UNIVERSITÀ DI PARMA

UNIVERSITA' DEGLI STUDI DI PARMA

DOTTORATO DI RICERCA IN

Scienze della Terra

Ciclo XXXIV

Dipartimento di Scienze Chimiche, della Vita e Sostenibilità Ambientale

SYN-TO POST-RIFT TECTONIC EVOLUTION OF THE RIO DO PEIXE BASIN (BRAZIL) AND IMPLICATIONS FOR SILICICLASTIC RESERVOIRS PROPERTIES

Coordinatore:

Chiar.mo Prof. Marco Roveri

Tutor:

Prof. Fabrizio Balsamo

Co-tutor:

Prof. Francisco Cezar Costa Nogueira

Prof. Francesca Cifelli

Dottorando: Matheus Amador Nicchio

Anni Accademici 2018/2019 – 2020/2021

ABSTRACT

The study of sedimentary basins is crucial to the global economy, as they are sources of underground water and hydrocarbon, strategic resources for the industrial development and human activities. The development of sedimentary basins is linked with the regional stress imparted by geodynamic processes, thus understanding their tectonic evolution help to constrain the structural pattern of the upper crust. This way, the study of sedimentary basins provides a great scientific contribution to global tectonic evolution and the distribution of resources and sites for CO2 storage.

In sedimentary basins dominated by porous siliciclastic sequences, the syn-sedimentary basin-boundary faults generally host thin tabular structures known as deformation bands. Such deformational features can develop as single or in clusters in response to tectonic processes, and generally reduce the host rock permeability of up to 4-5 orders of magnitude. Thus, linking the tectonic history with deformation bands evolution in sedimentary basins is important to constrain fluid migration and accumulation in siliciclastic reservoirs.

In this PhD thesis, the Rio do Peixe (RdP) basin, located in northeast of Brazil, is used as a case study to understand the intracontinental deformation during the progressive opening of the Atlantic Ocean in the Lower Cretaceous and the later Cenozoic reactivation. The effects of such tectonic evolution on the petrophysical properties of rocks are also documented, and implications for siliciclastic reservoirs are discussed.

The greatest challenge of studying the Rio do Peixe basin is the partial lack of quantitative data on the syn-rift stage, which leads to distinct interpretations for the tectonic evolution of the basin. On border faults, only few outcrops are identified, making it quite difficult to constrain the evolution of stretching directions during basin formation based only on field data. The syn-rift siliciclastic sequence of the RdP basin is affected by deformation bands, mm-thick scale with insufficient exposure of kinematic markers such as fault striae and evolved displacements. Additionally, as they are subseismic structures, it is very challenging to study using conventional methods such as seismic interpretation and field structural analysis. In this PhD thesis, multi-scale and multidisciplinary investigation was performed to constrain the tectonic evolution of the basin.

In the Rio do Peixe basin, excellent exposures of deformation bands in porous sandstones are common. These structures are very important for the oil industry as they substantially affect the petrophysical properties of siliciclastic reservoirs. In this context, it is very important to understand the deformation processes during the formation and evolution of deformation bands to predict their impacts on reservoir properties. In this PhD thesis we investigated the microstructural and petrophysical properties of deformation bands in connection with the evolutionary stages of the basin.

This PhD thesis is organized in 5 chapters, three of which correspond to articles acepted or submitted in peer review journals.

The chapter 1 is a brief introduction about the importance of the Rio do Peixe basin in terms of regional tectonics and its relevance for siliciclastic reservoirs study. Further, it is explained the fundamentals of anisotropy of magnetic susceptibility (AMS) and its application on tectonic interpretation of sedimentary basins. A general introduction of deformation bands and its importance to siliciclastic reservoirs is at the end of the chapter.

Chapter 2 is an article submitted to the Tectonics journal. In this work we performed AMS and structural analysis to constrain the syn-rift extensional stages of the Rio do Peixe basin and the intracontinental deformation in northeast Brazil during the Early Cretaceous. As main result, we observed that two orthogonal syn-rift stages were responsible for the opening of the Rio do Peixe Basin. The main extension direction of the basin gradually shifted from NNE to NW reflecting the intracontinental deformation of the Borborema Province due to the rotation of the stress field in South America continent during the pre-Pangea Breakup. This contribution is important for better understand of the opening of the South Atlantic Ocean.

The chapter 3 is an article submitted to the Journal of Structural Geology. In this contribution, we performed structural/microstructural and petrophysical analysis of deformation bands formed during the syn- and post-rift stage of the basin. This work distinguish the deformation intensity and its effects on fluid flow and mechanical properties on sedimentary units within the basin. As main result, we identified that post-rift deformation bands are likely to form more effective fluid flow barrier and forms more intensely comminuted fault core. It occurs because they form in an already tectonically compacted host rock. This contribution is of crucial importance to the industry, as the

progressive deformation observed due to the tectonic reactivation of the basin directly affects the sealing potential of siliciclastic reservoirs.

The chapter 4 is an article published in the Journal of Structural Geology. In this work, we emphasized the contribution of the cataclastic matrix generation in the sealing behavior of deformation bands. From high-resolution images, we performed 2D and 3D petrophysical analysis and observed that the amount of cataclastic matrix produced due to shear is either influenced by the mineralogy or the strain intensity of deformation bands. This contribution is of interest to the industry, as cataclastic deformation bands are a frequent problem in siliciclastic reservoirs around the world.

The chapter 5 is a general discussion and conclusions at the end of the thesis, emphasizing the influence of the tectonic evolution of the basin in silisciclastic reservoir properties.

Index

Chapter 1 – Introduction

The goal of this thesis is to constrain the syn-to post-rift tectonic evolution of the Rio do Peixe basin (RPB), located in northeast Brazil. This knowledge is very important, as the RPB is an excellent proxy to understand the intracontinental deformation in Borborema Province during the Early Cretaceous Pangea breakup, contributing to better constrain the regional stress field evolution responsible for the opening of the Atlantic Ocean. As tectonic regime may also control the deformation intensity and attributes of deformational features in sedimentary units, constraining the tectonic evolution of the Rio do Peixe basin provide an excellent way to link tectonic regimes with development and characteristics of minor structures such as the deformation bands (DBs). The DBs are common structures in porous siliciclastic reservoirs worldwide, and received much attention in the last decades for their role in subsurface fluid flow in acquirers, hydrocarbon reservoirs, and more recently sites for CO2 storage. In general, it is commonly accepted that they affect the fluid flow and mechanical properties of rocks by acting as sealing structures and increasing the rock resistance due cataclasis and pore collapse. In the case of the RPB, the large exposures of DBs with easy access facilitates its study, which makes the RPB an outstanding site to be used as analogue of porous siliciclastic reservoirs. In this PhD thesis, we investigated the petrophysical and microstructural properties of deformation bands and linked them to the identified tectonic stages recognized in the basin.

A brief explanation about the importance of studying the RPB basin from both scientific and economic points of view is provided in the next section. This is followed by an introduction to the AMS (anisotropy of magnetic susceptibility) method, used to constrain the tectonic evolution of the basin. This method was of great importance to this PhD thesis as it was the main tool to constrain the extensional main stretching directions even on apparently non-deformed zones (i.e., deformed zones with no fault planes or deformation bands) of the basin. A short review of deformation bands and their effects on siliciclastic reservoirs is also provided at the end of the introduction. Finally, in chapters 2, 3 and 4, we present our results as submitted or published papers organized from regional scale to micro-scale.

1.1 The scientific and economic importance of the Rio do Peixe Basin, NE Brazil

The Rio do Peixe Basin is one of the most important intracontinental sedimentary basin located in northeast Brazil. The basin owns a great scientific importance because it is an excellent proxy to the intracontinental deformation of the Borborema Province during the Early Cretaceous. The opening of the basin is resulted from extensional stress related to the opening of the Atlantic Ocean, which caused brittle reactivation of the E-W-striking Patos and NE-striking Portalegre (Françolin et al., 1994; Sénant & Popoff, 1991; Szatmari et al., 1987) shear zones, branches of the major Proterozoic Transbrazilian shear zone (Schobbenhaus et al., 1975). In this context, the understanding of the tectonic evolution of the Rio do Peixe basin is a great contribution to better understand the opening of the South Atlantic Ocean during the Cretaceous. These questions are better discussed in chapter 2, where the opening of the Rio do Peixe basin is explained.

The Rio do Peixe basin has also been the focus of several studies with great importance for the oil industry. Due to its excellent deformation band exposures with easy access (Araujo et al., 2018; Nicchio et al., 2018; Pontes et al., 2019), the basin is been recently used as analogue of siliciclastic reservoirs (Nogueira et al., 2021; Silva et al., 2021; Torabi et al., 2021). The analysis of deformation bands of the Rio do Peixe basin and its impacts in reservoirs is a great contribution to the petroleum industry, as the excellent fault-related deformation bands exposures in the basin facilitate researches with guidelines to predict fault zone structures and permeability in subsurface reservoirs.

1.2 Magnetic fabric of rocks and applications in basin tectonics

The anisotropy of magnetic susceptibility (AMS) method consist in a non-destructive and fast way to constrain the rock deformation even on apparently non-deformed rock. The method presents a wide range of use in geological studies as the magnetic properties of the rock is controlled by the crystallographic characteristics and grain shape of the main mineralogy of the rock (Borradaile & Henry, 1997; Borradaile, 1988; Lanza & Meloni, 2006; Rochette et al., 1992). In deformed rocks, the main crystallographic axes tend to be reoriented parallel to the main extensional direction. The magnetic susceptibility (K) is obtained from an induced magnetic field and is expressed in "SI" units. The magnetic fabric is represented represented as an ellipsoid composed of three main magnetic axes K1>K2>K3 that are inversely correlated to the stress field ($\sigma1>\sigma2>\sigma3$) with K1 parallel to $\sigma3$, thus representing the extensional direction of

deformed zones (Borradaile & Hamilton, 2004; Cifelli et al., 2005). This way, through the analysis of the magnetic fabric of sedimentary basins, it's possible to constrain the stretching direction of deformed zones. The efficiency of the anisotropy of magnetic susceptibility (AMS) to constrain tectonic evolution of sedimentary basins has already been proved by several works around the world, working on both extensional (Borradaile & Hamilton, 2004; Cifelli et al., 2005; Faccenna et al., 2002) and compressive (Test et al., 2019; Weinberger et al., 2022) regimes. In this thesis, the AMS was a great source of information to constrain the stretching direction of the main zones of the RPB and applied as an innovative method producing new relevant data to contribute to an updated tectonic interpretation. We combined the AMS data with the kinematic features observed in fault zones. For the rocks of the RPB, the method proved to be an excellent tool to constrain the extensional syn-rift phases of the basin. The results and interpretations are presented in chapter 2.

1.3 Deformation bands

Deformation bands (DBs) are millimeter-thick, tabular structures present in fault damage zones in porous rocks (Antonellini et al., 1994; Aydin, 1978; Fossen et al., 2017). The DBs can occur as single isolated structures or grouped as two or more sub parallel structures clustering in small volume of rock (Aydin, 1978). The classification of deformation bands, described by Fossen et al., 2007 and uptaded by Fossen et al., 2017 is based on kinematics (Fig. 1.2) and deformation mechanism (Fig. 1.3). The kinematic classification considers the changes in the rock volume and/or the shear. In this sense, deformation bands can be classified as compactional bands (local volume loss), simple shear bands (constant rock volume) or dilation bands (local volume increase). Additionally, as compaction and dilation commonly occur combined with shear, the terms compactional shear bands and dilation shear bands are used to classify deformation bands formed due compaction combined with shear and dilation combined with shear, respectively (Fig. 1.2).

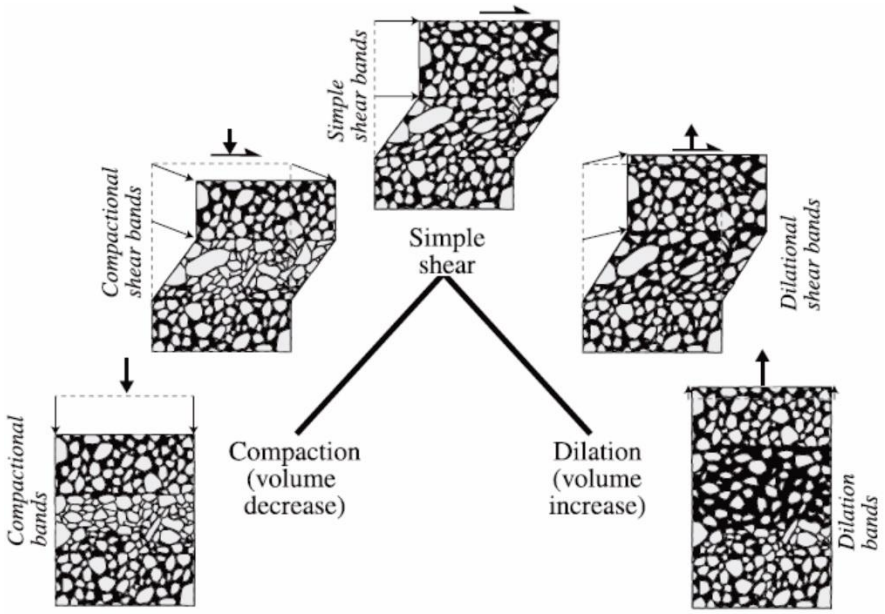

Fig.1.2 – Kinematic classification of deformation bands by Fossen et. al., (2007).

Four distinct deformation band types are described in terms of deformation mechanism (Fossen et. al., 2007; 2017). The disaggregation band (Fig. 1.3A) is formed due to localized disaggregation of grains. The Phyllosilicate bands (Fig. 1.3B) are common in clay-rich rocks. In this case, phyllosilicates are reoriented and aligned parallel to shear plane in the deformation band core. In cataclastic deformation bands (Fig. 1.3C), grain crushing and pore collapse localized in thin tabular structures is the main characteristic. To form this kind of band, at least some degree of compaction is needed. The solution and cementation band (Fig. 1.3D) is formed when cementation occurs preferentially within the band.

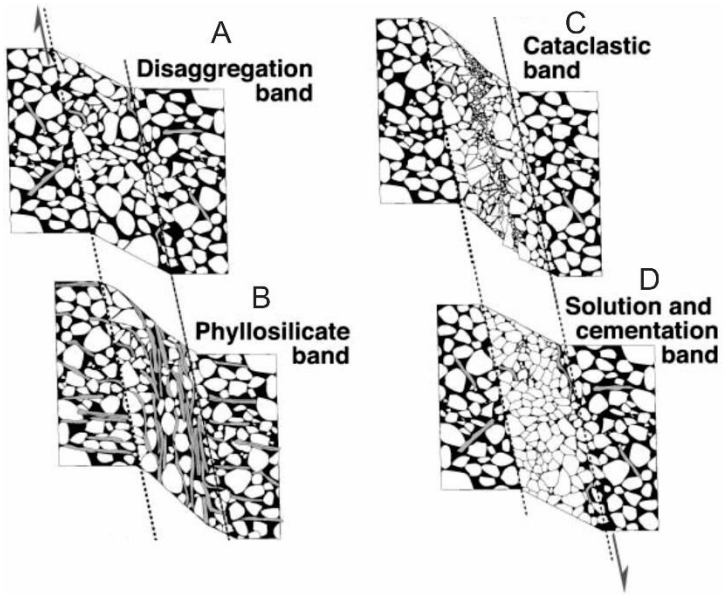

Fig. 1.3. Classification of deformation bands based on deformation mechanism by Fossen et al., 2007.

In the last decades, a great amount of studies concerning to deformation bands has been published (Ballas et al., 2012; F. Balsamo & Storti, 2010; Fossen & Bale, 2007; Philit et al., 2018; Torabi et al., 2013). This importance is given to its capacity to affect the petrophysical properties of porous siliciclastic rocks (Ballas et al., 2015; Soliva et al., 2016; Torabi, 2014; Torabi et al., 2013; Torabi & Fossen, 2009), that constitutes important oil reservoirs around the world, thus being of great interest for the oil industry. The effects of DBs in petrophysical properties of sandstones is given to its deformational mechanisms, the most common, grain fracturing and pore collapse, progressively increasing the strain hardening intensity and sealing potential in reservoirs (Aydin, 1978; Ballas et al., 2013, 2015; Torabi, 2014; Torabi et al., 2013). As result, the intense porosity reduction with the permeability reduction reaching up to six orders of magnitude in respect to the host rock (Balsamo & Storti, 2011; Fossen & Bale, 2007; Nogueira et al., 2021; Torabi et al., 2013). The main challenge of studying deformation bands in real reservoirs is the difficulty of getting in loco information, making it necessary to work in exposed analogue rocks. In this PhD thesis we studied the effects of deformation bands in coarse sandstones of the Rio do Peixe basin (Brazil) as analogue of siliciclastic reservoirs. Most of DBs studied in the RPB are cataclastic deformation bands developed both during Early Cretaceous syn-rift and Cenozoic post-rift phases. We performed multiscale and multidisciplinary study documenting the influence of basin reactivation on deformational processes and fluid flow (capillary pressure) properties of deformation

bands. This way, the deformation mechanism and the impacts of deformation bands in petrophysical properties of porous rocks described in this work is related exclusivelly to cataclastic shear compaction bands. A detailed description of these bands are found in chapters 3 and 4. On of the major finding of this study is that even a mild change in the stress field may determine capillary pressure properties of deformation bands, thus impacting fault sealing in porous siliciclastc reservoirs. This study contributes to predictive works that can be used worldwide in other structurally complex reservoirs.

References used in chapter 1

Almeida, F. F. M. De, Brito Neves, B. B. De, & Dal Ré Carneiro, C. (2000). The origin and evolution of the South American platform. *Earth Science Reviews*, *50*(1–2), 77–111. https://doi.org/10.1016/S0012-8252(99)00072-0

Antonellini, M. A., Aydin, A., & Pollard, D. D. (1994). Microstructure of deformation bands in porous sandstones at Arches National Park, Utah. *Journal of Structural Geology*, *16*(7), 941–959. https://doi.org/10.1016/0191-8141(94)90077-9

Araujo, R. E. B., Bezerra, F. H. R., Nogueira, F. C. C., Balsamo, F., Carvalho, B. R. B. M., Souza, J. A. B., et al. (2018). Basement control on fault formation and deformation band damage zone evolution in the Rio do Peixe Basin, Brazil. *Tectonophysics*, *745*(August), 117–131. https://doi.org/10.1016/j.tecto.2018.08.011

Aydin, A. (1978). Small faults formed as deformation bands in sandstone. *Pure and Applied Geophysics PAGEOPH*, *116*(4–5), 913–930. https://doi.org/10.1007/BF00876546

Ballas, G., Soliva, R., Sizun, J. P., Benedicto, A., Cavailhes, T., & Raynaud, S. (2012). The importance of the degree of cataclasis in shear bands for fluid flow in porous sandstone Provence, France. *AAPG Bulletin*, *96*(11), 2167–2186. https://doi.org/10.1306/04051211097

Ballas, G., Soliva, R., Sizun, J. P., Fossen, H., Benedicto, A., & Skurtveit, E. (2013). Shear-enhanced compaction bands formed at shallow burial conditions; implications for fluid flow (Provence, France). *Journal of Structural Geology*, *47*, 3–15. https://doi.org/10.1016/j.jsg.2012.11.008

Ballas, G., Fossen, H., & Soliva, R. (2015). Factors controlling permeability of cataclastic deformation bands and faults in porous sandstone reservoirs. *Journal of Structural Geology*, *76*, 1–21. https://doi.org/10.1016/j.jsg.2015.03.013

Balsamo, F., & Storti, F. (2010). Grain size and permeability evolution of soft-sediment extensional sub-seismic and seismic fault zones in high-porosity sediments from the Crotone basin, southern Apennines, Italy. *Marine and Petroleum Geology*, *27*(4), 822–837. https://doi.org/10.1016/j.marpetgeo.2009.10.016

Balsamo, Fabrizio, & Storti, F. (2011). Size-dependent comminution, Tectonic mixing, and sealing behavior of a "structurally oversimplified" fault zone in poorly lithified sands: Evidence for a coseismic rupture? *Bulletin of the Geological Society of America*, *123*(3–4), 601–619. https://doi.org/10.1130/B30099.1

Borradaile, Graham J., & Hamilton, T. (2004). Magnetic fabrics may proxy as neotectonic stress trajectories, Polis rift, Cyprus. *Tectonics*, *23*(1), 1–11. https://doi.org/10.1029/2002TC001434

Borradaile, Graham J., & Henry, B. (1997). Tectonic applications of magnetic susceptibility and its anisotropy. *Earth-Science Reviews*, *42*(1–2), 49–93. https://doi.org/10.1016/S0012-8252(96)00044-X

Borradaile, Graham John. (1988). Magnetic susceptibility, petrofabrics and strain. *Tectonophysics*, *156*, 1–20.

Cifelli, F., Mattei, M., Chadima, M., Hirt, A. M., & Hansen, A. (2005). The origin of tectonic lineation in extensional basins: Combined neutron texture and magnetic analyses on "undeformed" clays. *Earth and Planetary Science Letters*, *235*(1–2), 62–78. https://doi.org/10.1016/j.epsl.2005.02.042

Faccenna, C., Speranza, F., Caracciolo, F. D. A., Mattei, M., & Oggiano, G. (2002). Extensional tectonics on Sardinia (Italy): Insights into thearc-back-arc transitional regime. *Tectonophysics*, *356*(4), 213–232. https://doi.org/10.1016/S0040-1951(02)00287-1

Fossen, H., Schultz, R. A., Shipton, Z. K., & Mair, K. (2007). Deformation bands in sandstone: a review. Journal of the Geological Society, 164, 1–15. https://doi.org/10.1144/0016-76492006-036

Fossen, H., & Bale, A. (2007). Deformation bands and their influence on fluid flow. *AAPG Bulletin*, *91*(12), 1685–1700. https://doi.org/10.1306/07300706146

Fossen, H., Soliva, R., Ballas, G., Trzaskos, B., Cavalcante, C., Schultz, R. A., et al. (2017). A review of deformation bands in reservoir sandstones : geometries, mechanisms and distribution. *Geological Society of London Special Publication*, *459*. https://doi.org/10.1144/SP459.4

Françolin, J. B. L., Cobbold, P. R., & Szatmari, P. (1994). Faulting in the Early Cretaceous Rio do Peixe basin (NE Brazil) and its significance for the opening of the Atlantic. *Journal of Structural Geology*, *16*(5), 647–661. https://doi.org/10.1016/0191-8141(94)90116-3

Lanza, R., & Meloni, A. (2006). *The Earth's Magnetism. An introduction for geologists.* Berlin: Springer.

Nicchio, M. A., Nogueira, F. C. C., Balsamo, F., Souza, J. A. B., Carvalho, B. R. B. M., & Bezerra, F. H. R. (2018). Development of cataclastic foliation in deformation bands in feldspar-rich conglomerates of the Rio do Peixe Basin, NE Brazil. *Journal of Structural Geology*, *107* (December 2017), 132–141. https://doi.org/10.1016/j.jsg.2017.12.013

Nogueira, F. C. C., Nicchio, M. A., Balsamo, F., Souza, J. A. B., Silva, I. V. L., Bezerra, F. H. R., et al. (2021). The influence of the cataclastic matrix on the petrophysical properties of deformation bands in arkosic sandstones. *Marine and Petroleum Geology*, *124*(November 2020), 15. https://doi.org/10.1016/j.marpetgeo.2020.104825

Philit, S., Soliva, R., Castilla, R., Ballas, G., & Taillefer, A. (2018). Clusters of cataclastic deformation bands in porous sandstones. *Journal of Structural Geology*, *114*(April), 235–250. https://doi.org/10.1016/j.jsg.2018.04.013

Pontes, C. C. C., Nogueira, F. C. C., Bezerra, F. H. R., Balsamo, F., Miranda, T. S., Nicchio, M. A., et al. (2019). Petrophysical properties of deformation bands in high porous sandstones across fault zones in the Rio do Peixe Basin , Brazil. *International Journal of Rock Mechanics and Mining Sciences*, *114*(May 2017), 153–163. https://doi.org/10.1016/j.ijrmms.2018.12.009

Robustelli Test, C., Festa, A., Zanella, E., Codegone, G., & Scaramuzzo, E. (2019).

Distinguishing the mélange-forming processes in subduction-accretion complexes: Constraints from the anisotropy of magnetic susceptibility (AMS). *Geosciences (Switzerland)*, *9*(9). https://doi.org/10.3390/geosciences9090381

Rochette, P., Jackson, M., & Aubourg, C. (1992). Rock magnetism and the interpretation of anisotropy of magnetic susceptibility. *Reviews of Geophysics*, *30*(3), 209–226.

Schobbenhaus, C., C. L. Ribeiro, L. A. Oliva, J. T. Takanohashi, A. G. Lindenmayer, J. C. Vasconcelos, and V. Orlandi (1975), Folha Goiás SD.22, with explanatory text, in Carta Geológica do Brasil Milionésimo, edited by C. Schobbenhaus, DNPM, Brasília, DF, Brazil.

Sénant, J., & Popoff, M. (1991). Early Cretaceous extension in northeast Brazil related to the South Atlantic opening. *Tectonophysics*, *198*(1), 35–46. https://doi.org/10.1016/0040-1951(91)90129-G

Silva, M. E., Nogueira, F. C. C., Pérez, Y. A. R., Vasconcelos, D. L., Stohler, R. C., Sanglard, J. C. D., et al. (2021). Permeability modeling of a basin-bounding fault damage zone in the Rio do Peixe Basin, Brazil. *Marine and Petroleum Geology*, *135*(October 2021), 105409. https://doi.org/10.1016/j.marpetgeo.2021.105409

Soliva, R., Ballas, G., Fossen, H., & Philit, S. (2016). Tectonic regime controls clustering of deformation bands in porous sandstone. *Geology*, *44*(6), 423–426. https://doi.org/10.1130/G37585.1

Szatmati, P., Françolin, J. B. L., Zanotto, O., Wolff, S. (1987). Evolução Tectônica Da Margem Equatorial Brasileira. *Revista Brasileira de Geociências*, *17*(2), 180–188. https://doi.org/10.25249/0375-7536.1987180188

Torabi, A. (2014). Cataclastic bands in immature and poorly lithified sandstone, examples from Corsica, France. *Tectonophysics*, *630*(C), 91–102. https://doi.org/10.1016/j.tecto.2014.05.014

Torabi, A., & Fossen, H. (2009). Spatial variation of microstructure and petrophysical properties along deformation bands in reservoir sandstones. *AAPG Bulletin*, *93*(7), 919–938. https://doi.org/10.1306/03270908161

Torabi, A., Fossen, H., & Braathen, A. (2013). Insight into petrophysical properties of deformed sandstone reservoirs. *AAPG Bulletin*, *97*(4), 619–637.

https://doi.org/10.1306/10031212040

Torabi, A., Balsamo, F., Nogueira, F. C. C., Vasconcelos, D. L., Silva, A. C. E., Bezerra, F. H. R., & Souza, J. A. B. (2021). Variation of thickness, internal structure and petrophysical properties in a deformation band fault zone in siliciclastic rocks. *Marine and Petroleum Geology*, *133*, 105297. https://doi.org/10.1016/j.marpetgeo.2021.105297

Weinberger, R., Alsop, G. I., & Levi, T. (2022). Magnetic fabrics as strain markers in foldes soft-sediment layers. *Journal of Structural Geology*. https://doi.org/10.1016/j.jsg.2022.104513

Chapter 2 - An integrated structural and magnetic fabric study to constrain the progressive extensional tectonics of the Rio do Peixe Basin, Brazil

This chapter is presented in the form of manuscript. The manuscript is under preparation to be submited to Tectonics. In this article we combined structural and Anisotropy of Magnetic Susceptibility (AMS) data to constrain the extensional tectonics of the Rio do Peixe basin. This is a contribution to better understand the tectonics of the Borborema Province (Brazil) resulted from the opening of the Atlantic Ocean, Cretaceous. This work brings new information to support the development of the knowledge about the Pangea breakup. As main conclusion, we proposed an evolutionary model with two main stretching directions that resulted in the syn-rift I and syn-rift II deformational stages of the Rio do Peixe basin as a response to a progressive deformation.

Nicchio, M.A[a,*]; Balsamo, F[a]; Cifelli, F[b]; Nogueira, F.C.C[c]; Aldega, L.[d]; Bezerra, F.H.R[e]; Vasconcelos. D. L[c]; Souza, J.A.B[f]

[a] Department of Chemistry, Life Science and Environmental Sustainability, University of Parma, Parma, Italy;

[b]Dipartimento di Scienze, Università Roma TRE, Rome, Italy;

[c] Laboratório de Pesquisa Em Exploração Petrolífera, Departamento de Engenharia Do Petróleo, Universidade Federal de Campina Grande, Campina Grande, PB, Brazil;

[d] Dipartimento di Scienze dela Terra, Sapienza Università di Roma, Rome, Italy;

[e] Universidade Federal Do Rio Grande Do Norte, Campus Universitário, Natal, RN, Brazil;

[f] Petrobras, Rio de Janeiro, RJ, Brazil.

Abstract

We constrained the tectonic evolution of the intracratonic Cretaceous Rio do Peixe basin (RPB), combining structural and Anisotropy of Magnetic Susceptibility (AMS) data. We analyzed structural features of 4 sites along two major faults bordering the basin, the NE-striking Portalegre fault and the E-W-striking Malta fault. AMS data from 42 sites distributes along the basin suggest two stretching directions driving the opening of the RPB. The early syn-rift phase I resulted from N-S to NNE stretching direction with vertical σ1, producing normal fault displacement along the E-W-striking Malta fault and

right-lateral transtension along the NE-striking Portalegre fault, Sítio Saguí and Lagoa do Forno faults. The syn-rift phase II results from NW stretching direction with vertical σ1, causing normal displacement on NE-striking major faults and left-lateral transtension on E-W-striking major faults. Additionally, the NW extension was responsible for forming NE-striking extensional faults and deformation bands in sedimentary units. The RPB developed due to the intraplate deformation on Borborema Province during the early stage of the Pangea Breakup. The stretching direction gradually shifted from NNE to NW as a consequence of the South America clockwise rotation. The extensional stress orthogonal to the main E-W-striking and NE-striking Precambrian shear zones facilitated the opening and evolution of the RPB.

2.1 Introduction

The Anisotropy of Magnetic Susceptibility (AMS) has been widely used as a proxy for the tectonic interpretation of sedimentary basins (Borradaile & Jackson, 2004; Faccenna et al., 2002; García-Lasanta et al., 2018; Porreca & Mattei, 2012). As the magnetic fabric is concordant with the gross petrofabric of the rock (Borradaile, 1988), it represents a powerful tool for tectonic reconstructions, even in rocks at a low grade of deformation or in zones where deformation is not visible (Cifelli et al., 2004; Schwehr & Tauxe, 2003).

The Pangea Breakup is one of the most important events of the tectonic history of the Earth. This event had its begining in (145 Ma) and determined the actual continent disposal (Heine et al., 2013; Moulin et al., 2010; Peace et al., 2020). Its understanding is of crucial importance as one of its main results is the opening of the Atlantic Ocean. The event was responsible to rifting events that resulted in several sedimentary basins in South America and Africa continents not only at the coast but also in intracontinental zones (Frizon De Lamotte et al., 2015; Heine et al., 2013; Moulin et al., 2010). Thus, the tectonic study of the syn-rift intracontinental basins is an excellent proxy to better understanding of the Pangea Breakup event (Frizon De Lamotte et al., 2015). In Borborema Province (northeast Brazil), the initial stress responsible for the Pangea Breakup is recorded in dyke intrusions (Matos et. al., 2021) and intracontinental syn-rift sedimentary basins (Celestino et al., 2020; Peralta Gomes et al., 2018).

In this study, we use the Rio do Peixe Basin (RPB) as case of study to contribute to the understanding of the Pangea Breakup event and its effects on the Borborema Province.

In the Rio do Peixe Basin (RPB), the lack of structural field information, mostly from its central regions, where apparently undeformed fine sandstones and shales are exposed (Sénant & Popoff, 1991; Françolin et al., 1994), turns the tecnonic study of the basin into a very challenging task. The intrabasinal deformation occurs as deformation bands mainly developed on coarse sandstones, while a complex network of deformation bands and minor faults are localized in the proximity of major basin-boundary faults (Araujo et al., 2018; Nicchio et al., 2018; Pontes et al., 2019; de Souza et al., 2021; Nogueira et al., 2021; Torabi et al., 2021; Silva et al., 2022). The lack of clear kinematic features, typical of deformation bands, makes the interpretation of the displacement direction and paleostress field evolution within the sedimentary units very complex.

Utilizing structural data, seismic interpretations, and potential data, previous studies discussed the Cretaceous syn-rift (Sénant & Popoff, 1991; Françolin et al., 1994; de Castro et al., 2007, 2008; Marques et al., 2014; Peralta Gomes et al., 2018; Celestino et al., 2020) and the Cenozoic post-rift tectonic inversion (Marques et al., 2014; Nogueira et al., 2015; Vasconcelos et al., 2021) of the intracontinental basins of Northeast Brazil during the Pangea breakup. However, the evolution of intraplate tectonic activity responsible for opening of intracontinental sedimentary basins in the Borborema Province during the Cretaceous syn-rift stage is still debated and poorly constrained by regional geophysical and field data (e.g., de Castro et al., 2007, 2008; Marques et al., 2014; Nogueira et al., 2015). Such information is of paramount importance to better constrain the tectonic evolution of Northeast Brazil during the Pangea Breakup

In this study, we present a new interpretation about the development and tectonic evolution of the Rio do Peixe Basin (RPB) focusing mostly on the stretching direction along the whole basin during the syn-rift stage. We used AMS analysis of deformed and undeformed sedimentary rocks and structural data collected on both main border faults and intrabasin domains. Two main stretching directions responsible for the opening of the RPB are oriented NNE-SSW and NW-SE. The NNE-SSW stretching direction is observed on border fault zones. It has been predominant during the syn-rift phase I, thus resulting in the development of normal kinematics of the N-dipping, E-W-trending Malta fault. The same stretching direction was responsible for the dextral transtensive displacement of the NE-SW-trending Portalegre Fault. The syn-rift phase II is marked by NW-SE stretching direction and is observed on the west Malta fault and intrabasin deformation on sedimentary units, being predominant during the late syn-rift stage. It is

responsible for the left-lateral transtensive displacement on the western portion of the E-W Malta fault and NE-striking normal faults within the basin. The overall stress field responsible for the Pangea Breakup event was recorded in intracontinental deformation of the Borborema Province in northeast Brazil and is observed in the main structures of the Rio do Peixe basin.

2.2 Geological Settings

The Rio do Peixe (RPB) is an intracontinental basin located along Precambrian shear zones in the Borborema Province, northeast Brazil (Fig. 2.1A). The RPB is one of the most important sedimentary basins in the region, tectonically correlated with other basins in northeastern Brazil (Matos, 1992). The RPB is composed of three sub-basins, from W to E, named Brejo das Freiras (BFSB), Sousa (SSB) (Fig. 1B), and Pombal. All sub-basins are subgrabens presenting a major faulted border and a flexural border (Sénant & Popoff, 1991; Nogueira et al., 2004). The sub-basins are elongated following the trend of their border faults: NE Portalegre Fault (Brejo das Freiras), E-W Malta Fault (Sousa) and NE Rio Piranhas Fault (Pombal). Two main depocenters were identified in the basin by gravimety (Nogueira et al., 2004; de Castro et al., 2007) and seismic data (Rapozo et al., 2021; Vasconcelos et al., 2021). In the BFSB, the depocenter is localized in the southern zone of the Portalegre fault and follows the fault trend. In the SSB, the depocenter is aligned along the Malta fault with deeper portions at the inflection zones between the NE-trending faults (Sítio Saguí and Lagoa do Forno) and the Malta Fault (Fig. 2.1B).

The RPB presents a tectonic evolution characterized by syn- and normal faulting and post-rift transpression (Nogueira et al., 2015; Vasconcelos et al., 2021). The opening of the basin is related to the brittle reactivation of the E-W-striking Patos and NE-SW-striking Portalegre ductile shear zones (Fig. 2.1A). This reactivation led to the development of the E-W-striking Malta Fault at the southern border of the SSB and the NE-SW-striking Portalegre Fault at the eastern border of the BFSB (Sénant & Popoff, 1991; Françolin et al., 1994) (Fig. 2.1B). The RPB presents Devonian pre-rift units (Lourenço et al., 2021; Rapozo et al., 2021; Vasconcelos et al., 2021) and Cretaceous rift units that span from the early (145 My) to late Cretaceous (125 My) (Braun, 1969; Lima & Coelho, 1987; Arai, 2006; Sousa et al., 2018). It was suggested that the Cretaceous rifting of the basin is related to intracontinental deformation during the initial opening of the Atlantic Ocean (Matos, 1992).

The extensional tectonics of the basin is still under debate, as different interpretations have been proposed. Szatmari et al. (1987) interpreted that the basin was formed due to N-S-oriented extension. According to the authors, during the initial stage of the opening of the Atlantic Ocean, the clockwise rotation of the South American continent would have pressed the northeastern region of Brazil against the African continent, resulting in an E-W-oriented compression and a N-S-oriented extension. Following a similar interpretation, Françolin et al. (1994) suggested that the initial opening of the RPB is marked by NW-SE-oriented extension as a result of ENE-SWS-oriented compression, thus generating a left-lateral wrenching. On the other hand, Sénant & Popoff (1991) proposed that the N-S-oriented extension with vertical σ_1 might have been the initial stretching direction of the basin.

The post-rift stage of RPB was marked by tectonic inversion, identified through reverse reactivated border faults (Nogueira et al., 2015), inverted deep normal faults within the basin (Vasconcelos et al., 2021), and conjugate systems of minor strike-slip faults and deformation bands overprinting the syn-rift normal faults (Nicchio et al., submitted). During this inversion stage, an E-W-oriented compression was responsible for the reactivation of the rift faults under a strike-slip stress field (Nogueira et al., 2015; Vasconcelos et al., 2021).

Three main synchronous and heterolytic syn-rift siliciclastic formations occurs in the RPB. The Antenor Navarro Formation is a fluvial deposit composed of braided rivers, where basal trough cross-bedding conglomerates are predominant (Braun, 1969; Françolin et al., 1994). They occur as metric-scale channel deposits, where the conglomerates are overlapped by medium and fine sandstones on fining upwards deposits. The Sousa Formation is composed of fine-grained deposits, with the predominance of mudstones, muddy sandstones, and marls occurrences (Sénant & Popoff, 1991). The Sousa Formation is composed of meandering river deposits interspersed with flood plains. The Rio Piranhas Formation is composed of coarse conglomerates that interfinger with sandstones and siltstones. Its occurrence is restricted to the border faults and is interpreted as alluvial fan deposits, which resulted from the fault evolution during the opening of the basin (Sénant & Popoff, 1991; Françolin et al., 1994). Based on X-ray diffraction analysis of clay minerals of outcrop and borehole samples, Nicchio et al. (submitted) suggested that the three Formations experienced a maximum burial depth <1-2 km.

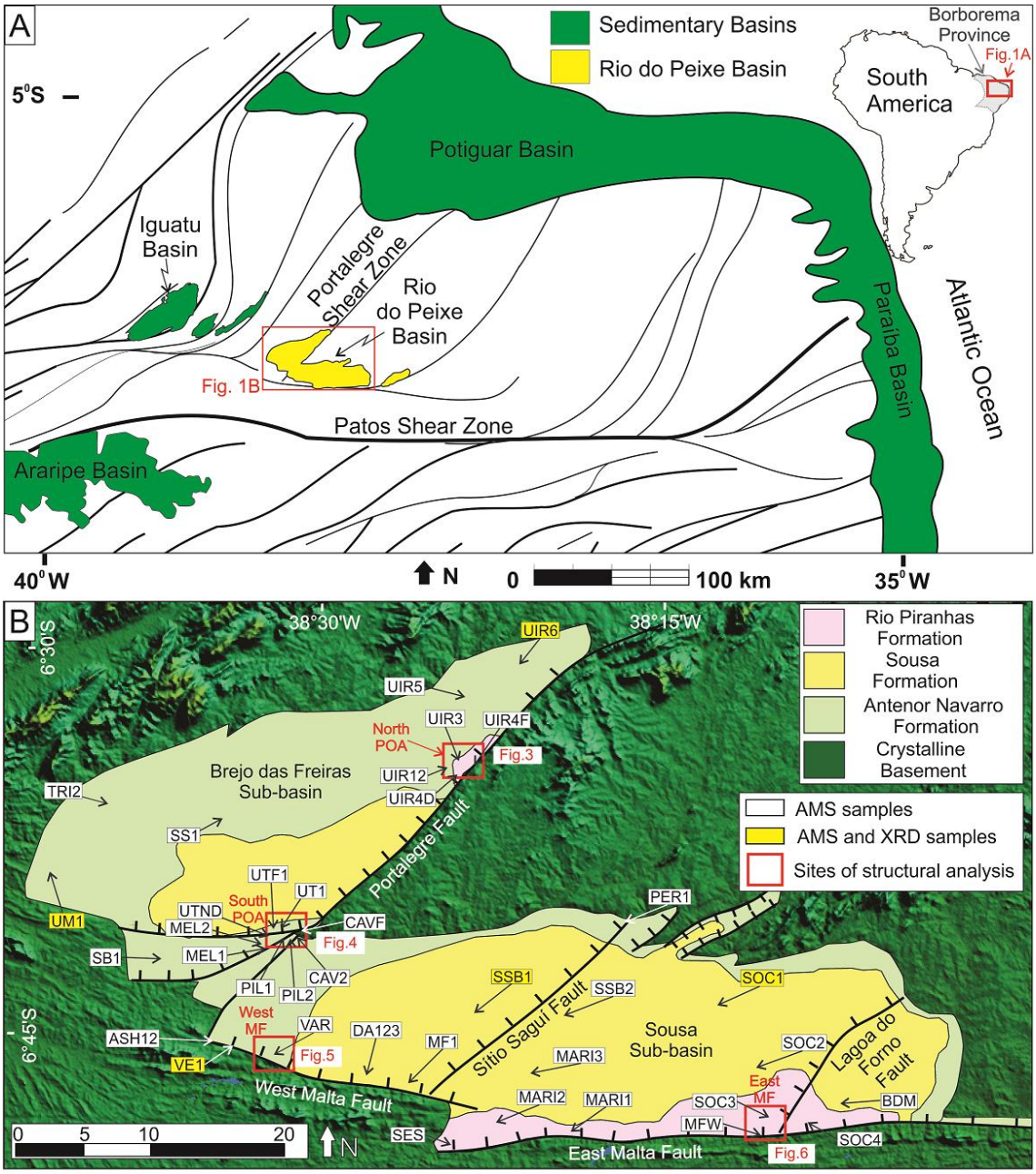

Fig. 2.1 – (A) Location of the Rio do Peixe Basin in a simplified tectonic framework of northeastern Brazil (modified from Nogueira et al., 2015). (B) Geological map of the Rio do Peixe Basin with major structures (modified from Nogueira et al., 2021). Red boxes indicate the studied outcrops for structural analysis. White and yellow boxes indicate the sampling point for AMS (Anisotropy of Magnetic Susceptibility) analysis and the name of the sample. Yellow boxes indicate the samples analyzed with X-ray diffraction (XRD).

2.3 Methods

Field data consist of structural analysis and paleocurrent analysis. The structural analysis was performed on four areas (red boxes in Fig. 2.1B) along the main fault zones. We collected structural data from faults, open fractures, and deformation bands along the northern and southern areas of the Portalegre fault, and the eastern and western areas of

the Malta fault (Fig. 2.1B). In the exposures close to the bordering fault, we compared structural data from the crystalline basement (35 fault planes and 73 fractures) with rift units deformation of the major fault damage zone (19 fault planes and 44 deformation bands). As only a few striae and kinematic indicators were identified on the border fault, we used joint to infer the extensional direction on crystalline basement, since joint directions strike perpendicular to the minimum principal stress (σ_3) (Dyer, 1988). In addition, we measured a total of 88 paleocurrent data from 15 outcrops, considering the trough axis inclination of the cross-trough bedding and crest direction of ripples as indicative of paleocurrent direction.

We also performed AMS analysis, which is a non-destructive method that allows characterizing depositional and deformation patterns of sedimentary deposits. AMS is defined by a symmetric second rank tensor and represented geometrically by an ellipsoid with principal axes K_1, K_2, K_3. Several parameters have been defined both for quantifying the magnitude of anisotropy and for defining the shape of the ellipsoid (Table 2.2; Hrouda, 1982). The T-shape parameter varies from +1 (perfectly prolate ellipsoid, $K_1 > K_2 = K_3$) to -1 (perfectly oblate ellipsoid, $K_1 = K_2 > K_3$), while a value of 0 corresponds to a triaxial ellipsoid. The magnetic lineation L (K_1/K_2) is defined by the orientation of K_1, while the magnetic foliation F (K_2/K_3) is defined as the plane perpendicular to K_3. The anisotropy degree is expressed by the parameter Pj. The mean magnetic susceptibility ($K_{mean} = (K_1 + K_2 + K_3)/3$) gives a relative estimation of the amount of magnetic minerals in the sample (Borradaile, 1988; Rochette et al., 1992).

In undeformed units, the magnetic susceptibility ellipsoid is generally oblate with the foliation plane subparallel to bedding; this fabric is attributed to depositional and/or compaction processes (Hamilton et al., 1970; Teh-Quei Lee et al., 1990; Paterson et al., 1995). If sediments undergo tectonic deformation, an AMS sub-fabric progressively develops, modifying the primary magnetic fabric according to the nature and extent of deformation (e.g., Borradaile and Tarling, 1981). Particularly in extensional basins, the magnetic lineation usually coincides with the maximum stretching direction, which is orthogonal to the main normal faults and generally aligned with the bedding dip (Mattei et al., 1997; Cifelli et al., 2005).

In this study, we collected a minimum of four cylindrical cores with a battery-powered driller equipped with a cooling water pump in 42 sites (Fig. 2.1B). When possible, the sampling was performed on clay-rich rocks. Extracted cores (2.5 cm in diameter and 3-

15 cm long) were oriented in situ by a magnetic compass. All oriented samples were cut in cylindrical standard specimens of 2.5cm in diameter and 2.1 in height. For each site, we performed a minimum of nine AMS measurements. A total of 531 AMS measurements were carried out on samples collected along the whole basin, being 316 on the SSB and 225 on the BFSB.

The low field magnetic susceptibility (k) was measured in the laboratory of Paleomagnetism at Roma Tre University. We used the KLY-3 from the Kappabridge equipment. For data processing, we used the software Anisoft 4.2, applying the Jelinek's statistics (Jelinek, 1981) to evaluate and validate the acquired anisotropy degree and shape parameter data. As primary structures of rocks might influence the AMS fabric (Borradaile, 1988; Rochette et al., 1992), we compared the acquired magnetic fabric of each sample with the bedding and paleocurrent of each site to constrain better the origin of the magnetic fabric, either sedimentary or due to tectonic deformation. To interpret the type of magnetic fabric of each sample, we used the stereonet interpretation methodology proposed by Lanza & Meloni (2006).

2.4 Results

2.4.1 Paleocurrent analysis of syn-rift units

The Antenor Navarro Formation is composed of interbedded fine conglomerates and coarse sandstones (Fig. 2.2A). The main facies of the Antenor Navarro Formation is composed of several decimetric to metric beds of fine conglomerates, which present features of high-energy river channels forming cross-trough bedding (Fig. 2.2B). Subparallel decimeter sandstone layers occur as lenses within the conglomerate beds (Fig. 2.2A). The Sousa Formation is composed of laminated shale and clay-rich fine sandstones to siltstones with ripple marks (Fig. 2.2C). The reconstructed paleocurrent directions are not homogeneous along the basin, and three main directions were observed: NE-SW, NW-SE, and E-W (Fig. 2.2D). In the BFSB, the inner zones show paleocurrent directions toward SE and SSW, thus the Portalegre Fault direction. Close to the Portalegre Fault, the paleocurrent also occurs in the opposite direction, following the fault dip direction towards NW. In the SSB, different paleocurrent directions are observed. Near to the Malta Fault, the paleocurrent direction shows sedimentation towards the border fault (SE and SW directions), subparallel to the border fault (toward W), and following the fault dip

direction towards NE. In the inner portions of the SSB, the paleocurrent direction spans from SE, SW to NW direction (Fig. 2.2D).

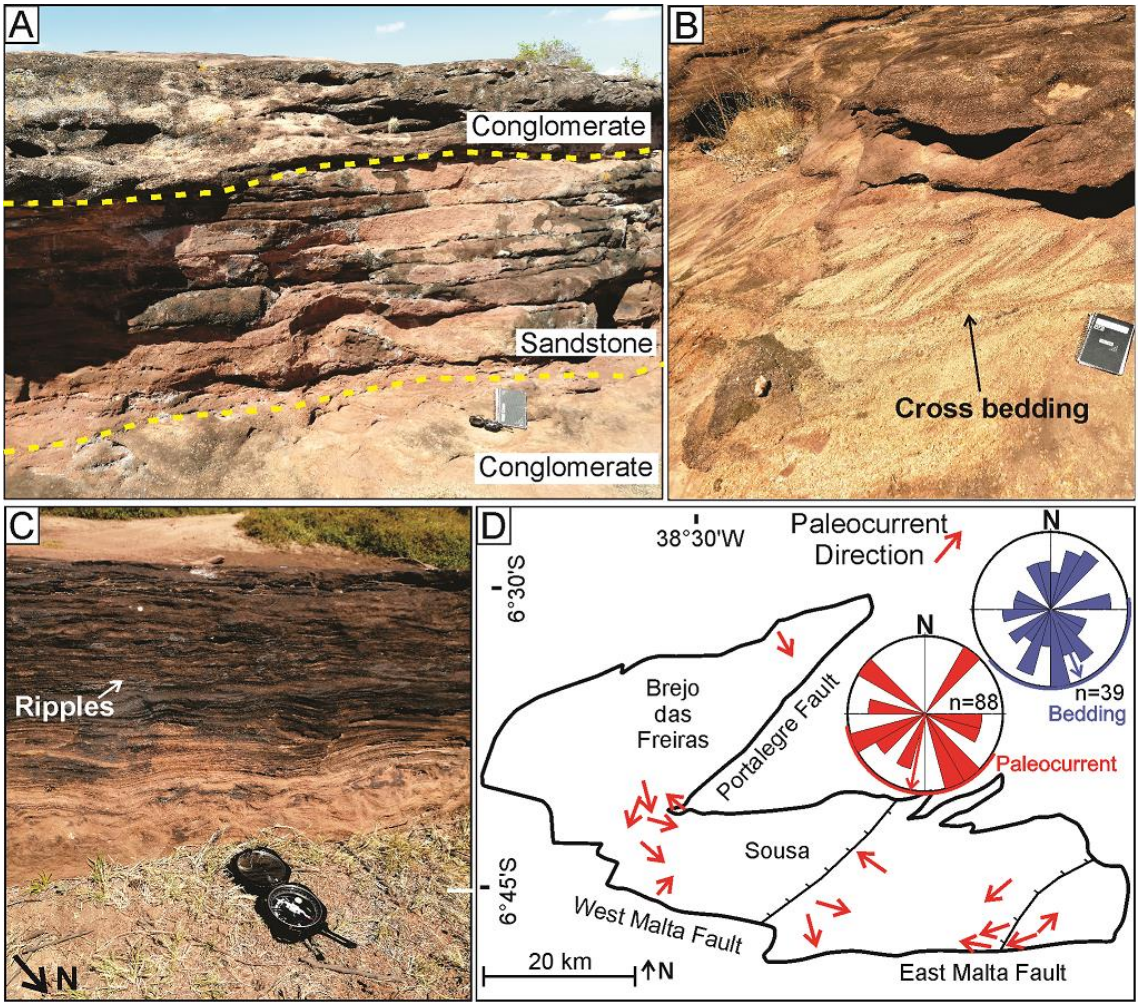

Fig. 2.2– Host rock characteristics. (A) Section view of sandstone layers interbedded within two conglomerate layers (Antenor Navarro Fm.). (B) Detailed section view of conglomerate with cross-bedding (Antenor Navarro Fm.). (C) Detailed plan view of fine sandstone with ripple marks (Sousa Fm.). (D) Map view of paleocurrent direction (red arrows). Red stereogram indicates cumulative paleocurrent direction. Blue stereogram indicates the azimuth direction of the bedding in the outcrops.

2.4.2 Structural Data

The border faults were analysed in four distinct sites. Two sites were studied along the NE-SW-striking Portalegre fault, being one in its northern zone (fig. 2.3) and one in its southern zone (Fig. 2.4). The Portalegre fault presents right-lateral transtensive movement with fault plane parallel to proterozoic ductile foliation of the Portalegre shear zone. In E-W-striking Malta fault, two sites were analyzed, being one in its western zone (Fig. 2.5) and one in tis eastern zone (Fig. 2.6). The Malta fault presents normal displacement with fault plane parallel to the ductile foliation of the Patos shear zone.

2.4.2.1 North Portalegre Fault

The Portalegre Fault is well exposed in the northern region of the BFSB, where the crystalline basement is in contact with sedimentary units of the Antenor Navarro Formation. The fault strikes NE-SW and dips steeply toward NW (Fig. 2.3A). The striae found on the main fault surface are sub-horizontal and indicate dextral movement. Several E-W trending joints occur (Fig. 2.3B), compatible with dextral movement due to N-S extension. Decimetric to metric spaced NNE-striking deformation bands occur in conglomeratic sandstone of the damage zone (Fig. 2.3C). The deformation bands are locally reopened and filled with quartz veins (Fig. 2.3D).

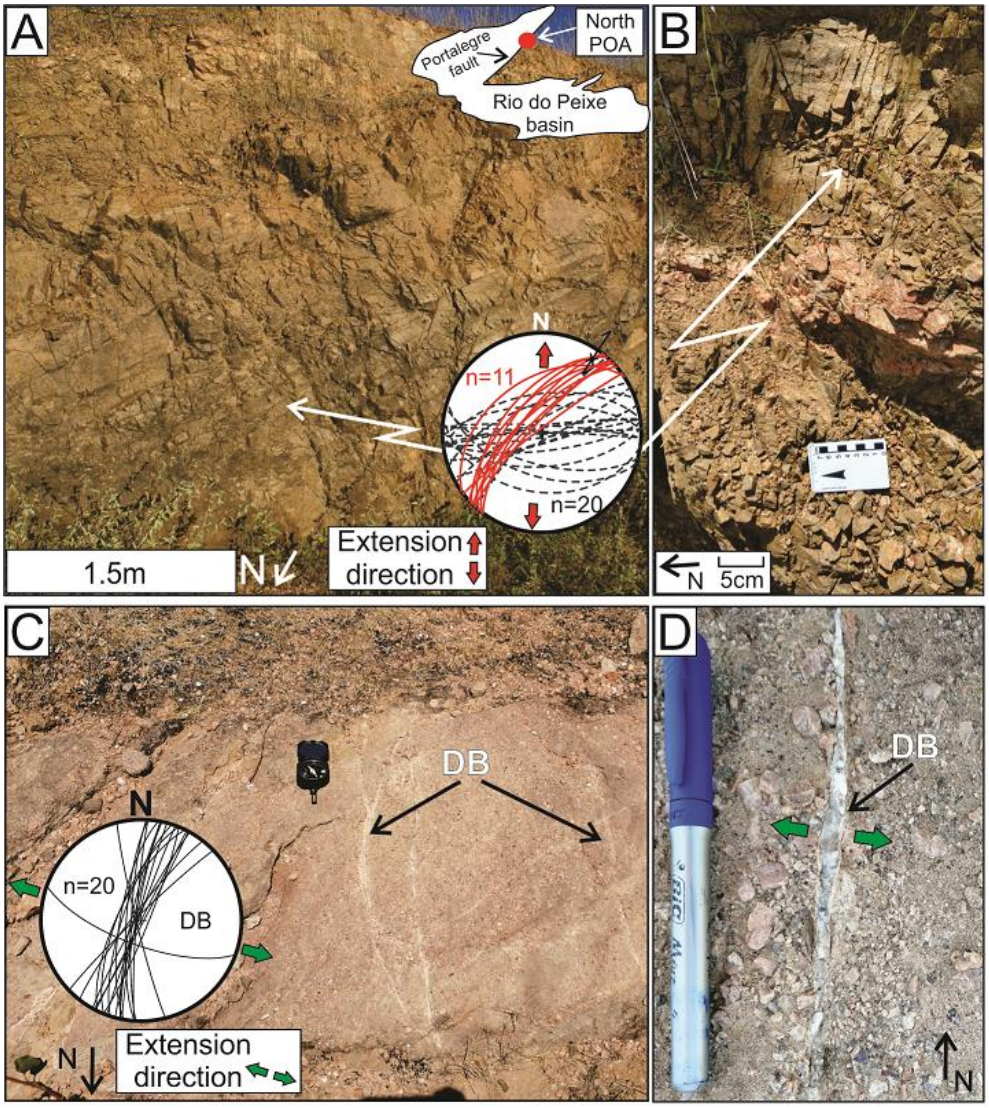

Fig. 2.3 – Outcrop view of the North Portalegre Fault: (A) NE-striking border fault plane (red lines in stereogram) in the crystallyne basement with E-W-striking open joints (dashed black lines in stereogram) indicating right lateral transtension. Red arrows indicate the extension direction. (B) Detail of E-W-striking open joints in the fault footwall. (C) NNE-striking deformation bands (black lines in stereogram) in coarse sandstones of the Antenor Navarro Fm. close to the border fault. (D) Detail of NNE-

striking deformation bands filled with quartz vein indicating a WNW-ESE extension (green arrows).

2.4.2.2 South Portalegre Fault

In the Southern part of the Portalegre Fault, the crystalline basement is in contact with the Antenor Navarro Formation coarse sandstone (Fig. 2.4A). The crystalline basement is intensely fractured and silicified trending NE-SW (Fig. 2.4B). Close to the fault, the sedimentary unit presents no visible deformation, preserving its original sedimentary features with bedding dipping towards NNW (Fig. 2.4C). In the vicinity of the border fault core, minor NE-striking faults occur (Fig. 2.4D). These minor faults that dip toward south are antithetic to the Portalegre Fault present striae with low obliquity to downdip.

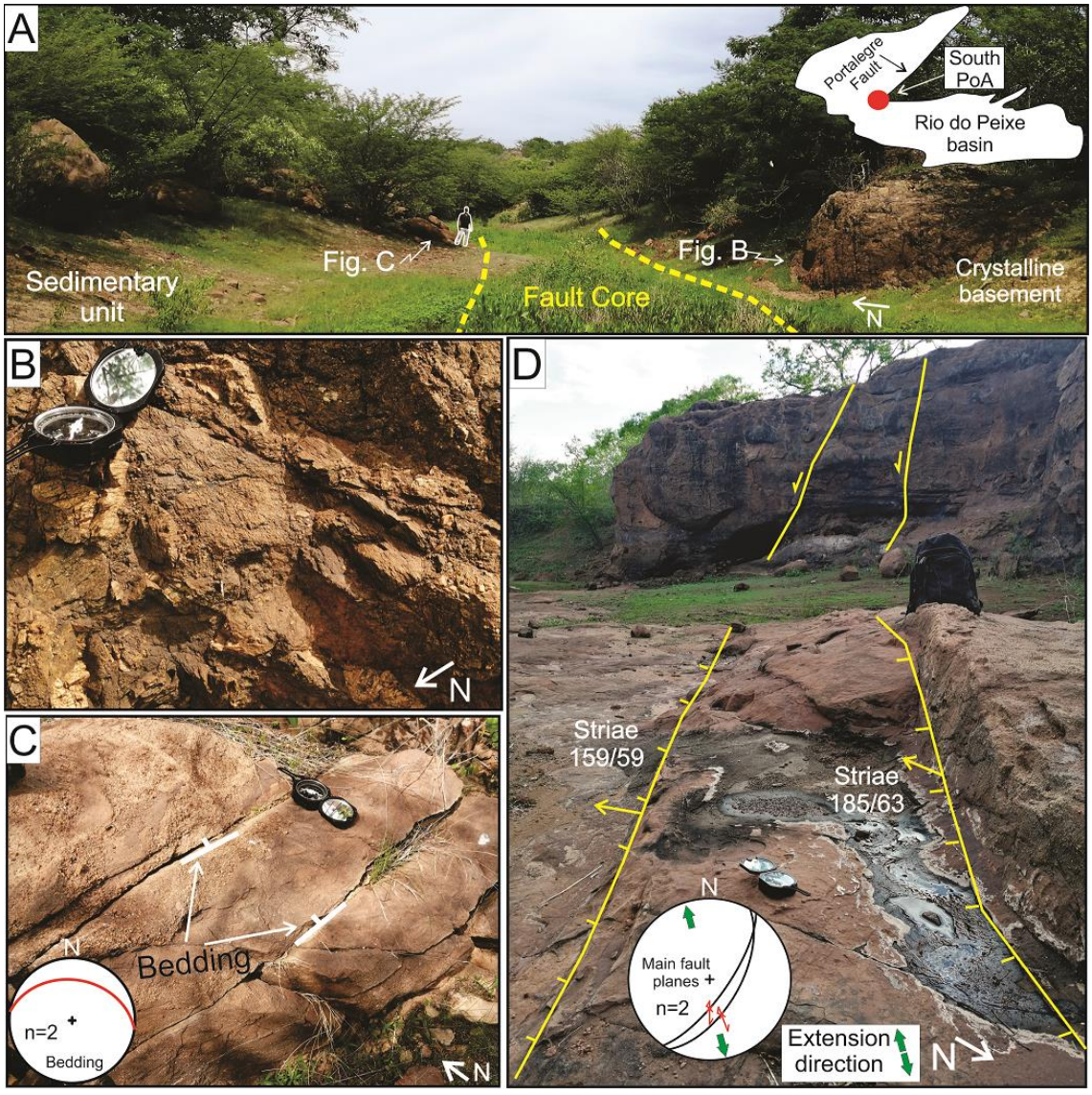

Fig. 2.4– Outcrop view of South Portalegre Fault: (A) General view of the outcrop indicating the Portalegre Fault core separating the crystalline basement and sedimentary

units of the Antenor Navarro Formation. (B) Detail of crystalline basement. (C) Detail of sedimentary units with beds dipping north. (D) Fault planes in sedimentary units antithetic to the major border fault. The faults strike NE with striae presenting low obliquity, indicating NW-SE-oriented extension (green arrows).

2.4.2.3 West Malta Fault

On the Western Malta Fault, the brecciated crystalline basement is in direct tectonic contact with the sedimentary unit of the Antenor Navarro Formation (Fig. 2.5A). The main fault strikes E-W and dips 65°-70° northward (Fig. 2.5A). Measured striae show normal displacement with low obliquity, indicating NNE-SSW-oriented extension. Also, in the footwall damage zone, several WNW-ESE to E-W joints occur (Fig. 2.5B), consistent with the almost pure normal fault kinematics and inferred NNE-SSW-oriented extension. E-W to ENE-WSW-striking minor faults, subparallel to the main border fault, occur in the sedimentary unit (Fig. 2.5C and D). They exhibit left-lateral transtensive kinematics and decimetric displacement, indicating NW-SE-oriented extension. The hanging wall fault damage zone is also dominated by pervasive fault-parallel deformation bands (Fig. 2.5E).

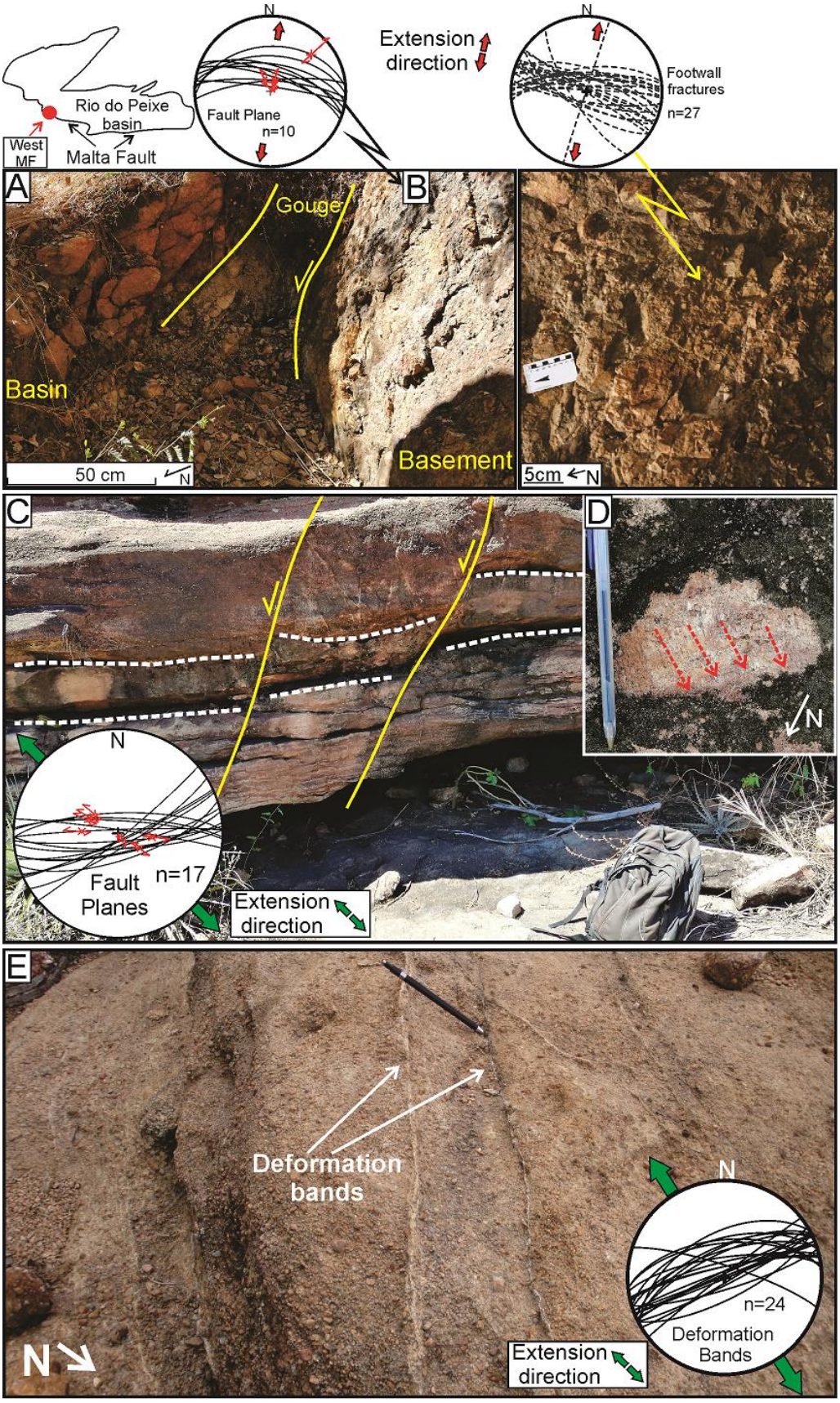

Fig. 2.5 – Outcrop view of West Malta Fault. (A) Contact zone between crystalline basement and sedimentary units of the Antenor Navarro Formation. The border fault plane is WNW-ESE striking with striae towards north. Red arrows indicate the extention

direction of the fault. (B) Detail of WNW-ESE striking open joints in the fault footwall. (C) WSW-ENE left lateral transtensive faults with striae towards NW in the sedimentary unit. Green arrows indicate the extension direction. (D) Detail of fault striae indicating transtensive displacement towards NW. (E) WSW-ENE striking deformation bands in the fault damage zone.

2.4.2.4 East Malta Fault

In the eastern part of the Malta Fault, the crystalline basement is in contact with the sedimentary unit of the Rio Piranhas Formation (Fig. 2.6A). The border fault strikes E-W and dips 65-70° to the north (Fig. 2.6A). Striae on the main fault surface are downdip, indicating NNE-trending extension (Fig. 2.6B). The main fault surface is cross-cut by NNE-striking joints (Fig. 2.6C). The sedimentary unit exhibits a very low deformation grade, preserving its original sedimentary features close to the border fault (Fig. 2.6D). Only a few mm-thick, NE-striking isolated deformation bands exhibit tens of meters spacing (Fig. 2.6E).

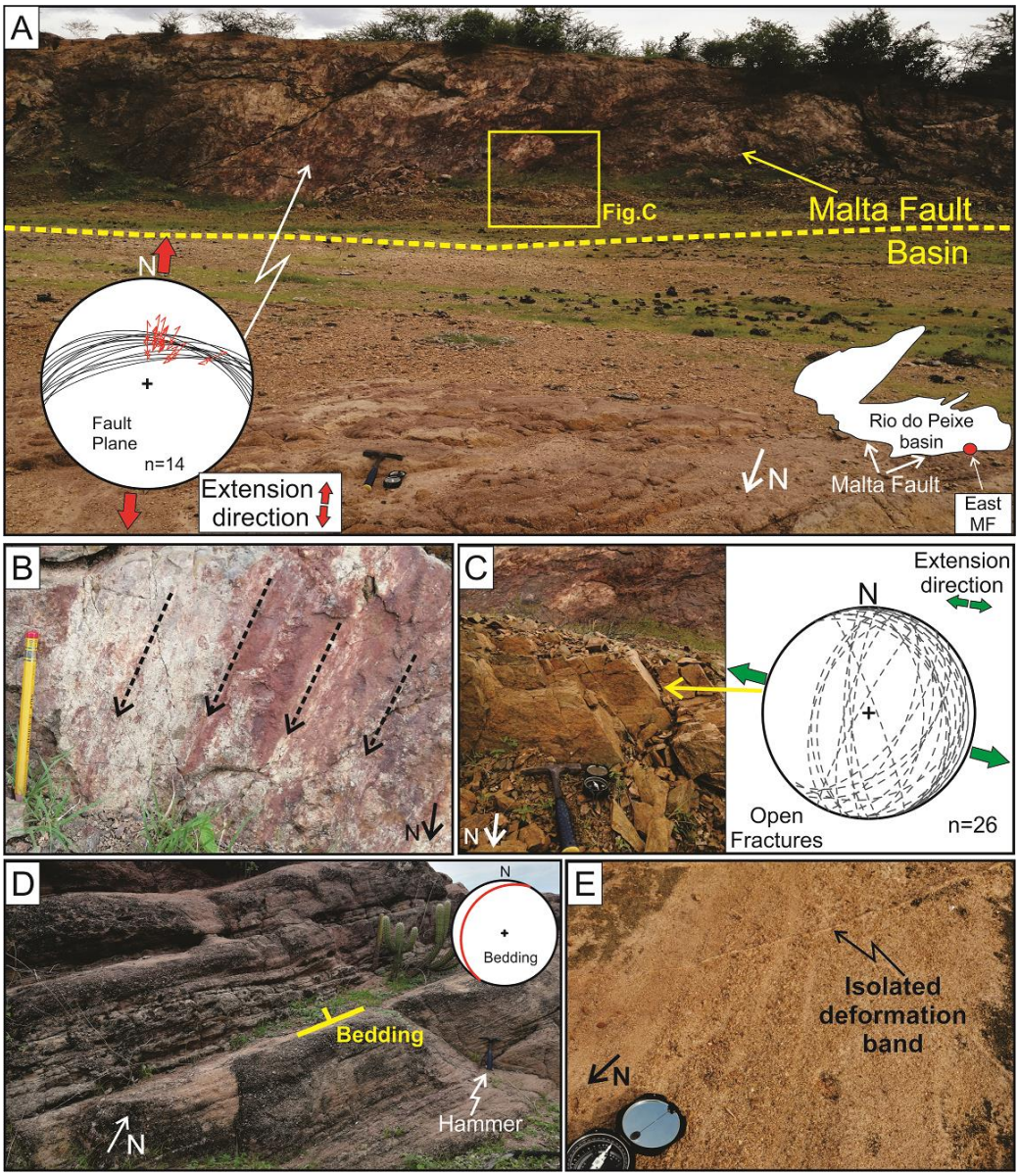

Fig. 2.6 – Outcrop view of East Malta Fault. (A) Major border E-W-striking fault scarp. Striae indicate downdip to right-lateral transtension (B) with a displacement of the hangingwall towards NNE. Red arrows indicate the extension direction. (C) Detail of NNE-striking open joins cross-cutting the mylonitic foliation in the major border fault. Green arrows indicate the extension direction. (D) Non deformed coarse sandstone with bedding dipping NW. (E) Detail of isolated NE-striking deformation band indicated in the damage zone.

2.4.3 AMS data

2.4.3.1 Cumulative statistical analysis

The AMS data from samples collected within the RPB are reported in Tab.2.2. Collectively, the AMS parameters present low anisotropy degrees with P_j values lower than 1.084 and K_{mean} lower than $5.4x10^{-03}$, with predominance of values $<10^{-5}$ (Fig. 2.7E). The shape parameter of most samples from the Antenor Navarro and Sousa formations is

oblate, with magnetic foliation (F) predominant over the magnetic lineation (L) (Fig. 2.7F, also observed as positive T values on Tab. 2.2). Magnetic lineation (L) predominance is observed mainly close to the Western Malta Fault (WMF in Tab. 2.2), where the prolate ellipsoid shape is also highlighted by the negative T values (Tab. 2.2).

Location	Site	Coord_X	Coord_Y	Lithology	N	Kmean	T	L	F	Pj	B0	K1 (D/I)	K3 (D/I)	Paleo-current (AZ)
BFSB	ASH1-2	545979	9251331	Sandstone	20	3.52E-05	0.456	1.009	1.025	1.036	n	132/13	292/75	
BFSB	CAVF	552151	9259450	Sandstone	28	9.48E-05	0.457	1.007	1.02	1.028	350/35	128/08	007/75	310
BFSB	CAV2	552091	9259418	Sandstone	14	4.83E-05	0.641	1.006	1.029	1.038	350/35	179/23	017/65	310
BFSB	MEL2	549894	9258471	Sandstone	10	3.30E-05	0.033	1.003	1.03	1.037	334/14	306/29	134/61	
BFSB	SB1	542990	9258018	Siltstone	10	2.59E-05	-0.611	1.017	1.004	1.023	225/31	301/11	196/54	
BFSB	SS1	547456	9268415	Sandstone	10	5.62E-05	0.546	1.006	1.021	1.029	180/10	136/10	340/79	
BFSB	TRI2	538532	9269211	Sandstone	10	5.57E-05	0.057	1.01	1.011	1.021	159/11	214/18	012/09	
BFSB	UIR1-2	564426	9271895	Sandstone	20	6.53E-05	0.497	1.006	1.019	1.027	283/15	128/07	240/71	
BFSB	UIR3	564413	9271278	Sandstone	10	5.64E-03	0.94	1.002	1.054	1.063	232/15	293/01	030/82	
BFSB	UIR5	564856	9275867	Sandstone	10	8.04E-05	0.649	1.005	1.026	1.033	174/13	179/09	359/80	150
BFSB	UIR6	569049	9278946	Sandstone	10	4.92E-05	0.556	1.007	1.023	1.031	210/06	264/04	016/80	
BFSB	UM1	533058	9264597	Sandstone	9	5.40E-05	0.028	1.003	1.003	1.006	118/20	011/04	104/39	
SSB	MARI1	572331	9244220	Sandstone	12	1.55E-04	0.415	1.012	1.03	1.044	040/59	317/26	210/32	
SSB	MARI2	566468	9244766	Sandstone	17	8.48E-05	0.836	1.004	1.044	1.054	145/04	144/06	339/83	165
SSB	MARI3	569189	9249537	Sandstone	13	1.42E-04	0.693	1.008	1.043	1.056	186/10	275/01	009/77	106
SSB	PER1	576328	9260129	Sandstone	10	8.50E-05	0.757	1.009	1.067	1.084	196/05	149/08	321/81	
SSB	SOC1	583168	9253770	Siltstone	10	1.41E-04	-0.347	1.005	1.002	1.008	179/13	336/82	075/01	
SSB	SOC2	586118	9248867	Siltstone	13	1.63E-04	0.878	1.001	1.012	1.014	200/09	267/07	051/81	230
SSB	SOC3	587844	9245717	Siltstone	16	9.83E-05	0.553	1.003	1.011	1.015	230/11	140/03	000/86	251
SSB	SOC4	590026	9245607	Siltstone	12	6.51E-05	0.368	1.006	1.014	1.02	200/11	202/01	102/87	250
SSB	SSB1	565095	9253257	Siltstone	10	9.30E-05	0.768	1.003	1.021	1.026	164/16	185/14	356/75	
SSB	SSB2	571914	9253105	Siltstone	10	9.69E-05	0.667	1.005	1.024	1.031	180/13	159/08	348/82	305
SSB	UT1	550813	9259755	Sandstone	11	7.67E-05	0.899	1.001	1.022	1.026	148/09	176/06	326/82	
SSB	UTF1	550882	9259832	Sandstone	11	9.46E-05	0.869	1.003	1.038	1.046	145/09	165/03	016/86	165
SSB	UTND	550791	9259479	Sandstone	11	3.29E-05	0.806	1.004	1.04	1.049	170/20	211/03	072/86	
SSB	BDM	592289	9246819	Sandstone	15	2.38E-04	0.792	1.003	1.027	1.033	126/17	036/02	286/84	45
NPOA	UIR4F	565152	9271812	Sandstone	15	9.74E-05	0.549	1.009	1.018	1.029	084/09	190/02	331/87	
NPOA	UIR4D	565109	9271817	Sandstone	10	1.28E-04	0.419	1.012	1.03	1.044	084/09	013/37	151/06	
SPOA	MEL1	550061	9258456	Sandstone	10	9.18E-05	0.033	1.009	1.009	1.018	334/14	021/03	286/65	
SPOA	PIL1	551706	9259424	Sandstone	17	5.32E-05	0.757	1.005	1.018	1.024	269/08	269/06	041/80	
SPOA	PIL2	551692	9259446	Sandstone	12	7.64E-05	0.34	1.011	1.023	1.035	269/08	038/01	270/88	
WMF	DA123	557342	9248477	Sandstone	34	4.80E-05	0.637	1.01	1.044	1.057	008/43	290/02	196/65	
WMF	MF1	560242	9247706	Sandstone	9	2.63E-05	-0.039	1.016	1.014	1.03	024/55	286/14	36/54	
WMF	VE1	546693	9250948	Sandstone	9	2.71E-05	0.546	1.011	1.037	1.051	030/24	151/22	023/56	
WMF	VAR1	550042	9249855	Sandstone	9	5.63E-05	-0.496	1.014	1.005	1.02	043/38	128/37	007/35	40
WMF	VAR2	549886	9249881	Sandstone	12	4.06E-05	-0.355	1.021	1.01	1.032	044/13	155/05	064/13	40
WMF	VAR3	549810	9250154	Sandstone	10	7.14E-05	-0.207	1.011	1.007	1.019	035/20	334/19	193/66	40
WMF	VAR2-F	549998	9249938	Sandstone	29	6.30E-05	-0.579	1.008	1.002	1.01	030/13	149/03	250/73	40
EMF	MFW	587346	9245273	Sandstone	12	1.25E-04	0.74	1.006	1.042	1.053	298/22	27/17	164/67	280
EMF	SES	564317	9243460	Sandstone	11	7.78E-05	0.397	1.003	1.007	1.01	089/39	196/09	074/73	

Tab. 2.1 – Table of AMS data. BFSB = Brejo das Freiras sub-basin. SSB = Sousa sub-basin. NPOA = North Portalegre Fault. SPOA = South Portalegre Fault. WMF = West Malta Fault. EMF = East Malta Fault. N = Number of specimens measured. Kmean = Mean anisotropy of magnetic susceptibility in SI units (Kmean = $k_1+k_2+k_3$). T = Magnetic elipsoid shape parameter (varies from -1 to 1, where negative values indicate prolate shape and positive values indicate oblate shape). L = Magnetic lineation (K_1/K_3). F = Magnetic foliation (K_2/K_3). Pj = Corrected anisotropy degree **(Jelinek, 1981)**. B0 = bedding (in dip strike/dip). K_1 = maximum anisotropy direction (Kmax). K_3 = minimun magnetic anisotropy direction (Kmin). D = K azimuth; I = K inclination.

The magnetic fabric of the whole basin is characterized by NW-SE K1 direction with vertical minimum magnetic susceptibility (K3) (Fig. 2.7A). The same pattern can be observed individually on both Sousa and Brejo das Freiras sub-basins (Fig. 2.7B and C). However, the Gaussian-best-fit statistical analysis of the whole population of K1 values (n=531 data) indicates a bimodal distribution with two main distinct AMS fabrics (and stretching directions) in the whole basin: a main fabric with K1 trending toward NW (N47W±30°), and a second one with K1 trending toward NNE (N32°E±27°) (Fig. 2.7D). A progressive change between the two main directions is inferred, as indicated by the non-well clustered data and the overlapped Gaussian-best-fit curves. The main susceptibility degree (Km) presented very low values (Fig. 2.7E) with oblate ellipsoid shape parameter evidenced by the predominance of magnetic foliation (F) in respect to magnetic lineation (L) (Fig. 2.7F).

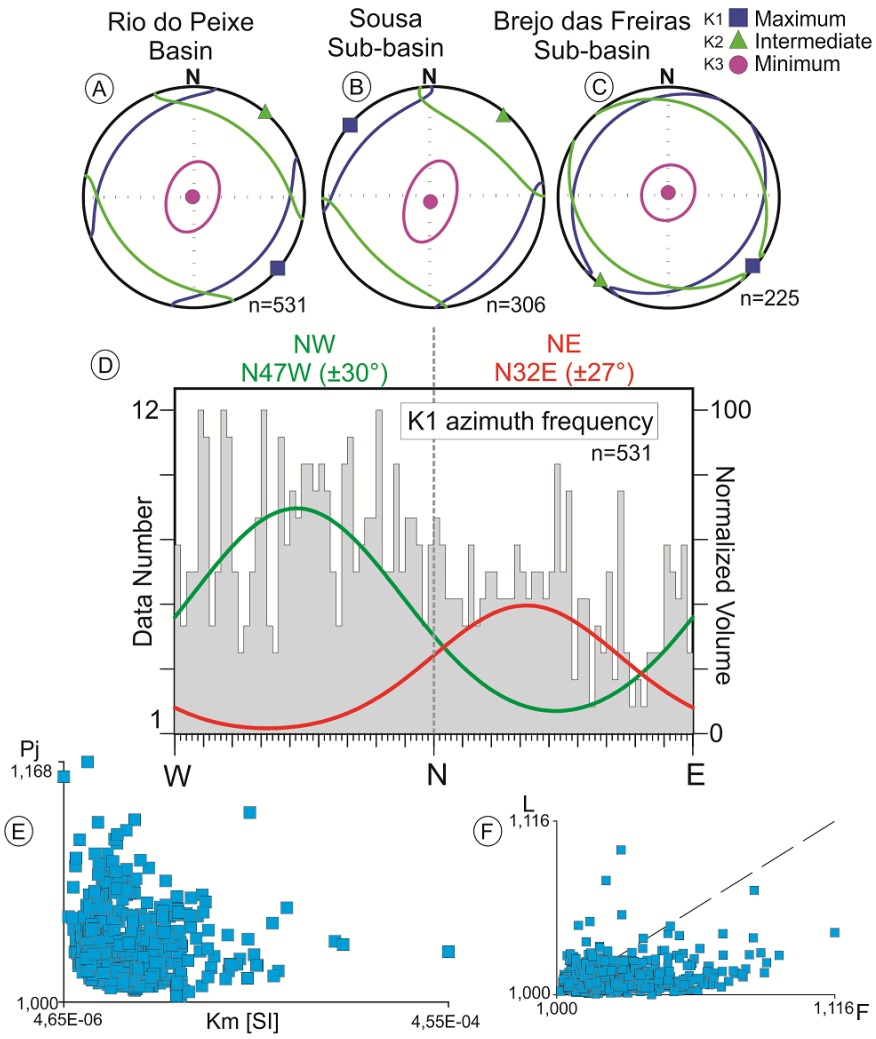

Fig. 2.7 – General AMS data. Stereonet with grouped values in the whole basin (A), Sousa Sub-basin (B) and Brejo das Freiras Sub-basin (C). (D) Histogram with Gaussian-

best-fit statistical analysis of the whole population of K_1 values. (E) Corrected anisotropy degree *versus* Mean anisotropy degree graph. (F) Magnetic lineation *versus* magnetic foliation graph.

2.4.3.2 AMS fabric along the basin

Two distinct magnetic fabrics are observed in sedimentary units of the RPB, NNE and NW trending (Fig. 2.7D). In Fig. 2.8, the mean orientation of K_1 of each sampling site is showed in different color codes for different stretching directions. The NNE-trending magnetic lineation is recorded in samples in the contact zone between sedimentary units and crystalline basement or a few meters away from the border faults. This pattern is observed on either Portalegre or Malta faults. The NNE direction occurs in the northern (Fig. 2.8, samples UIR4F and UIR4D) and southern Portalegre Fault (samples CAV2, PIL2, and MEL1 in Fig. 2.8). On the Eastern Malta fault, the NE trending magnetic lineation is recorded in apparently undeformed sediments located along the contact with the Malta fault (samples SES, MFW, and SOC4 in Fig. 2.8). On the Western Malta Fault region, no clear K_1 NE-direction was observed.

The NW-trending K_1 is dominant in the inner regions of the basin and also close to fault zones (Fig. 2.8). Close to the border faults, the NW-trending K_1 is observed mostly on samples collected in the hangingwall damage zone where NE-trending structures (minor faults and/or deformation bands) are present (Figs. 2.4D and 2.5, South Portalegre Fault and Western Malta Fault, respectively). In the Northern Portalegre Fault, the NW-trending K_1 is was found several meters away from the main fault surface (Fig. 2.8, sample UIR12), where low deformation is observed due to the presence of NNE trending deformation bands (Fig. 2.3C and D). The same AMS fabric is observed in the Southern Portalegre Fault on both deformed zones (Fig. 2.8, samples CAVF and MEL2) and on apparently non-deformed outcrops (sample SB01 in Fig. 2.8). Along the Western Malta Fault (samples VAR2-F, DA123, and MF1 on Fig. 2.8), the NW trending K_1 is predominant is very close to the border fault, where the rock is constantly affected by ~NE-striking extensional faults and deformation bands in sedimentary units. At the Eastern Malta Fault segment, the NW trending K_1 is observed at the western part of the fault (samples MARI1 and MARI2 in Fig. 2.8). At the easternmost region of the East Malta Fault, the NW trending K_1 is well marked in the inner zone of the basin, mostly where the Lagoa do Forno Fault is probably influences the deformation in surface (sample SOC3 in Fig. 2.8).

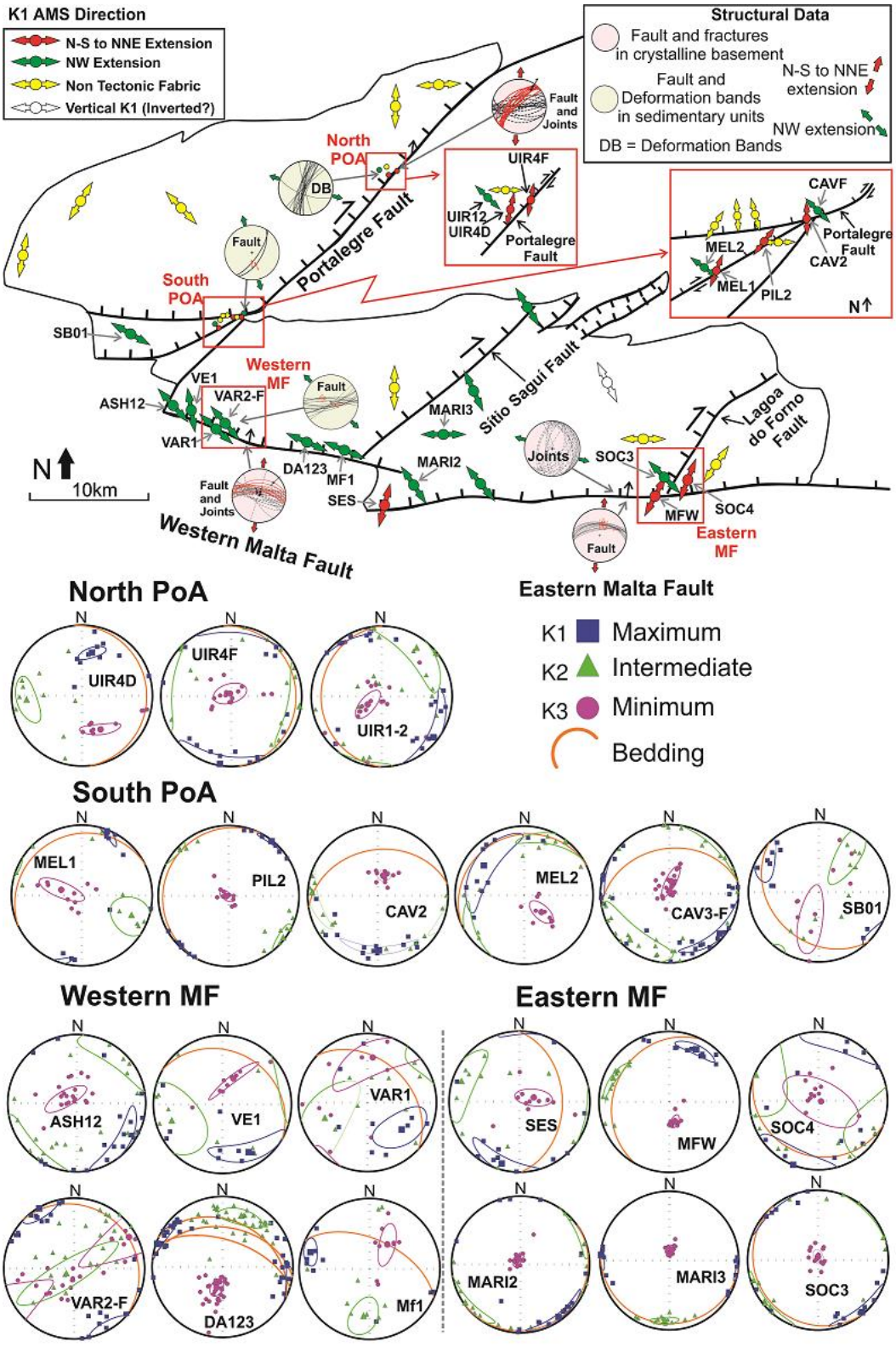

Fig. 2.8 – Map of Rio do Peixe Basin with K_1 direction of sampling sites and stereonet of the samples collected close to the main border faults. Red arrows indicate N-S to NNE-SSW K_1 direction and extension. Green arrows indicate NW-SE K_1 direction and extension. Blue arrows indicate K_1 direction of samples with non-tectonic magnetic fabric (i.e., magnetic fabric influenced by the bedding and/or the paleocurrent). The white arrow indicates vertical K_1 direction with the arrow pointing towards K_2. North POA = North

Portalegre Fault. South POA = South Portalegre Fault. Western MF = Western Malta Fault. Eastern MF = Eastern Malta Fault.

2.5 Discussions

2.5.1 Magnetic fabric of the Rio do Peixe Basin

The magnetic fabric (AMS) of the Rio do Peixe Basin may provide important information about the tectonic opening of the basin, as the main magnetic susceptibility (K_1) direction tend to be parallel to the stretching direction in sedimentary basins (e.g., Rochette et al., 1992; Cifelli et al., 2004; Lanza & Meloni, 2006). As no relevant amount of ferromagnetic minerals (<5%) that could dictate the magnetic fabric was found in our samples (Nicchio et al. submitted), we interpret the acquired magnetic fabric as the result of tectonic deformation or sedimentary features of the rocks (Borradaile & Jackson, 2004; Lanza & Meloni, 2006). In our case, the two different magnetic fabrics inferred from the cumulative Gaussian best-fit statistical analyses of K_1 values (Fig. 2.7D) indicate two main stretching directions responsible for the opening of the basin, i.e., oriented ~N-S to NNE and ~NW. The N-S- to NNE-trending magnetic fabric (K_1) is limited to the contact zone between the crystalline basement and sedimentary units (i.e., in the fault damage zone affecting sedimentary units), and it is concordant with the σ_3 direction inferred from brittle structures recorded in the crystalline basement rocks of both Portalegre and Malta border faults (joints and fault striae) (Fig. 2.8). Conversely, the NW-trending magnetic fabric (K_1) is observed in the inner parts of the basin in apparently undeformed sandstones, and in the hangingwall damage zone sandstone of Portalegre and Malta border faults (Fig. 2.8). The NW magnetic fabric is also concordant with the σ3 direction inferred from minor faults in sedimentary units.

The occurrence of two distinct, mutually orthogonal tectonic magnetic fabrics, recorded in the syn-rift deposits, are concordant with the extension directions (σ_3) inferred from structural data collected along the major border faults. It suggests that two main syn-rift phases were responsible for developing the Rio do Peixe Basin: an early N-S to NNE-SSW stretching direction (syn-rift I) followed by a NW-SE stretching direction (syn-rift II). The following lines of evidence support this relative chronology between the two stretching directions:

1) Structural data showing different extension directions in crystalline basement and sedimentary units (Fig. 2.8). The footwall damage zone of Malta and Portalegre

border faults (i.e., in the crystalline basement rocks) show an extension direction invariably (σ3) oriented N-S to NNE-SSE. In contrast, in the sedimentary rocks, the NW-trending direction is dominant in the inner portions of the basin and along the Malta and Portalegre faults. The general lack of minor faults and deformation bands with a NW-trending extension in the hangingwall damage zone of the Malta fault indicated that, in the first stage of tectonic opening of the basin, the mylonitic foliations in the basement were reactivated under a N-S to NNE-SSW stretching directions. This extension was responsible for the normal and transtensive kinematics of the Malta and Portalegre fault. Subsequently, after sediment infilling, the stretching direction turned to be NW-SE-trending as confirmed by widespread NW-trending σ3 inferred from minor faults and deformation bands in the sedimentary rocks. In other words, a late-stage N-S stretching would have produced subsidiary structures in the hangingwall damage zones indicating N-S extension direction, which are completely lacking along the Malta fault.

2) The Gaussian-best fit statistical analysis of K_1 values (Fig. 2.7D) shows bimodal distribution with predominant NW-oriented data, suggesting that this stretching direction was probably more intense, younger, and likely acted in a longer period than the other stretching direction.
3) Cross-cutting relationship between deformation bands and quartz veins. In the northern Portalegre Fault, the presence of mm-thick quartz veins reopening the NNE-SSW deformation bands (Fig. 2.3D) suggests a late-stage reactivation of previous structures (developed during the right-lateral strike-slip transtension) under a NW-SE-trending stretching direction.
4) The NE-striking open fractures cross-cutting the E-W Eastern Malta Fault (Fig. 2.6C) might also support the interpretation that the NW-SE extension occurs as a second stretching direction during the development of the basin.

We also identified a non-tectonic magnetic fabric mostly far from border faults (with scattered K_3 around the equatorial plane of stereonets) and a vertical magnetic lineation in only one sample (SOC01). Although the magnetic fabric of the sample may coincide with the stress field responsible for the basin inversion (Nogueira et al., 2015; Vasconcelos et al., 2021), our AMS data are not conclusive to discuss the post-rift inversion stage. Additionally, subsurface data suggest that even the main inverted faults within the basin are not sufficiently developed to reach the surface (Vasconcelos et al.,

2021). This indicates that the basin inversion might not be strong enough to change the previously formed magnetic fabric of sedimentary units, thus justifying the lack of AMS data with vertical K_1 along the basin.

2.5.2 - The N-S to NNE extensional tectonics of the Rio do Peixe Basin

The N-S to NNE stretching directions represent the initial opening of the Rio do Peixe Basin, i.e., the syn-rift phase I (Fig. 2.9A). In this stage, the E-W trending mylonitic foliation of the Patos Shear Zone was decisive to the brittle reactivation as it acts as weakness zone, forming the Malta fault with the same strike of the ductile shear zone (Fraçolin et al., 1994; de Castro et al., 2007; Nogueira et al., 2015). During this stage, the N-S to NNE extension resulted in dextral transtensive reactivation of NE-striking Portalegre Fault in its northernmost region. The normal to oblique displacement at its southernmost region of the fault interacted with E-W fault trends forming "horsetail" fault tip geometry (Vasconcelos et al., 2021). The same stretching direction resulted in the early opening of the SSB, forming the E-W striking normal faults dipping towards the north, facilitated by the ductile foliation of the E-W-striking Patos Shear Zone. In the Western Malta Fault, the block movement towards the north affected the former NE-striking ductile shear zones, developing Sitio Saguí fault on dextral transtensive kinematics (Fig. 2.9A). The N-S to NNE extension on the Eastern Malta Fault resulted in normal faulting with down-dip striae towards the north, developing the Lagoa do Forno Fault as a right-lateral transtensive structure. Although the intrabasinal NE-striking faults are blind, seismic data show that both faults occur as negative flower structures (Vasconcelos et al., 2021), strengthening our interpretation. In summary, the early syn-rift brittle faulting followed the former sigmoidal ductile foliation geometry of the basement, imparted by the Portalegre (NE-trending) and Patos (E-W-trending) shear zones, assuming the actual geometry of the Rio do Peixe Basin.

2.5.3 - The NW extensional tectonics of the Rio do Peixe Basin

The NW extension represents the syn-rift phase II of the Rio do Peixe Basin (Fig. 2.9B). This stretching direction, corresponding to the most important AMS fabric, reactivated the former NE-striking faults in a normal shear sense, as the stretching direction is orthogonal to the favorably oriented fault surfaces. This extensional reactivation is observed in the Portalegre Fault (Fig. 2.9B), as well as in subsurface Sitio Saguí and Lagoa do Forno Faults (Vasconcelos et al., 2021) (Fig. 2.9B). As the NW-SE

extension became dominant, the E-W- Malta and E-W-striking south Portalegre faults were reactivated on a left-lateral transtensional sense, as documented by structural data (minor faults and deformation bands) in these sites. The deformation occurs mostly on coarse sandstone units at the southern region of the Portalegre fault zone, reflecting the deep fault reactivation (Araujo et al., 2018). In the BFSB, the faults occur as synthetic and antithetic structures from the basin boundary Portalegre Fault. In the SSB, the deformation is observed at its westernmost region, where NE-striking normal to left-lateral transtensive faults in sediments occurs obliquely from the East Malta E-W Fault. NW extension is barely observed on the West Malta Fault, forming a few NE-striking deformation bands and NNE-trending joints perpendicularly cross-cutting the E-W-striking Malta Fault.

The lack of two distinct populations of K_1 orientations, indicated by the overlap of gaussian-best-fit curves (Fig. 2.7D), suggests that the transition from NNE to NW stretching directions was gradual during the basin development. Therefore, the data indicate that extensional tectonics affected the basin progressively and not in separate phases.

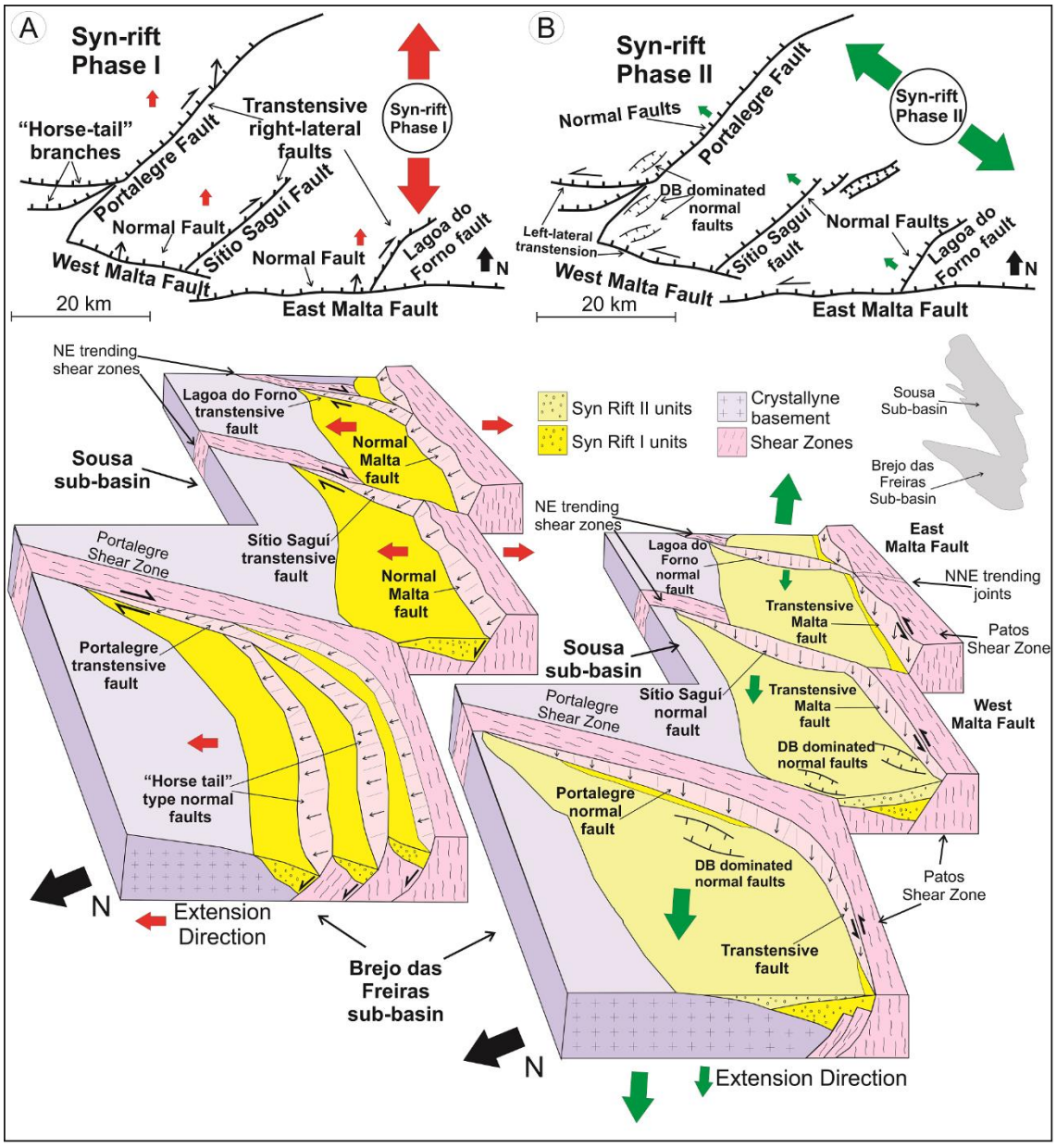

Fig. 2.9 – Schematic model of the syn-rift phase I and II in the Rio do Peixe Basin. (A) Syn-rift phase I. The red arrows indicate the N-S- to NNE-oriented extension forming the E-W-striking Malta Fault, with normal kinematics, and dipping to the north. Consequently, it resulted in right-lateral transtensive faults along the NE-striking Portalegre and other NE-striking faults. They are from, W to E, the Portalegre, Sítio Saguí, and Lagoa do Forno faults. (B) Syn-rift phase II. The green arrows indicate NW-oriented extension. It resulted in the reactivation of the NE-striking Portalegre, Sitio Saguí, and Lagoa do Forno faults. The kinematics had a normal shear sense, dipping to NW and consequently reactivating the E-W-striking Malta fault in a left-lateral transtensive sense. Extensional NE-striking faults and deformation bands (DB) were formed within the basin.

2.5.4 Rio do Peixe Basin rifting and implications for the Pangea breakup

The rifting of the Rio do Peixe Basin is related to the opening of the Atlantic Ocean (Matos, 1992). Therefore, it is important to return to the pre-Pangea breakup configuration to understand the development of the basin (Fig. 2.10). In this pre-basin period, the South American continent was still welded to West Africa, and the intraplate deformation was dominant in NE Brazil (Torsvik et al., 2009; Moulin et al., 2010; de Castro et al., 2012; Matos et al., 2021). Before the Pangea breakup, the South American continent was subjected to a counterclockwise stress rotation. Although the angle of such rotation is not clear after the pre-breakup interval, considering today's geographic position, the total continent rotation reached up to 40-50^0 with respect to West Africa (Moulin et al., 2010). Therefore, the two stretching directions found in this study and acting during the rifting phase were oriented ~NNW-SSE (syn-rift I; N32°E - 45°) and ~E-W (syn-rift II, N47°W - 45°), respectively.

Considering the actual geographic position of the South American continent, the N-S extension during the pre-breakup of Pangea was documented by several studies focused on plate reconstruction (Eagles & König, 2008; Torsvik et al., 2009; Moulin et al., 2010; Heine et al., 2013). This stretching direction was likely caused by the clockwise rotation of the South American continent with respect to Africa during the Cretaceous (Matos, 1992, 2021; Françolin et al., 1994), with the regional rotation pole located at the junction of the Transbrasiliano and the Trans-Saharan lineaments (Matos et al., 2021). Thus, when the RPB Rio do Peixe Basin started developing (145 Ma) (Nóbrega et al., 2005) the Patos and Portalegre Shear Zones were oriented NE and N-S, respectively (Fig. 2.10).

Matos et al. (2021) subdivided the South Atlantic Cretaceous Rift System into six distinct structural segments, including the Rio do Peixe Basin in the Cariri Rift Valley, affectec by the NNW-SSE extension of the orthogonal branch. This zone was affected by dextral oblique-slip kinematics that lasted until the Barremian (Nóbrega et al., 2005; Matos et al., 2021) accommodated along the Transbrasiliano shear zone (Almeida et al., 2000) (Fig. 2.10A). The NNW-SSE extension in the Rio do Peixe Basin area would be the result of the right-lateral strike-slip motion of the NNE-trending continental ductile shear zones. It matches with our NNE-oriented extension of syn-rift phase I data (Fig. 2.10B) once the continent rotation of ~45^{0}is considered (Moulin et al., 2010). As the Lower Cretaceous rift developed, the E-W-oriented σ3 was associated with the South Atlantic opening and continuously migrated towards the north (Eagles, 2007) up to the

Rio do Peixe Basin, thus progressively becoming the dominant stretching direction in this stage (Fig. 2.10C). As the E-W extension occurred with higher velocities at the southern part of the South Atlantic, the South American Plate was forced to rotate clockwise (Heine et al., 2013), thus gradually increasing the contribution of the E-W-oriented extension in the Borborema Province, changing the stress field in the Rio do Peixe Basin and further reactivating the basin-boundary Portalegre and Malta faults (Fig. 2.10A and C). The forced continent rotation resulted in gradual normal stress-field rotation from NNW-SSE to E-W (cf. Heine et al., 2013). The overlap of K_1 data distribution (Fig. 2.7) allows us to infer that the rotation in the stretching directions is progressive, rather than a sudden switch imparted by two distinct syn-rift stages.

The exact age when the E-W-oriented extension became stronger than the NNW extension at Rio do Peixe Basin is not clear, as geochronological data is scarce in the Rio do Peixe basin. However, Matos et al. (2021) used the Mesozoic Equatorial Atlantic Magmatic Province (EQUAMP) (Hollanda et al., 2019), which they called Borborema Giant Dyke, as a controlling factor of the rifting age in the whole Borborema Province. In the RPB area, this event is rouhly NE-oriented, suggesting a NW-SE-extension (in today's north position, and ~E-W- oriented extension in Pre-Pangea Breakup north position). The age of this event is 135-120 Ma. Thus, in our model (Fig. 2.10C and D), we interpret that the ~E-W-oriented extension became the most influent in the Rio do Peixe Basin between 135-125 Ma, as the intraplate deformation has ceased at the Aptian-Albian boundary ~120Ma (Moulin et al., 2010; Heine et al., 2013).

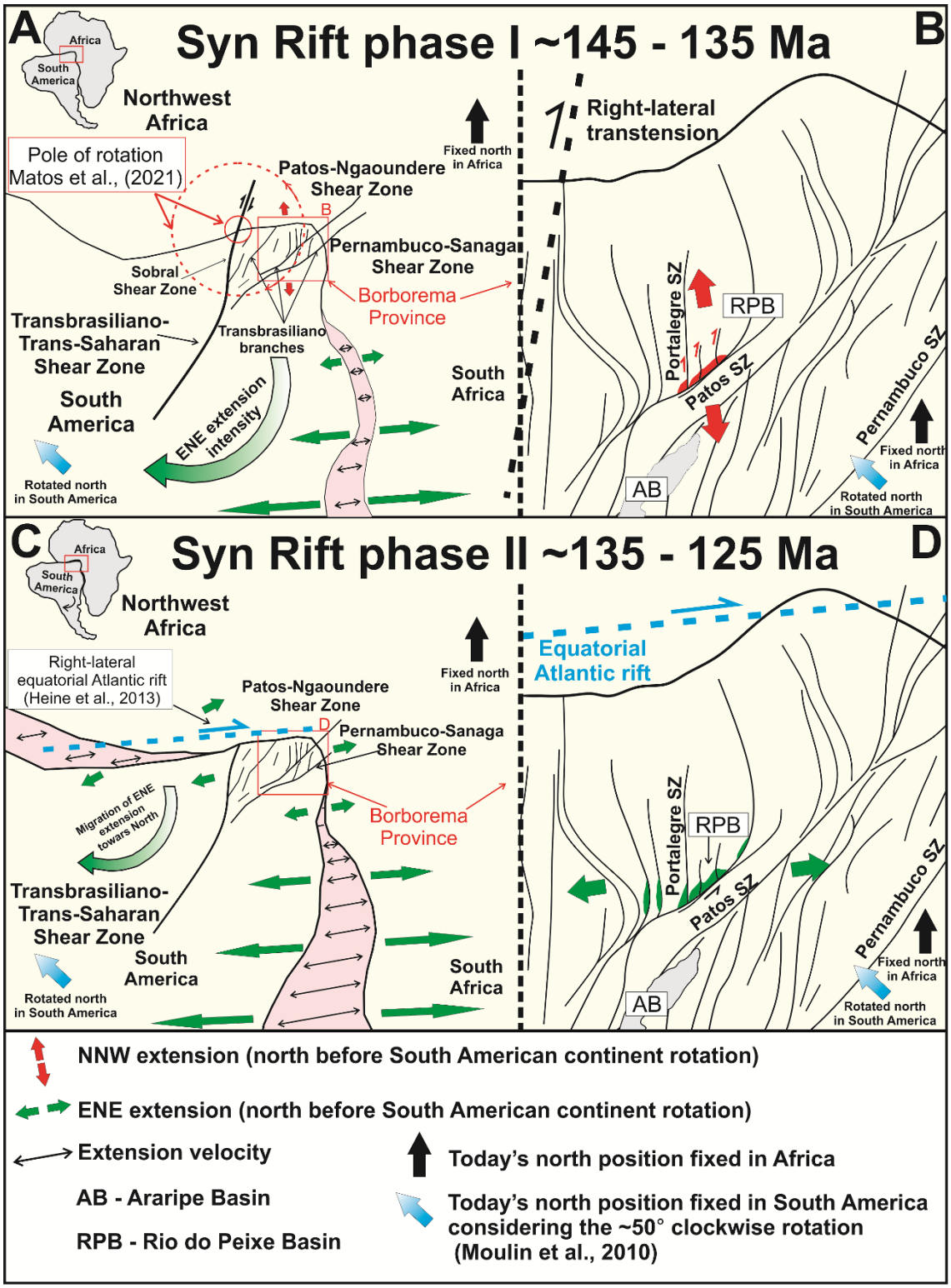

Fig. 2.10 – Schematic model of the Pangea breakup with emphasis on the Borborema Province and Rio do Peixe Basin with north rotated anticlockwise considering the geographic north position in the South America during the pre-breakup (modified from Moulin et al., 2010). (A) Syn-rift phase I scheme during the initial rotational stress in the South American continent. The ENE-oriented extension started the breakup in the south of the South America continent, with stretching intensity gradually migrating northwards. In the Borborema Province, the rotation of the stress field generated a right-lateral transtension along the Transbrasilian-Trans-Saharan shear zones with the rotation pole at

their intersection (Matos et al., 2021). It resulted in the NNW-oriented distension in Transbrasilian Shear Zone branches such as the NE-trending (on the Cretaceous north position in South America continent) Patos Shear Zone and the opening of the Rio do Peixe Basin (B). (C) Syn-rift phase II scheme. The development of the South Atlantic opening gradually increased the intensity of the ENE extension towards the north, arriving in the Borborema Province. (D) The start of the ENE stretching at the Borborema Province resulted in reactivation of the N-S faults in Rio do Peixe Basin, changing the main stretching direction to the ENE trend. On today's north position, N-S structures became NE-striking, and NE structures became E-W-striking.

2.5 Conclusions

In this study, we combined AMS and structural data to interpret the strain trajectories responsible for opening the Rio do Peixe Basin. Our data show that two distinct main stretching directions, diverging about 79^0, occurred during rifting. The stretching direction gradually rotated counterclockwise from NNE-SSW to NW-SE due to the intraplate stress rotations in a pre-Pangea breakup period.

The NNE-SSW-oriented stretching controlled the syn-rift phase I, marking the initial opening stage of the basin during the Berriasian. This extension resulted in right-lateral displacement of the Transbrasiliano-Trans-Saharian shear zones. In the SSB, this phase caused the initial brittle deformation on the normal Malta Fault, striking E-W and dipping to north. Due to movement of blocks towards the north, the right-lateral transtensive NE-striking Sítio Saguí and Lagoa do Forno faults were formed, facilitated by former NE-striking Precambrian shear zones. The deformational pattern was repeated in the BFSB, with E-W inflection of the Portalegre Fault. It opened as a normal fault with hangingwall movement towards the north, resulting in right-lateral transtensive displacement of the NE-striking Portalegre Fault.

The NW-SE-oriented stretching was associated with the syn-rift phase II. It marked the increasing of the intensity of the E-W extension (considering the geographic north position in South America before the continent rotation) on northeast Brazil and West Africa that gradually migrated northwards during the opening of the South Atlantic. In the Rio do Peixe Basin, this stretching direction lasted from the Barremian to late Aptian, when the continent breakup started at the northern part of the Borborema Province, Brazil. During the syn-rift phase II of the basin, NE trending faults became the most relevant to the continuous opening of the basin, reactivating in a normal sense. The new extension direction resulted in left-lateral transtension of the E-W trending border faults with block movement towards NW. This pattern was repeated on both Sousa and Brejo das Freiras

sub-basins. NE-striking extensional faults were formed in the basin, reflecting the deep fault reactivation. Our results indicate that integrating structural and AMS data can be used for tectonic reconstructions and to infer the progressive evolution of the tectonic stress field in intraplate settings.

Acknowledgments

We are greatful to the Brazilian Oil Company Petrobras that funded the DEBRIP Project (TC 5850.0109438.18.9) coordinated by Francisco C. C. Nogueira (UFCG).

References

Almeida, F. F. M. De, Brito Neves, B. B. De, & Dal Ré Carneiro, C. (2000). The origin and evolution of the South American platform. Earth Science Reviews, 50(1–2), 77–111. https://doi.org/10.1016/S0012-8252(99)00072-0

Arai, M. (2006). Revisão estratigráfica do Cretáceo inferior das bacias interiores do Nordeste do Brasil. Geociencias, 25(1), 7–15.

Araujo, R. E. B., Bezerra, F. H. R., Nogueira, F. C. C., Balsamo, F., Carvalho, B. R. B. M., Souza, J. A. B., et al. (2018a). Basement control on fault formation and deformation band damage zone evolution in the Rio do Peixe Basin, Brazil. Tectonophysics, 745(August), 117–131. https://doi.org/10.1016/j.tecto.2018.08.011

Araujo, R. E. B., Bezerra, F. H. R., Nogueira, F. C. C., Balsamo, F., Carvalho, B. R. B. M., Souza, J. A. B., et al. (2018b). Basement control on fault formation and deformation band damage zone evolution in the Rio do Peixe Basin, Brazil. Tectonophysics, 745(August), 117–131. https://doi.org/10.1016/j.tecto.2018.08.011

Borradaile, Graham J., & Jackson, M. (2004). AMS: magnetic petrofabrics of deformed rocks.

Borradaile, Graham John. (1988). Magnetic susceptibility, petrofabrics and strain. Tectonophysics, 156, 1–20.

de Castro, D. L., de Oliveira, D. C., & Gomes Castelo Branco, R. M. (2007a). On the tectonics of the Neocomian Rio do Peixe Rift Basin, NE Brazil: Lessons from gravity, magnetics, and radiometric data. Journal of South American Earth Sciences, 24(2–4), 184–202. https://doi.org/10.1016/j.jsames.2007.04.001

de Castro, D. L., de Oliveira, D. C., & Gomes Castelo Branco, R. M. (2007b). On the tectonics of the Neocomian Rio do Peixe Rift Basin, NE Brazil: Lessons from gravity, magnetics, and radiometric data. Journal of South American Earth Sciences, 24(2–4), 184–202. https://doi.org/10.1016/j.jsames.2007.04.001

Celestino, M. A. L., Miranda, T. S. de, Mariano, G., Alencar, M. de L., Carvalho, B. R. B. M. de, Falcão, T. da C., et al. (2020). Fault damage zones width: Implications for the tectonic evolution of the northern border of the Araripe Basin, Brazil, NE Brazil. Journal of Structural Geology, 138(June). https://doi.org/10.1016/j.jsg.2020.104116

Cifelli, F., Mattei, M., Chadima, M., Hirt, A. M., & Hansen, A. (2005). The origin of tectonic lineation in extensional basins: Combined neutron texture and magnetic analyses on "undeformed" clays. Earth and Planetary Science Letters, 235(1–2), 62–78. https://doi.org/10.1016/j.epsl.2005.02.042

Cifelli, Francesca, Rossetti, F., Mattei, M., Hirt, A. M., Funiciello, R., & Tortorici, L. (2004). An AMS, structural and paleomagnetic study of quaternary deformation in eastern Sicily. Journal of Structural Geology, 26(1), 29–46. https://doi.org/10.1016/S0191-8141(03)00092-0

Dyer, R. (1988). Using joint interactions to estimate paleostress ratios. Journal of Structural Geology, 10(7), 685–699. https://doi.org/10.1016/0191-8141(88)90076-4

Eagles, G. (2007). New angles on South Atlantic opening. Geophysical Journal International, 168(1), 353–361. https://doi.org/10.1111/j.1365-246X.2006.03206.x

Eagles, G., & König, M. (2008). A model of plate kinematics in gondwana breakup. Geophysical Journal International, 173(2), 703–717. https://doi.org/10.1111/j.1365-246X.2008.03753.x

Faccenna, C., Speranza, F., Caracciolo, F. D. A., Mattei, M., & Oggiano, G. (2002). Extensional tectonics on Sardinia (Italy): Insights into thearc-back-arc transitional regime. Tectonophysics, 356(4), 213–232. https://doi.org/10.1016/S0040-1951(02)00287-1

Françolin, J. B. L., Cobbold, P. R., & Szatmari, P. (1994). Faulting in the Early Cretaceous Rio do Peixe basin (NE Brazil) and its significance for the opening of the Atlantic, 16(5), 647–661.

Frizon De Lamotte, D., Fourdan, B., Leleu, S., Leparmentier, F., & De Clarens, P. (2015). Style of rifting and the stages of Pangea breakup. Tectonics, 34(5), 1009–1029. https://doi.org/10.1002/2014TC003760

García-Lasanta, C., Oliva-Urcia, B., Casas-Sainz, A. M., Román-Berdiel, T., Izquierdo-Llavall, E., Soto, R., et al. (2018). Inversion tectonics and magnetic fabrics in Mesozoic basins of the Western Tethys: A review. Tectonophysics, 745(August), 1–23. https://doi.org/10.1016/j.tecto.2018.08.005

Heine, C., Zoethout, J., & Müller, R. D. (2013). Kinematics of the South Atlantic rift. Solid Earth, 4(2), 215–253. https://doi.org/10.5194/se-4-215-2013

Jelinek, V. (1981). Characterization of the magnetic fabric of rocks. Tectonophysics, 79(3–4), 63–67. https://doi.org/10.1016/0040-1951(81)90110-4

Lanza, R., & Meloni, A. (2006). The Earth's Magnetism. An introduction for geologists. Berlin: Springer.

Lourenço, M. C. M., Jardim De Sá, E. F., Córdoba, V. C., & Pichel, L. M. (2021). Multi-scale tectono-stratigraphic analysis of pre- and syn-rift sequences in the Rio do Peixe Basin, NE Brazil. Marine and Petroleum Geology, 130(May). https://doi.org/10.1016/j.marpetgeo.2021.105127

de Matos, R. M. D. (1992). The Northeast Brazilian Rift System. Tectonics, 11(4), 766–791. https://doi.org/10.4324/9780203494219-10

Matos, Renato M.Darros de, Medeiros, W. E., Jardim de Sá, E. F., Almeida, C. B. de, Norton, I., & Córdoba, V. C. (2021). A solution to the Albian fit challenge between the South American and African plates based on key magmatic and sedimentary events late in the rifting phase in the Pernambuco and Paraíba basins. Marine and Petroleum Geology, 128(September 2020). https://doi.org/10.1016/j.marpetgeo.2021.105038

Moulin, M., Aslanian, D., & Unternehr, P. (2010). A new starting point for the South and Equatorial Atlantic Ocean. Earth-Science Reviews, 98(1–2), 1–37. https://doi.org/10.1016/j.earscirev.2009.08.001

Nicchio, M. A., Nogueira, F. C. C., Balsamo, F., Souza, J. A. B., Carvalho, B. R. B. M., & Bezerra, F. H. R. (2018). Development of cataclastic foliation in deformation

bands in feldspar-rich conglomerates of the Rio do Peixe Basin, NE Brazil. Journal of Structural Geology, 107(December 2017), 132–141. https://doi.org/10.1016/j.jsg.2017.12.013

Da Nóbrega, M. A., Sá, J. M., Bezerra, F. H. R., Hadler Neto, J. C., Iunes, P. J., Guedes, S., et al. (2005). The use of apatite fission track thermochronology to constrain fault movements and sedimentary basin evolution in northeastern Brazil. Radiation Measurements, 39(6), 627–633. https://doi.org/10.1016/j.radmeas.2004.12.006

Nogueira, F C C, Nicchio, M. A., Balsamo, F., Souza, J. A. B., Silva, I. V. L., Bezerra, F. H. R., et al. (2021). The influence of the cataclastic matrix on the petrophysical properties of deformation bands in arkosic sandstones. Marine and Petroleum Geology, 124(November 2020), 15. https://doi.org/10.1016/j.marpetgeo.2020.104825

Nogueira, Francisco C C, de Castro, D. L., & de Oliveira, M. S. (2004). Estudo Magnético e Gravimétrico do Arcabouço Estrutural da Bacia Rio do Peixe - PB. Revista de Geologia, 17 (1), 74–87.

Nogueira, Francisco C C, Marques, F. O., Bezerra, F. H. R., de Castro, D. L., & Fuck, R. A. (2015). Cretaceous intracontinental rifting and post-rift inversion in NE Brazil: Insights from the Rio do Peixe Basin. Tectonophysics, 644, 92–107. https://doi.org/10.1016/j.tecto.2014.12.016

Nogueira, Francisco Cezar Costa, Oliveira, M. S. De, & Castro, D. L. De. (2004). Estudo Magnético e Gravimétrico do Arcabouço Estrutural da Bacia Rio do Peixe – PB. Revista de Geologia, 17(1), 74–87.

Peace, A. L., Phethean, J. J. J., Franke, D., Foulger, G. R., Schiffer, C., Welford, J. K., et al. (2020). A review of Pangaea dispersal and Large Igneous Provinces – In search of a causative mechanism. Earth-Science Reviews, 206(March 2019), 102902. https://doi.org/10.1016/j.earscirev.2019.102902

Peralta Gomes, C., Fossen, H., de Almeida, R. P., & Salmoni, B. (2018). Subseismic deformation in the Vaza-Barris Transfer Zone in the Cretaceous Recôncavo-Tucano-Jatobá rift system, NE Brazil. Journal of Structural Geology, 117(May), 81–95. https://doi.org/10.1016/j.jsg.2018.09.007

Pontes, C. C. C., Nogueira, F. C. C., Bezerra, F. H. R., Balsamo, F., Miranda, T. S.,

Nicchio, M. A., et al. (2019). Petrophysical properties of deformation bands in high porous sandstones across fault zones in the Rio do Peixe Basin, Brazil. International Journal of Rock Mechanics and Mining Sciences, 114(November 2018), 153–163. https://doi.org/10.1016/j.ijrmms.2018.12.009

Porreca, M., & Mattei, M. (2012). AMS fabric and tectonic evolution of Quaternary intramontane extensional basins in the Picentini Mountains (southern Apennines, Italy). International Journal of Earth Sciences, 101(3), 863–877. https://doi.org/10.1007/s00531-011-0670-2

Rapozo, B. F., Córdoba, V. C., & Antunes, A. F. (2021a). Tectono-stratigraphic evolution of a cretaceous intracontinental rift: Example from Rio do Peixe Basin, north-eastern Brazil. Marine and Petroleum Geology, 126(January). https://doi.org/10.1016/j.marpetgeo.2021.104899

Rapozo, B. F., Córdoba, V. C., & Antunes, A. F. (2021b). Tectono-stratigraphic evolution of a cretaceous intracontinental rift: Example from Rio do Peixe Basin, north-eastern Brazil. Marine and Petroleum Geology, 126(December 2020). https://doi.org/10.1016/j.marpetgeo.2021.104899

Rochette, P., Jackson, M., & Aubourg, C. (1992). Rock magnetism and the interpretation of anisotropy of magnetic susceptibility. Reviews of Geophysics, 30(3), 209–226.

Schwehr, K., & Tauxe, L. (2003). Characterization of soft-sediment deformation: Detection of cryptoslumps using magnetic methods. Geology, 31(3), 203–206. https://doi.org/10.1130/0091-7613(2003)031<0203:COSSDD>2.0.CO;2

Sénant, J., & Popoff, M. (1991). Early Cretaceous extension in northeast Brazil related to the South Atlantic opening. Tectonophysics, 198(1), 35–46. https://doi.org/10.1016/0040-1951(91)90129-G

Sousa, A. D. J. e, Carvalho, I. D. S., & Ferreira, E. P. (2018). Western Gondwana non-marine ostracods from Early Cretaceous low- latitude ephemeral lake , Northeastern Brazil. Journal of South American Earth Sciences, 86(June), 23–37. https://doi.org/10.1016/j.jsames.2018.06.001

de Souza, D. H. S., Nogueira, F. C. C., Vasconcelos, D. L., Torabi, A., Souza, J. A. B., Nicchio, M. A., Pérez, Y. A. R., Balsamo, F. (2021). Growth of cataclastic bands into a fault zone: A multiscalar process by microcrack coalescence in sandstones of

Rio do Peixe Basin, NE Brazil. Journal of Structural Geology, 146(August 2020). https://doi.org/10.1016/j.jsg.2021.104315

Szatmari, P., Françolin, J. B. L., Zanotto, O., & Wolff, S. (1987). Evolução Tectônica Da Margem Equatorial Brasileira. Revista Brasileira de Geociências, 17(2), 180–188. https://doi.org/10.25249/0375-7536.1987180188

Teh-Quei Lee, Kissel, C., Laj, C., Chorng-Shern Horng, & Yi-Teh Lue. (1990). Magnetic fabric analysis of the Plio-Pleistocene sedimentary formations of the Coastal Range of Taiwan. Earth and Planetary Science Letters, 98(1), 23–32. https://doi.org/10.1016/0012-821X(90)90085-C

Torsvik, T. H., Rousse, S., Labails, C., & Smethurst, M. A. (2009). A new scheme for the opening of the South Atlantic Ocean and the dissection of an Aptian salt basin. Geophysical Journal International, 177, 1315–1333. https://doi.org/10.1111/j.1365-246X.2009.04137.x

Vasconcelos, D. L., Marques, F. O., Nogueira, F. C. C., Perez, Y. A. R., Bezerra, F. H. R., Stohler, R. C., & Souza, J. A. B. (2020). Tectonic inversion assessed by integration of geological and geophysical data: The intracontinental Rio do Peixe Basin, NE Brazil. Basin Research, (March), 1–24. https://doi.org/10.1111/bre.12491

Vasconcelos, D. L., Marques, F. O., Nogueira, F. C. C., Perez, Y. A. R., Bezerra, F. H. R., Stohler, R. C., & Souza, J. A. B. (2021). Tectonic inversion assessed by integration of geological and geophysical data: The intracontinental Rio do Peixe Basin, NE Brazil. Basin Research, 33(1), 705–728. https://doi.org/10.1111/bre.12491

Hollanda, M.H.B.M., Archanjo, C.J., Macedo Filho, A.A., Fossen, H., Ernst, R.E., Castro, D. L. de, Melo, A.C., Oliveira, A.L., 2019. The mesozoic equatorial atlantic magmatic province (EQUAMP). A new large igneous province in South America. In: Book: Dyke Swarms of the World: A Modern Perspective. https://doi.org/10.1007/ 978-981-13-1666-1_3.

Peralta Gomes, C., Fossen, H., Almeida, R.P. de, Salmoni, B., 2018. Subseismic deformation in the Vaza-Barris Transfer Zone in the Cretaceous Recôncavo-Tucano-Jatobá rift system, NE Brazil. Journal of Structural Geology 117, 81–95. https://doi.org/10.1016/j.jsg.2018.09.007

Chapter 3 - The effect of fault-induced compaction on petrophysical properties of deformation bands in poorly lithified sandstones

This chapter is presented in the form of a manuscript that is under review in the Journal of Structural Geology. In this work we describe the effects of progressive deformation on silisciclastic reservoir. In a multidisciplinary approach, we used structural, miscrostructural, chemical, petrophysical and geomechanical data to characterize the effects of fault-induced rock compaction on the strain intensity and sealing behavior of siliciclastic reservoir, were deformation bands are frequent on faulted zones. As main conclusion, we proposed a strain evolution model where the fault-induced compaction dictates the strain intensity and the sealing potential of subsequent deformation bands in siliciclastic reservoirs.

SUBMITED ARTICLE

Matheus Amador Nicchio[a, *]; Fabrizio Balsamo[a]; Francisco Cézar Costa Nogueira[b]; Luca Aldega[c]; Cayo Cesar Cortez Pontes[d]; Francisco Hilario Rego Bezerra[d]; Jorge André Braz de Souza[e]

[a] Department of Chemistry, Life Science and Environmental Sustainability, University of Parma, Parma, Italy;
[b] Universidade Federal da Campina Grande, Campina Grande, PB, Brazil;
[c] Dipartimento di Scienze dela Terra, Sapienza Università di Roma, Rome, Italy;
[d] Universidade Federal Do Rio Grande Do Norte, Natal, RN, Brazil;
[e] Petrobras Research Center, Rio de Janeiro, RJ, Brazil.

Submitted to: *Journal of Structural Geology (JSG).* Submission code: *SG-S-21-00416*

Date of submission: 15/11/2021

Status of submission: Under review

Abstract

We studied the impact of fault-induced compaction on deformation band's petrophysical properties developed in poorly lithified sandstones of the Rio do Peixe Basin, Brazil. We compared undeformed sandstone and deformation bands associated with syn-rift normal faults and post-rift strike-slip faults by integrating structural, petrophysical, mineralogical and uniaxial compressive strength (UCS) measurements. The sealing behavior was interpreted from capillary pressure obtained from mercury injection porosimetry and in situ air permeability. Host rock consists of poorly lithified

sandstone with 25-30% porosity, permeability of 1.3 Darcy, capillary pressure of 5 psi, and UCS of 20 MPa. The normal faults developed from soft-sediment conditions with moderate to intense cataclasis, and resulted in an overall fault zone compaction with localized porosity and permeability loss in deformation bands (reaching 10% and 12 mD) and rock volumes between deformation bands (reaching 20% and 0.7 Darcy, respectivelly). Compared to syn-rift deformation bands, the strike-slip deformation bands show similar porosity (12-13%), but lower permeability (1-10 mD) and greater capillary pressures (up to 114 psi). Minerals identified in XRD analysis indicates that both syn-rift and post-rift faults formed under similar shallow burial depths (< 1-2 km). In the end, we propose a model that quantifies fault-induced compaction and may predict fault sealing in deformation bands-dominated sandstone reservoirs.

Keywords: Faults, deformation bands, clay mineralogy, petrophysical properties

3.1 Introduction

Fault zones architecture and related permeability structures exert primary control on fluid flow and mechanical properties of rocks, mainly by changing textural, petrophysical and hydraulic properties during deformation (Torabi and Fossen, 2009; Balsamo et al., 2010; Ballas et al., 2015; Pontes et al., 2019). The changes of fault rock properties are caused by deformation processes that depends on several factors such as host rock properties (e.g., mineralogy, porosity and grain size), burial depth of deformation (i.e., confining pressure), and fault displacement (e.g; Caine et al., 1996; Balsamo and storti, 2011; Ballas et al., 2012, 2015; Exner and Tschegg, 2012; Fossen et al., 2017).

The tectonic setting also plays a vital role in the evolution of fault zone properties by modulating the amount of cataclasis, fracture geometry, and petrophysical properties (Soliva et al., 2013, 2016; Ballas et al., 2015; Balsamo et al., 2019). Additionally, other factors can modify the rheology of deformed rocks and related permeability, such as compaction induced by increasing burial depth (Beke et al., 2019), selective cementation within fault zones (Williams et al., 2017; Pizzati et al., 2020) and the inheritance from pre-existing faults (Gajst et al., 2018).

In porous sandstones, deformation bands (DB) are common in fault damage zones and can occur as single DB or as DB clusters, depending on the intensity of the

deformation (Fossen et al., 2017). DB clusters can be localized further within the core of fault zone, incorporating small shear surface (slip surfaces) (e.g Torabi et al., 2021; Shipton et al., 2006).

Several works investigated the importance of DBs on siliciclastic reservoirs properties, thus classifying them as baffle and seal structures, mainly due to the cataclasis intensity (e.g., Fossen et al., 2017; Nogueira et al., 2021 and references therein). The most important factors controlling the petrophysical properties of deformation bands are (i) the distance from the master fault (Smeraglia et al., 2014), (ii) the depth at which deformation occurs (Beke et al., 2019), (iii) the pristine host rock petrophysical properties such as lithification degree, porosity, grain size and mineralogy (Ballas et al., 2015), (iv) amount of shear displacement (Pizzati et al., 2020) and (v) the tectonic setting (Soliva et al., 2013, 2016; Ballas et al., 2014). Although several works investigated factors controlling petrophysical properties of deformation bands in high-porosity sandstone (e.g., Ballas et al., 2015; Soliva et al., 2016; Philit et al., 2018), the role of progressive compaction during sin- to post-rift deformation band evolution, i.e., the porosity loss of rock volumes imparted by fault slip accumulation on the deformation bands attibutes is still not well understood. This work documents the role of fault-induced tectonic compaction on the petrophysical and microstructural properties of deformation bands affecting high-porosity feldspar-rich coarse sandstones of the Rio do Peixe Basin, Brazil (Fig. 3.1A). To this end, we compared two different sets of fault-related deformation bands developed at different times, with different kinematics and deformation style during the overall activity of the major basin-boundary, Portalegre fault. We compared structural, microstructural, geomechanical, air-permeability, and Hg-injection porosity data from host rocks and two sets of deformation bands. Further, we performed XRD mineralogical analyses on host sandstones (bulk and clay fractions) to evaluate the maximum burial depth experienced by the rocks and its effect on the observed changes of DBs petrophysical properties. Our results indicate that DBs, developed under normal kinematics during the early stage of deformation, have permeability reduction of 1-2 order of magnitude with respect to the undeformed sandstone and a capillary pressure threshold of about 45 psi. DBs developed under strike-slip kinematics in a later stage of deformation have permeability reduction up to 3 orders of magnitude and greater capillary pressure threshold of 100 psi. X-ray diffraction shows a smectite-risch assemblage, consistent with shallow burial depths (<1-2 km), thus suggesting that petrophysical differences are not induced by greater confining

pressures during the development of strike-slip DBs, but rather depend on the overall strength increase of the strength of the host sandstone as new faults nucleate and new bands are being formed (i.e., tectonic compaction). As a result, higher grain comminution and greater porosity and permeability loss are associated with late-stage strike-slip deformation bands, thus forming more effective fluid barriers. This information might contribute to fluid flow properties prediction on siliciclastic reservoirs, where faults are commonly dominated by deformation bands.

3.2 Geological Setting

The Rio do Peixe Basin (RPB) is an intracontinental basin located in northeast Brazil (Fig. 3.1A). The RPB formed as a consequence of the NNW-SSE extension occurred during the opening of the Atlantic Ocean in the Early Cretaceous (e.g., Françolin et al., 1994; Nogueira et al., 2015). During this event, brittle reactivation of the Brasiliano (740 – 560 Ma) E-W-striking Patos and the NE-SW-striking Portalegre ductile shear zones occurred, defining the current basin architecture (Sénant and Popoff, 1991; Françolin et al., 1994). The basin is composed of three asymmetric sub-basins: NE-SW trending Brejo das Freiras (BFSB), E-W trending Sousa (SSB) and NE-SW trending Pombal (PSB; Fig. 3.1B). These sub-basins present elongated shapes following the direction of the main basin-bounding faults, Portalegre (NE-SW), Malta (E-W) and Rio Piranhas (NE-SW) faults, respectively (e.g., Sénant and Popoff, 1991; Françolin et al., 1994; Nogueira et al., 2015). The basin-bounding faults presents a strong relationship with the formation of syn-sedimentary deformation bands and deformation band clusters (e.g., Nicchio et al., 2018; Araujo et al., 2018; Pontes et al., 2019) with higher deformation band frequency on basin-bounding fault damage zone (Silva et al., 2021).

Two tectonic stages occurred in the RPB formation (Nogueira et al., 2015). The syn-rift phase took place in Barriasian to Aptian time (Nóbrega et al., 2005) and caused the foundering of the basin, with a vertical maximum tensile stress ($\sigma1$) and NW-SE oriented minimum compressive stress ($\sigma3$). Such a stress field was responsible for the development of the main NE-SW trending extensional faults. In the same time span, E-W, NW-SE and N-S oriented faults were formed, interpreted as release faults (de Castro et al., 2007). In the post-rift stage, an approximately WSW-ENE main compressive stress ($\sigma1$) generated positive reactivation of former normal faults that overprinted the Patos (E-W) and Portalegre (NE-SW) ductile shear zones, thus revealing the tectonic inversion of

the basin (Vasconcelos et al., 2020). Additionally, the post-rift stage was responsible for the development of E-W and NE-SW strike-slip faults (Nogueira et al., 2015). Although the exact age of the beginning of the post-rift stage is not yet known, the latest post-rift deformation is Quaternary (Nogueira et al., 2015). In this work, the two studied fault zones are located near the Portalegre Fault (Fig. 1B and C), consisting of NE-SW trending synthetic and antithetic normal faults crosscutted by N-S and NW-SE strike-slip faults (Fig. 3.1C).

Intracontinental Early Cretaceous siliciclastic deposits fill the RPB and increase their thickness toward the faulted borders (de Castro et al., 2007). Three units deposited in adjacent depositional environments in the basin are described here. The Antenor Navarro formation is classified as braided fluvial deposit and is composed of medium to coarse grain size arkose and conglomerates (Sénant and Popoff, 1991; Françolin et al., 1994). The Sousa formation is composed of lacustrine shales and siltstones. The Rio Piranhas formation is composed of coarse sandstones and is interpreted as alluvial fan deposits associated with the evolution of the São Gonçalo Fault (Sénant and Popoff, 1991; Françolin et al., 1994). These units cap a pre-rift prodeltaic lagoonal-lacustrine mudstones and medium-to-very fine-grained sandstones and braided fluviodeltaic sandstones and conglomerates, with interbedded mudstones and fine-grained sandstones (Silva et al., 2014).

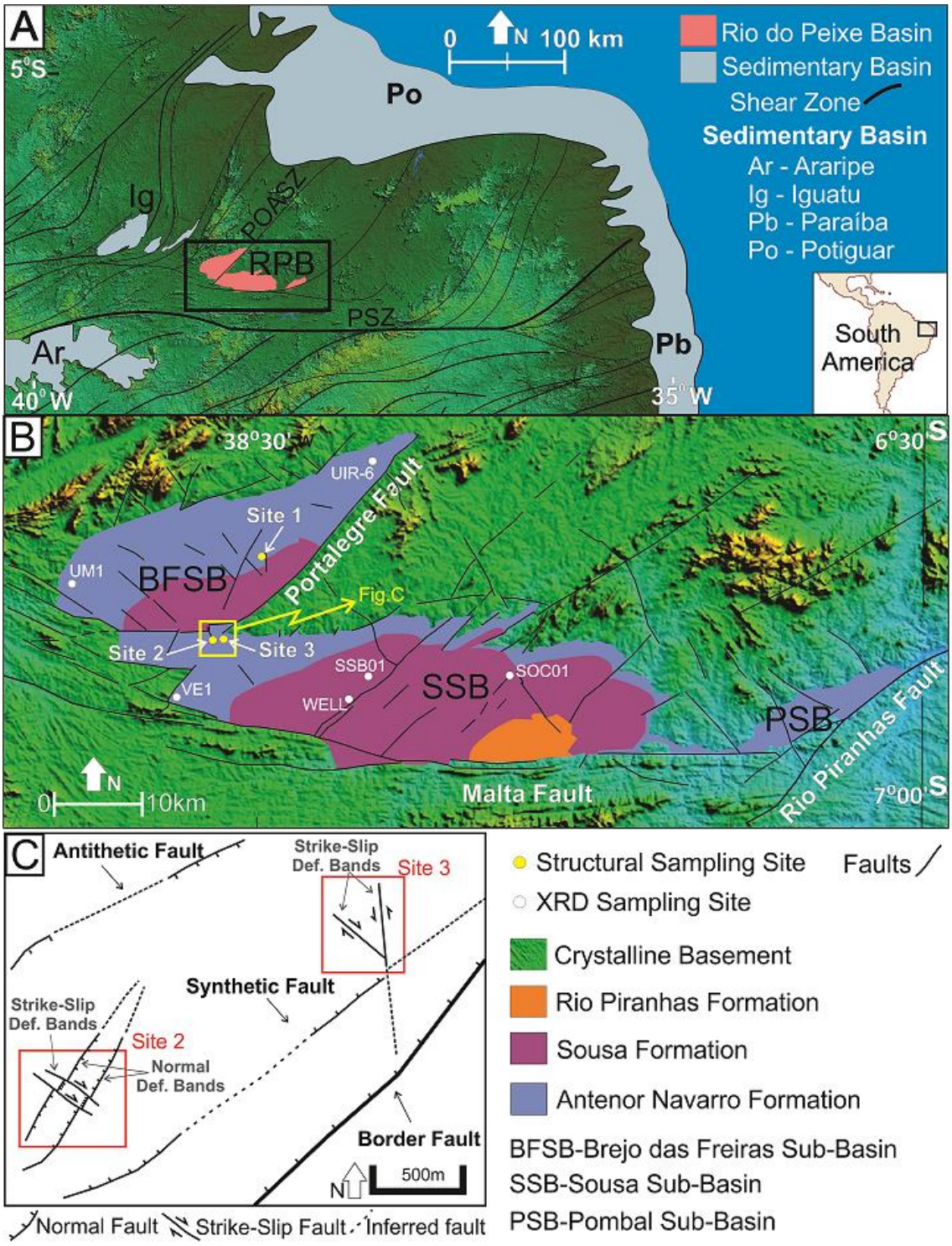

Fig. 3.1. (A) Shuttle Radar Topography Mission (SRTM) image with the Rio do Peixe Basin location and simplified tectonic framework of northeastern Brazil. Ar = Araripe Basin; Ig = Iguatu Basin; Pb = Paraíba Basin; Po = Potiguar Basin; RPB = Rio do Peixe Basin; PSZ = Patos Shear Zone; POASZ = Portalegre Shear Zone. (B) Geological map of the Rio do Peixe Basin showing structural site (yellow dots) and sampling (white dots) locations. Modified from Françolin et al., (1994) and Nogueira et al., (2015). (C) Simplified structural framework of the study area. Red boxes indicate faulted zones cited in the text.

3.3 Methods

This work is based on field, microscopic, mineralogical and petrophysical data. During the field work, we documented the DBs structural data and cross cutting relationships among different sets. We collected 34 samples from the sandy conglomerate facies (of the Antenor Navarro Formation) in three distinct outcrops: site 1 is ~10 km-far away from major bounding Portalegre fault in the BSFB, whereas sites 2 and 3 are near by the sub-basin bounding Portalegre Fault (Fig. 3.1B). Thin section analyses were performed with a standard petrographic microscope (Zeiss Axioplan). We used a Scanning Electronic Microscope (JEOL JSM 6400) with magnifications of 250x and 2.000x for investigation of fine-grained minerals. Thirteen representative samples were investigated for 2D grain size and shape distributions using image analysis from the open software ImageJ 1.51®: non-deformed sandy conglomerate (n=3), tectonically compacted sandy conglomerate (n=1) (i.e., volume of rock between bands presenting no deformation bands), normal DBs (n=4), right-lateral strike-slip DBs (n=3), left-lateral strike-slip DBs (n=2). We measured the survivor grains (i.e., coarser grains surrounded by cataclastic matrix) in the deformation bands. To analyze grain size and aspect ratio of 3723 grains we used 36.5 x 24 mm images with a resolution of 0.155 pixel/mm.

Total porosity and pore size distribution were measured by Hg-intrusion porosimetry using a PoreMaster33 (Quantchrome Instruments) on undeformed rocks (n=3), tectonically compacted host rock (n=2), normal DBs (n=6), right-lateral strike-slip DBs (n=4) and left-lateral strike-slip DBs (n=6). Additionally, we conducted in situ air-permeability measurements using a TinyPermII permeameter (New England Research) on the host rock, tectonically compacted host rock and deformation bands. In the undeformed host rock, we performed five measurements on points of the exposure and on eight points on the tectonically compacted host rock. On deformation bands, we measured 13 normal DBs and 19 strike-slip DBs, in which 12 on right-lateral strike-slip DBs and 7 on left-lateral strike-slip DB. Finally, combining porosimetry and permeability data, we estimated the capillary pressure of host rocks and all sets of deformation bands. As the obtained drainage curves from mercury injection data of deformed samples did not expose clear inflection points (e.g., Torabi et al., 2013), we used the empirical relation of Pittman (1992) to estimate the capillary pressure. The calculation was based on average porosity and average permeability values of host rock, tectonically compacted host rock, normal and strike-slip deformation bands, using the following equation:

Log rapex = 0.123 + 0.37logk (R2 = 0.80)

Pc = 90.018(rapex)-0.99 (R2= 1)

Where, rapex = effective pore-throat radius on apex point on mercury injection curves; k= permeability; and Pc= capillary pressure at the apex point (Torabi et al., 2013).

We performed in situ geomechanical analysis using the L-Type Schmidt Hammer to evaluate the fault-induced compaction in undeformed and faulted sandstone. For that, we applied the standards of the American Society for Testing and Materials (ASTM; Aydin, 2009). For each measured point, we acquired 10 rebound values, i.e. each 10 rebound values correspond to 1 uniaxial compressive strength (UCS) measure. We combined the average rebound values with the average rock density to convert Schmidt hammer measurements into UCS values. To calibrate the obtained UCS values, we compared our results with the compilation of UCS values obtained by Baud et al., (2013) for medium/coarse sandstones. We performed 28 measurements of UCS on host rock, 57 measurements on tectonically compacted host rock, 15 measurements on normal DBs and 52 measurements on strike-slip DBs being 20 on right-lateral DB and 32 on left-lateral DB.

To constrain the burial depth at which deformation occurs, X-ray diffraction (XRD) analysis of the whole-rock and the <2 μm grain size fraction has been carried out on five undeformed samples collected in the field (UM1, UIR6, VE1, SSB01, SOC01 in Fig. 1B) and four samples collected from boreholes at depth 8 m, 100 m, 200 m and 300 m (Well in Figure 1B) with a Scintag X1 X-ray system (CuKα radiation) at 40 kV and 30 mA. Randomly-oriented whole-rock powders were run in the 2-70 °2θ interval with a step size of 0.05°2θ and a counting time of 3 s per step. Oriented air-dried and ethylene-glycol solvated samples were scanned from 1 to 48 °2θ and 1 to 30 °2θ respectively with a step size of 0.05 °2θ and a count time of 4 s per step. The illite content in mixed layers I-S was determined according to Moore and Reynolds (1997) using the delta two-theta method after decomposing the composite peaks between 9-10 °2θ and 16-17 °2θ. The I–S ordering type (Reichweite parameter, Jagodzinski, 1949) was determined by the position of the I001-S001 reflection between 5 and 8.5 °2θ in the ethylene-glycol solvated patterns (Moore and Reynolds 1997). Peaks in relative close position were selected for clay mineral quantitative analysis to minimize the angle-dependent intensity effect. Composite peaks were decomposed using Pearson VII functions and the WINXRD Scintag

associated program. Integrated peak areas were transformed into mineral concentration by using mineral intensity factors as a calibration constant (for a review, see Moore and Reynolds 1997).

3.4 Results

3.4.1 Host rock characterization

The undeformed outcrop (site 1) is located in the central region of the Brejo das Freiras sub-basin, where the Antenor Navarro Formation is exposed (Fig. 3.1B). The formation is composed of a siliciclastic fluvial sequence with cm-to-meter thick conglomerate layers with lenses of medium-to-coarse pebbly sandstones and cross-stratified sandstones (Fig. 3.2A). The conglomerate presents a low degree of compositional maturity as it is mainly composed of quartz (~45%), feldspar (~35%) and rock fragments (20%). (Fig. 3.2C).

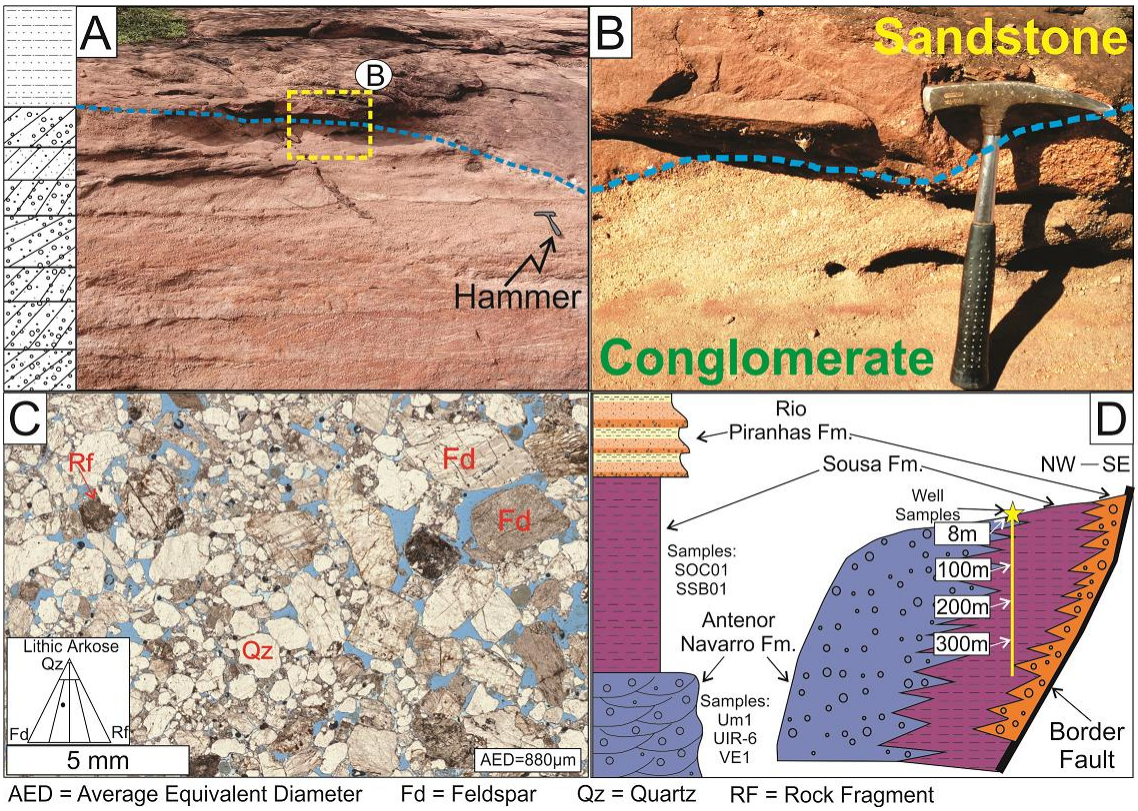

AED = Average Equivalent Diameter Fd = Feldspar Qz = Quartz RF = Rock Fragment

Fig. 3.2. (A) Overview of the undeformed outcrop. (B) Detail of the conglomerate (at the base) in contact with fine-grained sandstone (at the top). (C) Thin section of undeformed conglomerate. Rf= Rock Fragment; Fd= Feldspar; Qz= Quartz. Porosity indicated by blue color. (D) Simplified stratigraphic column with sampling location. Stratigraphic column simplified from Araujo et al. (2018). Stratigraphic chart simplified from Silva et al. (2014).

3.4.1.1 X-ray diffraction (XRD) analysis

XRD analyses were performed on the coarser conglomeratic facies of the Antenor Navarro Formation (Fig. 3.2B and D) and the very fine sandstones of the Sousa Formation (Fig. 3.2D). The undeformed Antenor Navarro Formation is mainly composed of quartz and K-feldspar grains, which constitute at least 85% of the overall composition of the unit and subordinate amounts of phyllosilicate minerals (from 7 to 12%), such as smectite, illite and mixed layer illite-smectite (I-S) and hematite (3-5%; Tab. 3.1 and Fig. 3.3A). The <2 μm grain size fraction is characterized by a smectite-rich composition (>84%) with low illite and random ordered (R0) mixed layers I-S contents (Tab. 3.2; Fig. 3.3D).

Sample ID	Formation	whole-rock composition (%wt)						
		Qz	Kfs	Ab	Phy	Hem	Anl	Cal
VE1	Antenor Navarro	34	51	-	12	3	-	-
UIR6	Antenor Navarro	24	9	55	7	5	-	-
UM1	Sousa	34	37	17	11	1	-	-
SOC01	Sousa	15	16	20	15	5	9	20
SSB01	Sousa	16	14	41	5	2	6	16

Tab. 3.1. Whole-rock composition of undeformed surface samples from the Antenor Navarro and Sousa Formations. Qz-quartz; Kfs-K-feldspar; Ab-albite; Phy-phyllosilicate minerals (smectite, illite, mixed layered minerals, kaolinite); Hem-hematite; Anl-analcime, Cal-calcite.

Surface samples from the Sousa Formation display quartz (15-34%), feldspars (orthoclase, microcline, and albite), phyllosilicate minerals, hematite (1-5%), calcite (16-20%), and analcime (6-9%; Fig. 3.3B). Among phyllosilicates, smectite is the most abundant clay mineral in the <2 μm grain size fraction with contents ranging from 63% to 95%, followed by illite (1-9%) and mixed layer chlorite-smectite (C-S; Tab. 2). K-feldspar occurs in sample SSB01 with amounts not exceeding 1%.

Sample ID	Formation	<2µm grain size fraction (%wt)							
		Sm	I	I-S	C-S	Kln	non-clay minerals	R	%I in I-S
VE1	Antenor Navarro	97	2	1	-	tr	Kfs+Qz	0	10
UIR6	Antenor Navarro	84	11	5	-	-	Ab+Kfs+Qz	0	30
UM1	Sousa	95	1	-	4	-	-	-	-
SOC01	Sousa	89	9	-	2	-	Ab+Anl+Cal+Kfs+Qz	-	-
SSB01	Sousa	63	36	-	-	1	Ab+Anl+Cal+Kfs+Qz	-	-

Tab. 3.2. Semi-quantitative X-ray diffraction analysis of the <2 µm grain-size fractions for the undeformed surface samples from the Antenor Navarro and Sousa formations. Sm-smectite; I-illite; I-S-mixed layer illite-smectite; C-S-mixed layer chlorite-smectite (corrensite); Kln-kaolinite; Qz-quartz; Kfs-K-feldspar; Ab-albite; Anl-analcime; Cal-calcite; tr-traces; R- Reichweite parameter; %I in I-S-illite content in mixed layer illite-smectite.

Subsurface samples are from the Sousa Formation at depths between 8.45 and 300 m collected in the borehole 1-BSB01-PB (Fig. 3.1B for location). Whole-rock samples show a mineralogical association made of K-feldspar (5-9%), albite (28-49%), calcite (9-26%), analcime (1-25%), phyllosilicate minerals (3-10%), with increasing content of quartz as function of depth (from 10% to 19%). Hematite does not exceed 5% (Tab 3).

Sample ID	Formation	whole-rock composition (%wt)						
		Qz	Kfs	Ab	Phy	Hem	Anl	Cal
8.45 m	Sousa	10	6	28	10	4	16	26
100 m	Sousa	16	5	49	3	3	1	23
199.5 m	Sousa	14	7	30	10	5	25	9
300 m	Sousa	19	9	37	5	4	14	12

Tab. 3.3. Whole-rock composition of the very fine sandstones from the 1-BSB01-PB borehole. Qz-quartz; Kfs-K-feldspar; Ab-albite; Phy-phyllosilicate minerals (smectite, illite, mixed layer chlorite-smectite, chlorite); Hem-hematite; Anl-analcime, Cal-calcite.

In the <2 µm grain size fraction, illite is the main clay mineral in all the specimens with contents ranging between 82% and 89%, followed by mixed layer chlorite-smectite (up to 18%) and chlorite (1-5%). Smectite occurs only at the shallowest depth (8.45 m) with contents of 15% (Tab. 3.4).

Sample ID	Formation	<2μm grain size fraction (%wt)				
		Sm	I	C-S	Chl	non-clay minerals
8.45 m	Sousa	15	84	tr	1	Ab+Anl+Cal+Cbz+Kfs+Qz
100 m	Sousa	-	89	6	5	Ab+Cal+Kfs+Hem+Qz
199.5 m	Sousa	-	82	18	tr	Ab+Anl+Cal+Hem+Kfs+Qz
300 m	Sousa	-	82	13	5	Ab+Anl+Cal+Kfs+Qz

Tab. 3.4. Semi-quantitative X-ray diffraction analysis of the <2 μm grain-size fractions for the very fine sandstones drilled in the 1-BSB01-PB borehole. Sm-smectite; I-illite; I-S-mixed layer illite-smectite; C-S-mixed layer chlorite-smectite (corrensite); Chl-chlorite; Qz-quartz; Kfs-K-feldspar; Ab-albite; Anl-analcime; Cal-calcite; Cbz-Chabazite-Na; tr-traces.

The occurrence of the superstructure peak at low diffraction angles (about 3° 2θ) allowed us to identify mixed layer chlorite-smectite as low-charge corrensite with a 50/50 composition and R1 ordering (Fig. 3.3F).

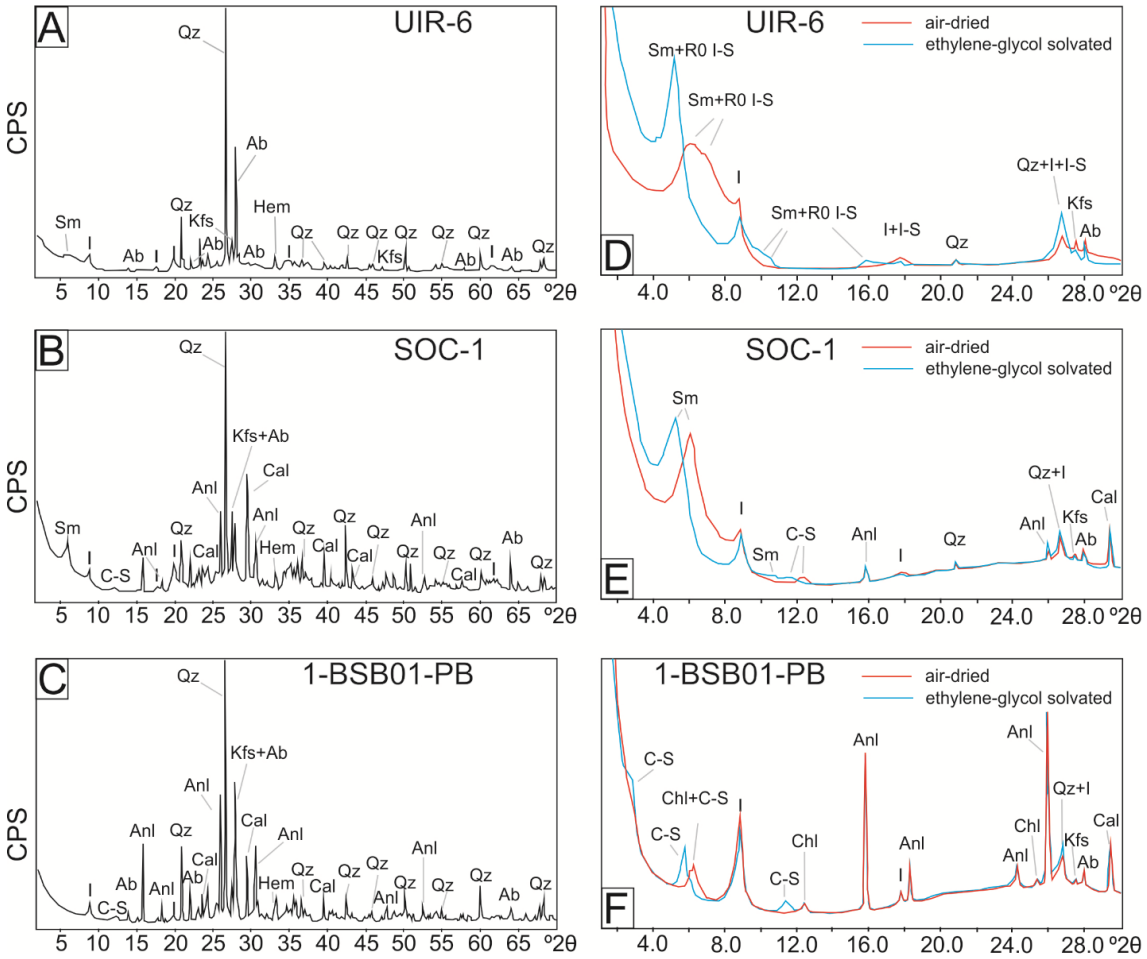

Fig. 3.3. Selected X-ray diffraction patterns for the whole-rock composition (A-C) and <2 µm grain-size fraction (D-F) of surface and subsurface samples from the Antenor Navarro and Sousa Formations. The blue and red lines show ethylene-glycol-solvated and air-dried diffraction patterns of the <2 µm grain-size fraction, respectively. A and D- UIR 6 (Antenor Navarro Fm.); B and E- SOC01 (Sousa Fm.); C and F- subsurface sample at a depth of 300 m from well 1-BSB01-PB (Sousa Fm.). Acronyms: Chl-chlorite; I-illite; I-S-mixed-layer illite-smectite; Sm-smectite; C-S- mixed-layer chlorite-smectite; Ab-albite; Anl-analcime; Hem-hematite; Qz-quartz; Cal-calcite; Kfs-K-feldspar (microcline and orthoclase). R0 refers to mixed layer illite-smectite stacking order.

3.4.1.2 Petrography and SEM analysis of subsurface very fine sandstones (Sousa Formation)

The very fine sandstone presents a tight fabric with gentle grain alignment. Although calcite cement may be present among the fine-grained minerals, it mainly occurs as an infill of shear fractures (Fig. 3.4A and B). Iron oxides occur in the shear veins as mm-long pockets (Fig. 3.4B) and intergranular micro-pore (Fig. 3.4C and D). SEM images allowed the identification of the most abundant minerals of the rock fabric, which is similar on both fine (Fig. 3.4C) and very fine grains (Fig. 3.4D). Based on EDS spectra, we identified albite (Fig. 3.4E), quartz (Fig. 3.4F) and K-feldspar (Fig. 3.4G). Except for

the authigenic iron oxide, all minerals occur as detrital grains with anhedral morphology. Analcime has been detected as anhedral grains but can also replace albite (Fig. 3.4C, D and H).

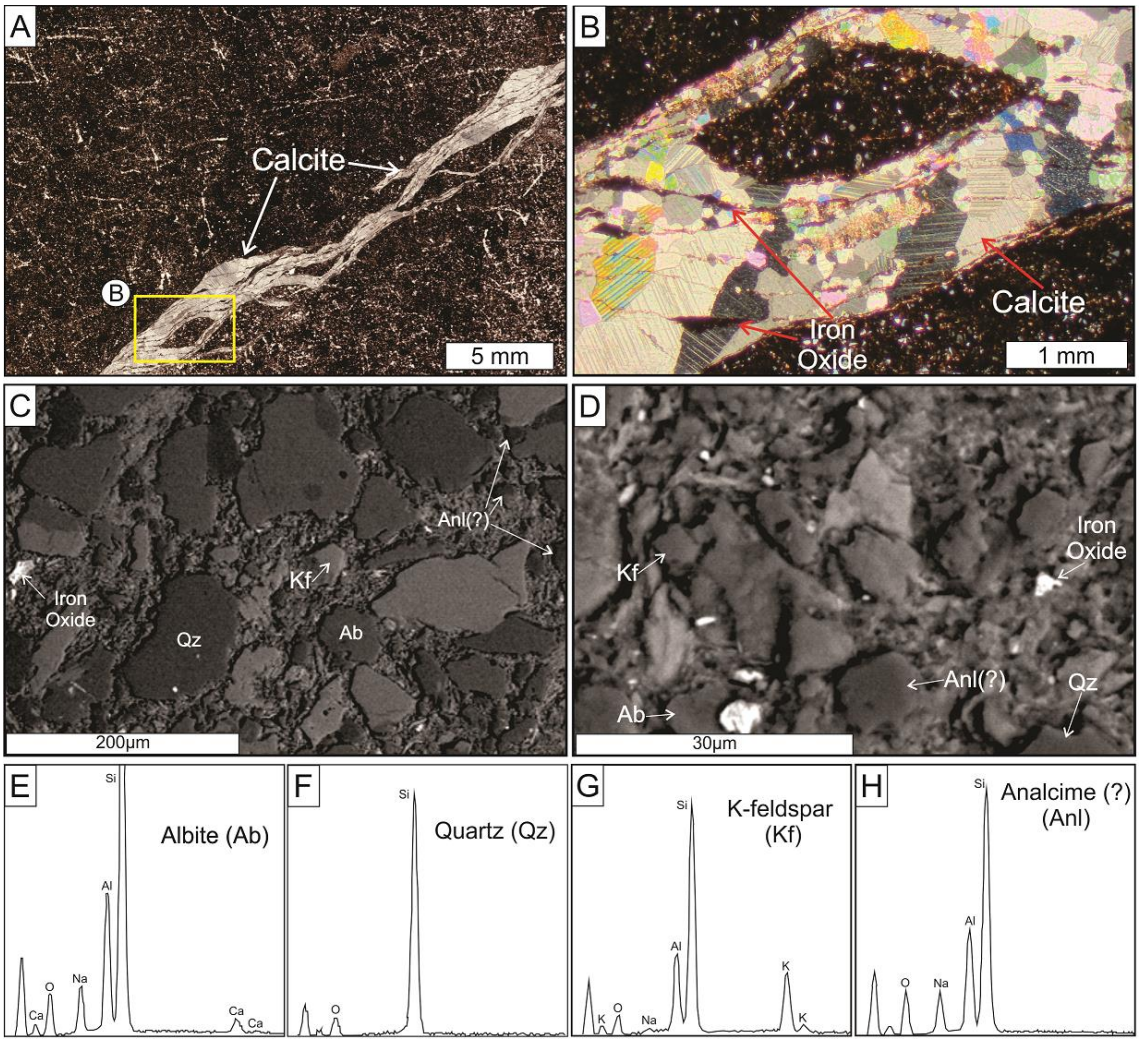

Fig. 3.4. Thin section analysis of very fine sandstone (Sousa Formation). (A) General view of the fine sandstone deformed by shear fracture filled by calcite. (B) Detail of the calcite and iron oxide filling the shear fracture. (C) SEM image of the coarse grains. (D) SEM image of the fine grains. (E to H) EDS spectra of the main constituent minerals. Ab = Albite; Qz = Quartz; Kfs = K-feldspar; Anl = Analcime.

3.4.2 Structural data

The Antenor Navarro Formation at sites 2 and 3 (Fig. 3.1B) is affected by syn-rift normal faults, post-rift strike-slip faults, and related DBs. Both sites are located at the southeastern edge of the Brejo das Freiras sub-basin, near the Portalegre Fault and close to the intersection between the Brejo das Freiras and Sousa sub-basins (Fig. 3.1). Site 2 is part of the major basin-boundary Portalegre fault damage zone (cf. Araujo et al., 2018)

and consists of a 60-m wide deformed zone with conjugate systems of NE-striking normal faults (~2-3 m offset) and related deformation bands. Normal faults and deformation bands are systematically cross-cut in this site by NW striking DBs with right-lateral transtensional shear and locally by NNW striking DBs with left-lateral transtensional shear (Fig. 3.5A). Site 3 is located approximately 1.8 km NE from site 2 (Fig. 3.1). Site 3 shows well-developed ~N-S deformation bands with left-lateral strike-slip kinematics and NW-SE deformation bands with right-lateral strike-slip kinematics (Fig. 3.5B). Left-lateral and right-lateral deformation bands mutually cross-cut each other. As common characteristics of both outcrops, single and deformation band clusters exhibit anastomosed geometry and positive relief. The thickness of individual DBs ranges between a few mm up to 1 cm.

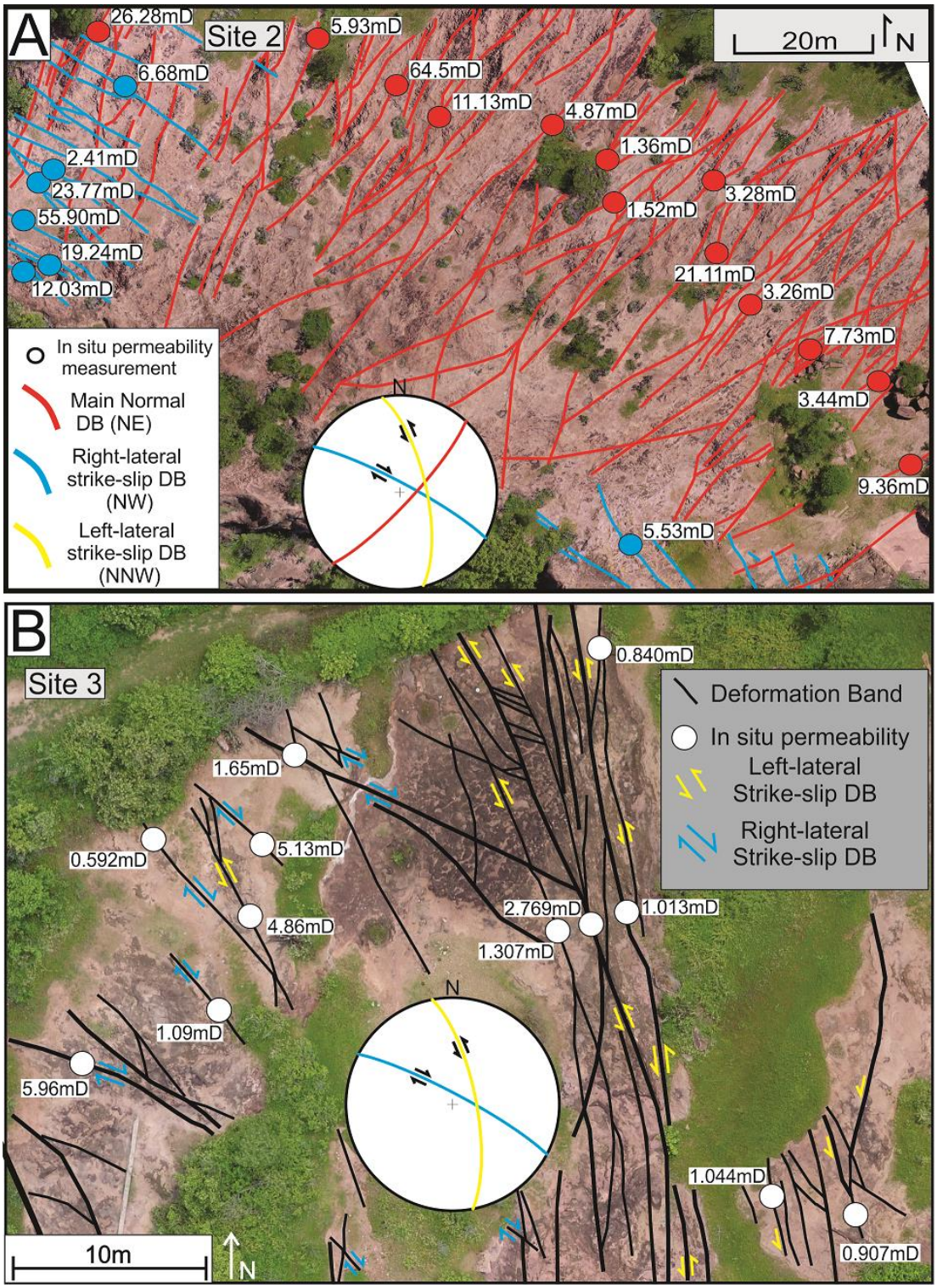

Fig. 3.5. Drone imagery and line drawings of main deformation bands with the location of in situ permeability measurements. (A) NE-striking normal deformation band clusters (average planes plotted in red in the Schmidt projection) and NW-striking right-lateral strike-slip deformation band clusters (average planes indicated by blue lines on the Schmidt projection) in site 2. Permeability values of normal (red dots) and oblique deformation bands (blue dots) are also shown. (B) Main strike-slip deformation bands of site 3 (average planes plotted on the Schmidt projection). Blue lines indicate the right-lateral DBs, and yellow lines indicate the left-lateral DBs. White dots indicate the location of in situ permeability measurements and corresponding permeability values.

3.4.2.1 Normal Deformation Bands

The normal deformation bands associated with NE-striking normal faults form a complex anastomosed pattern clustered within the fault damage zones (Fig. 3.5A and 3.6A). The clusters are up to ~5 m wide (Fig. 3.6A), with several distributed deformation bands spaced apart a few centimeters to decimeters (Fig. 3.6A). The displacement of individual deformation bands can reach ~1-10 cm, locally with striae indicating dip-slip kinematics (Fig. 3.6B and D). When the deformation band cross-cuts contact zones between conglomerate and sandstone, sand intrusion, clast injection within the sandstone and sediment mixing between conglomerate and sandstone occur (Fig. 3.6C).

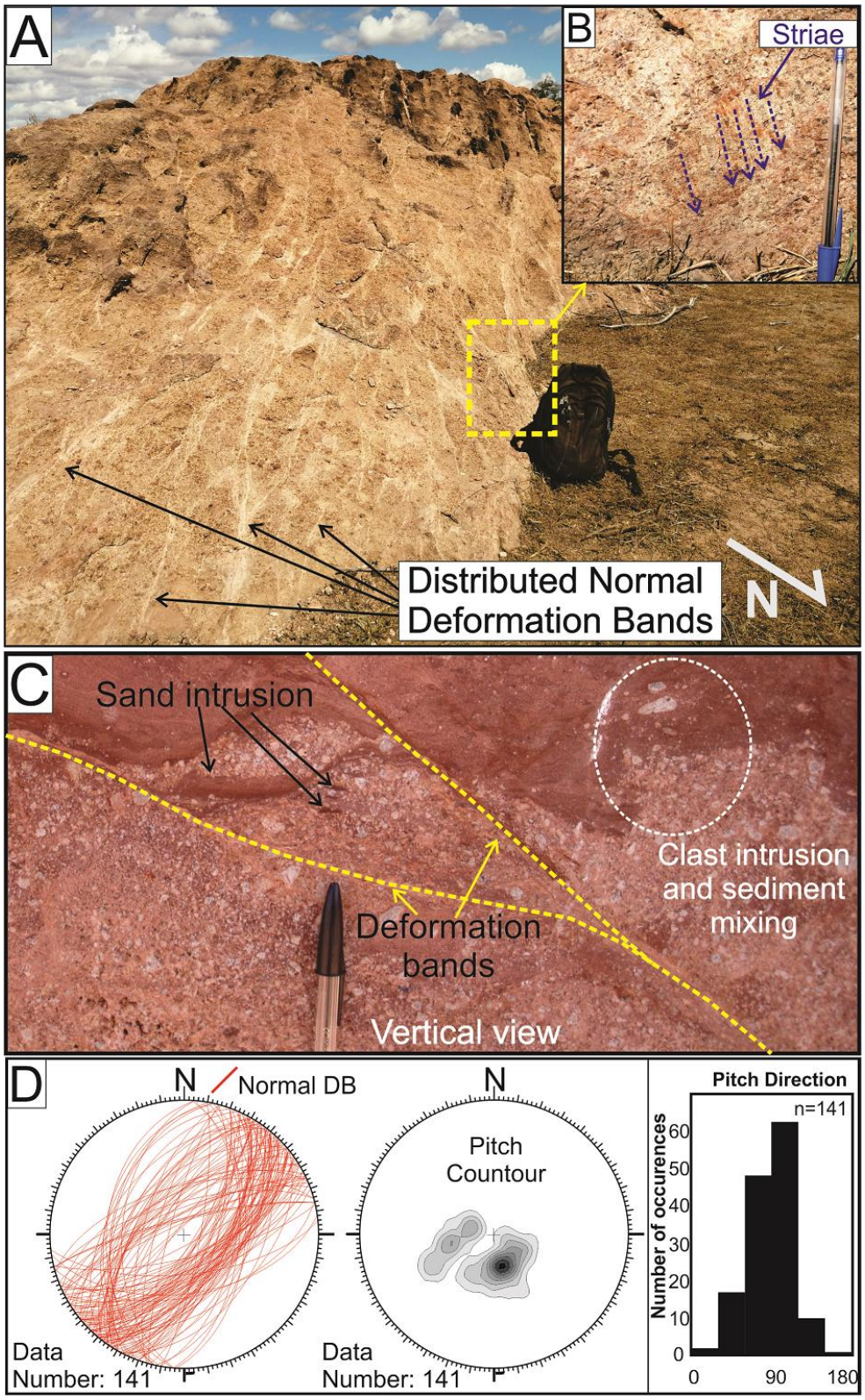

Fig. 3.6. Outcrop view of NE-striking normal deformation bands. (A) DB cluster with a detailed view of the NE-striking deformation band clustering zone. (B) Exposed deformation band plane with striae indicating dip-slip kinematics. (C) Detail of a polished vertical wall exhibiting normal deformation band cross-cutting facies contact zone. Note the sand intrusion and sediment mixing occurring between deformation bands. (D) Lower hemisphere Schmidt projection of deformation band (left), contour stereonet of the measured pitch (center), and histogram of pitch direction (right).

3.4.2.2 Strike-slip Deformation Bands

Two sets of strike-slip deformation bands occur in sites 2 and 3 (Fig. 3.7 and 3.8). In site 2, a NW-striking set of deformation bands with oblique to right-lateral kinematics form mostly subparallel, cm-thick clusters (Fig. 3.7A). In the same site, few NNW-striking left-lateral deformation bands are present but in lower frequency. The NW-striking bands with right-lateral transtensional movement cross-cut the NE-trending normal deformation bands (Fig. 3.7B and C). The striae commonly present high obliquity on exposed shear planes with pitch values between 30 and 150° (Fig. 3.7D). When observed, the apparent displacement can reach up to ~15-20 cm.

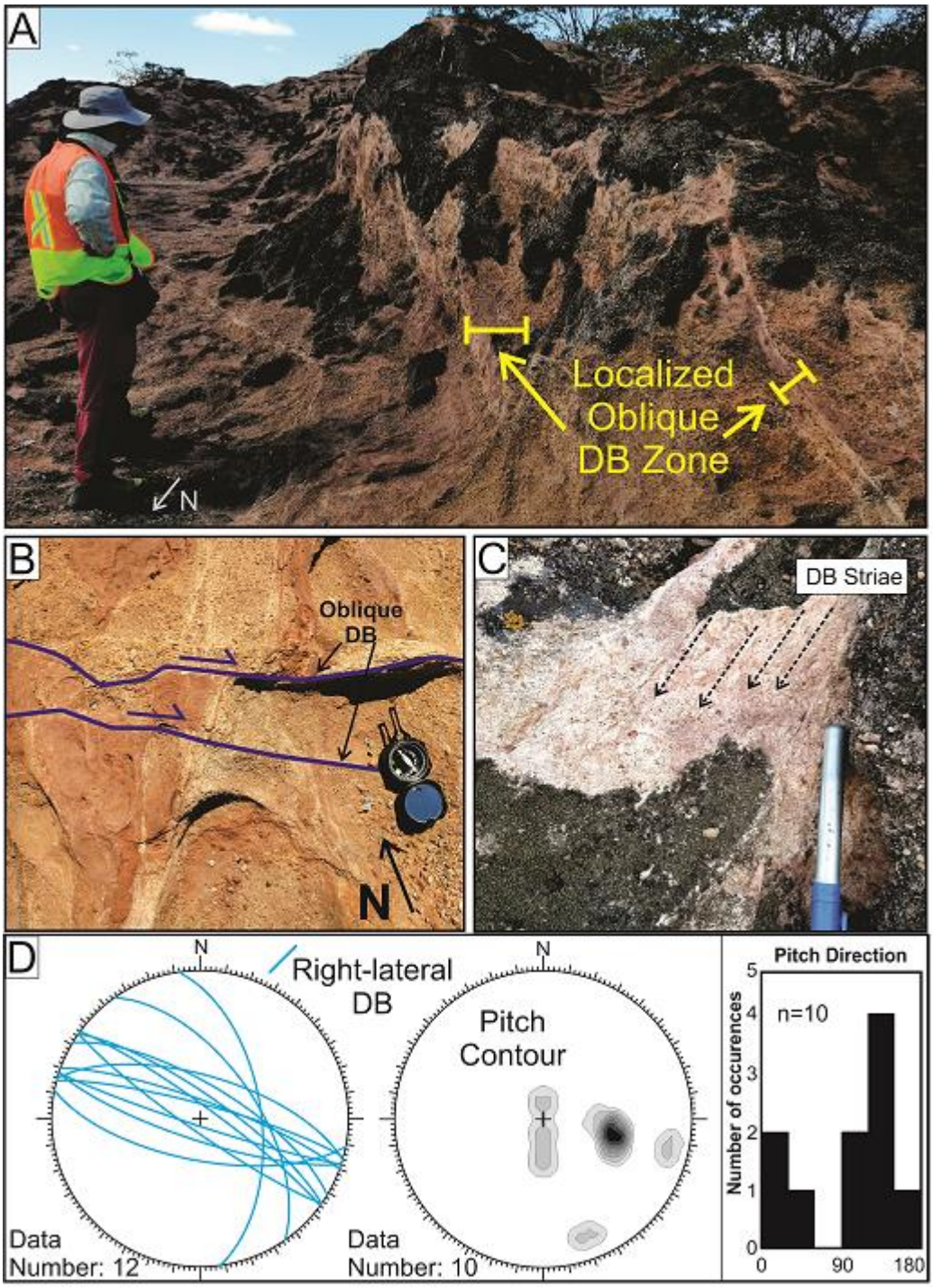

Fig. 3.7. Outcrop details of the NW-trending right-lateral strike-slip deformation bands clusters in site 02. (A) Deformation band clusters formed by several right-lateral oblique deformation bands. (B) Plane view of right-lateral NW-striking deformation bands crosscutting NE-striking deformation bands. (C) Detail of DB striae indicating right-lateral transtensional kinematics. (D) Schmidt projection of deformation band (left), stereonet contour of the pitch (center), and histogram of pitch direction (right).

In site 3 (Fig. 3.2B and 3.8), two different sets of deformation bands with strike-slip kinematics occur and mutually crosscut each other. The main set is NNW-SSE oriented with a left-lateral sense of shear (Fig. 3.8A and B). This most prominent set

forms a major m-thick deformation band clusters (Fig. 3.8A). The NW-SE strike-slip set occurs as well developed subparallel deformation bands with a right-lateral sense of shear (Fig. 3.8C), as observed in site 2. The NNW-SSE set forms several subparallel left-lateral dm-thick deformation band clusters. For both deformation band sets, displacement of individual bands can reach up to ~15cm (Fig. 3.8B and C). The bands are subvertical and, when visible, show a predominance of horizontal striae (Fig. 3.8D). The bands are localized within the clusters, with isolated occurrences away from the clusters.

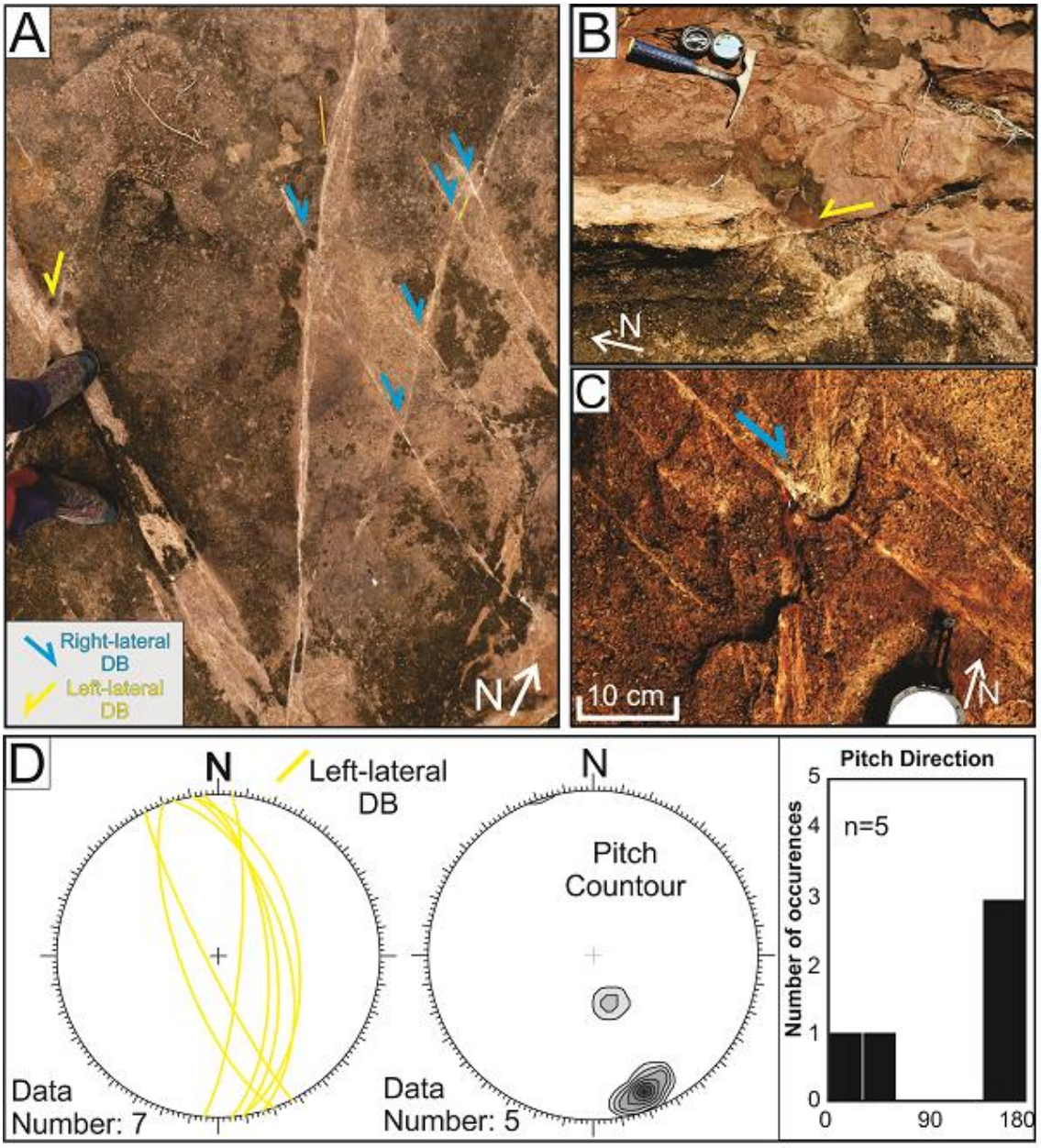

Fig. 3.8. (A) Outcrop view of the strike-slip deformation band system in site 03. Yellow arrows indicate left-lateral displacement. Blue arrows indicate right-lateral displacement. (B) Detail of NNW-SSE left-lateral deformation band. (C) Detail of NW-SE right-lateral deformation band. (D) Schmidt projection of the measured left-lateral deformation bands

(left) (right-lateral deformation bands are illustrated in Fig. 3.7D), contour stereonet of the measured pitch (center), and histogram of pitch direction (right).

3.4.3 Microstructural observations

Undeformed sandstone and conglomerate in site 1 show a grain size spanning from ~0.1 mm up to 6 mm in diameter. The host rock is generally grain supported without any significant clay matrix. The grains are subspherical to elongate. In faulted sites, sandstone between DBs have similar grain sizes but show a tighter fabric than observed in the host rock of site 1 (compare Fig. 3.9A with Fig. 3.2C). The normal deformation bands display significant grain size reduction (Fig. 3.9B) with diffuse boundaries between DBs and host sandstone. The strike-slip deformation bands show very intense grain size reduction (Fig. 3.9C and D) and commonly develop a cataclastic foliation marked by the alignment of intensely comminuted grains (Fig. 3.9C). Locally, thin slip zones (<1 mm thick) of ultra-comminuted grains and very high cataclastic matrix content occur within the strike-slip deformation bands (Fig. 3.9D). Conversely to the normal deformation bands, the deformation band borders are straight, and the sandstone outside the deformation bands has a tight fabric.

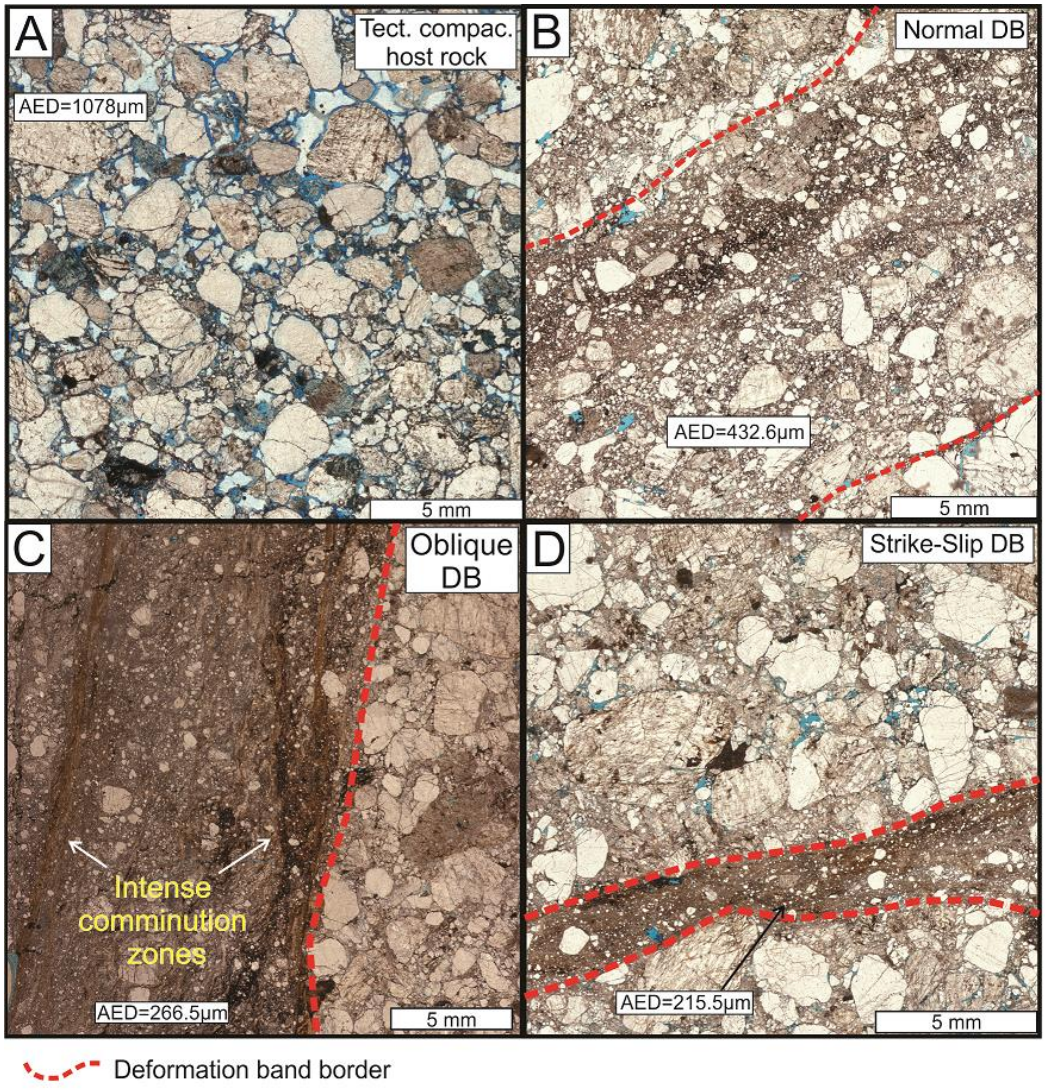

Fig. 3.9. Microscopic view of the tectonically compacted host rock (A) (Site 2), normal deformation band (B) (Site 2), foliated strike-slip deformation band surrounded by intensely compacted host rock (C) (Site 2), and thin strike-slip deformation band surrounded by moderately compacted host rock (D) (Site 3). Kfs= K-feldspar; Qz= quartz and Rf= rock fragments. Deformation bands are delimited by red dashed lines. AED = Average Equivalent Diameter measured in undeformed samples and within deformation bands. Intergranular pores are indicated by blue epoxy resin.

3.4.4 Grain size and shape analysis

The average equivalent diameter of the host rock grains is 880 ±518 µm, where quartz and feldspar have averaged values of 764 ± 416 µm and 1052 ± 600 µm, respectively (Fig. 3.10A). In tectonically compacted host rocks, the average equivalent diameter for all grains is 744µm ± 587 and quartz and feldspar grains have values of 587 ± 347 µm and 979 ± 767 µm, respectively. In deformation band samples, a strong grain size reduction occurs. The average equivalent diameter for total grains, quartz and feldspar in

deformation bands, are respectively: normal deformation bands, 432.6µm ± 300, 403µm ± 284.67 and 479µm ± 318.75; right-lateral strike-slip deformation bands, 266.5µm ± 183.68, 250µm ± 145.63 and 312µm ± 258.76; and left-lateral strike-slip deformation bands, 215.5 µm ± 144.74, 209µm ± 139.19 and 229µm ± 154.59 (Fig. 3.10A).

The average aspect ratio (standard deviations in brackets) on host rock grains is 1.57 ± 0.42 on total grains, 1.48 ± 0.32 on quartz and 1.70 ± 0.51 on feldspar grains (Fig. 3.10B). On tectonically compacted host rocks, the calculated average aspect ratio for all grains is about 1.57 ± 0.38; individually, on quartz and feldspar grains, the average values are 1.49 ± 0.35 and 1.69 ± 0.39, respectively. On deformation bands, the average aspect ratio on total grains, quartz and feldspar grains, were respectively: on normal deformation bands: 1.55 ± 0.42, 1.57 ± 0.46 and 1.51 ± 0.35; on right-lateral strike-slip deformation bands: 1.49 ± 0.37, 1.48 ± 0.36 and 1.51 ± 0.41; and on left-lateral strike-slip deformation band: 1.44 ± 0.32, 1.44 ± 0.32 and 1.43 ± 0.32 (Fig. 3.10B).

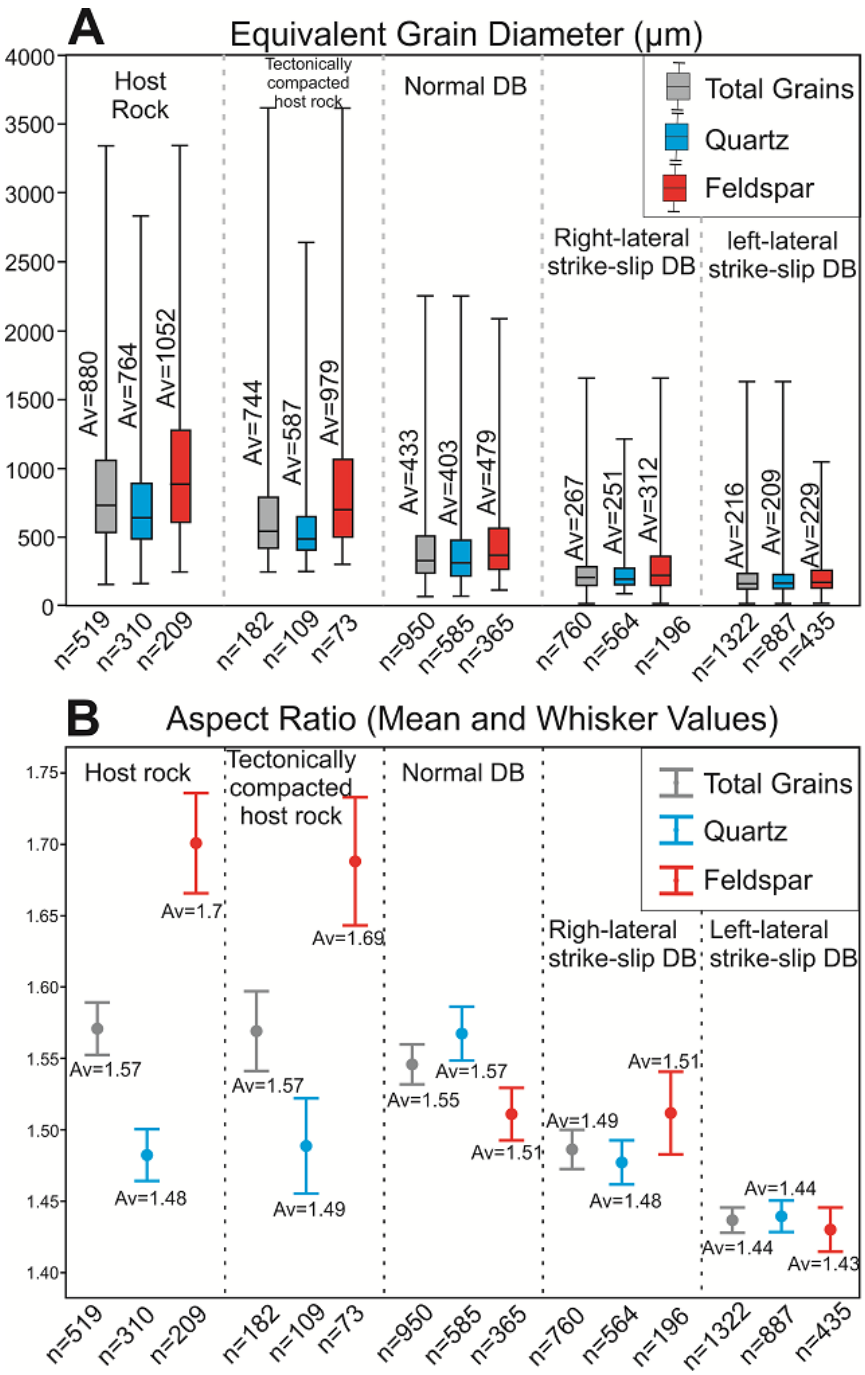

Fig. 3.10. Grain size and shape data of host rock and deformation bands. (A) Boxplot showing equivalent grain diameter in µm. (B) Mean and Whisker Values graphic of Aspect Ratio. Data for host rocks are gray, quartz grains are blue, and feldspar grains are red. n = number of measured grains.

3.4.5 Petrophysical data

3.4.5.1 Porosity

The undeformed rocks show a bimodal pore size distribution with a predominance of pore diameter between 10^{-1} and 10^{-2}µm and secondary pore size frequency between 10^{-1} and 100 µm (Fig. 3.11). The average total porosity value is 25.32% (Fig. 3.12A), and the

average pore size is 14.97μm (Fig. 3.12B). A similar pore size distribution is observed in the tectonically compacted host rock, with a predominance of pore diameter between 101 and 102 and a secondary pore size frequency between 10-1 and 100 μm. The average total porosity is about19.5% (Fig. 3.12A), and the average pore size is 19.7 μm (Fig. 3.12B). The pore-size distribution in deformation bands is mostly unimodal to quasi-unimodal, with a predominance of pore size values between 101 and 10-2 μm (Fig. 3.11). Porosity and pore size reduction occur in deformation bands (Fig. 3.11 and 3.12). In particular, the average porosity is 10% (Fig. 3.12A) and average pore size distribution is 0.38μm in normal deformation bands (Fig. 3.12B). The strike-slip deformation bands display average porosity of 12.71% (Fig. 3.12A) and average pore size distribution of 0.24μm (Fig. 3.12B). Among the strike-slip DBs, the right-lateral strike-slip deformation bands have an average porosity of 12.3% (Fig. 3.12A) and average pore size distribution of 0.14μm (Fig. 3.12B). In contrast, the left-lateral strike-slip DBs have an average porosity of 13.17% (Fig. 3.12A) and average pore size distribution of 0.30 μm (Fig. 3.12B).

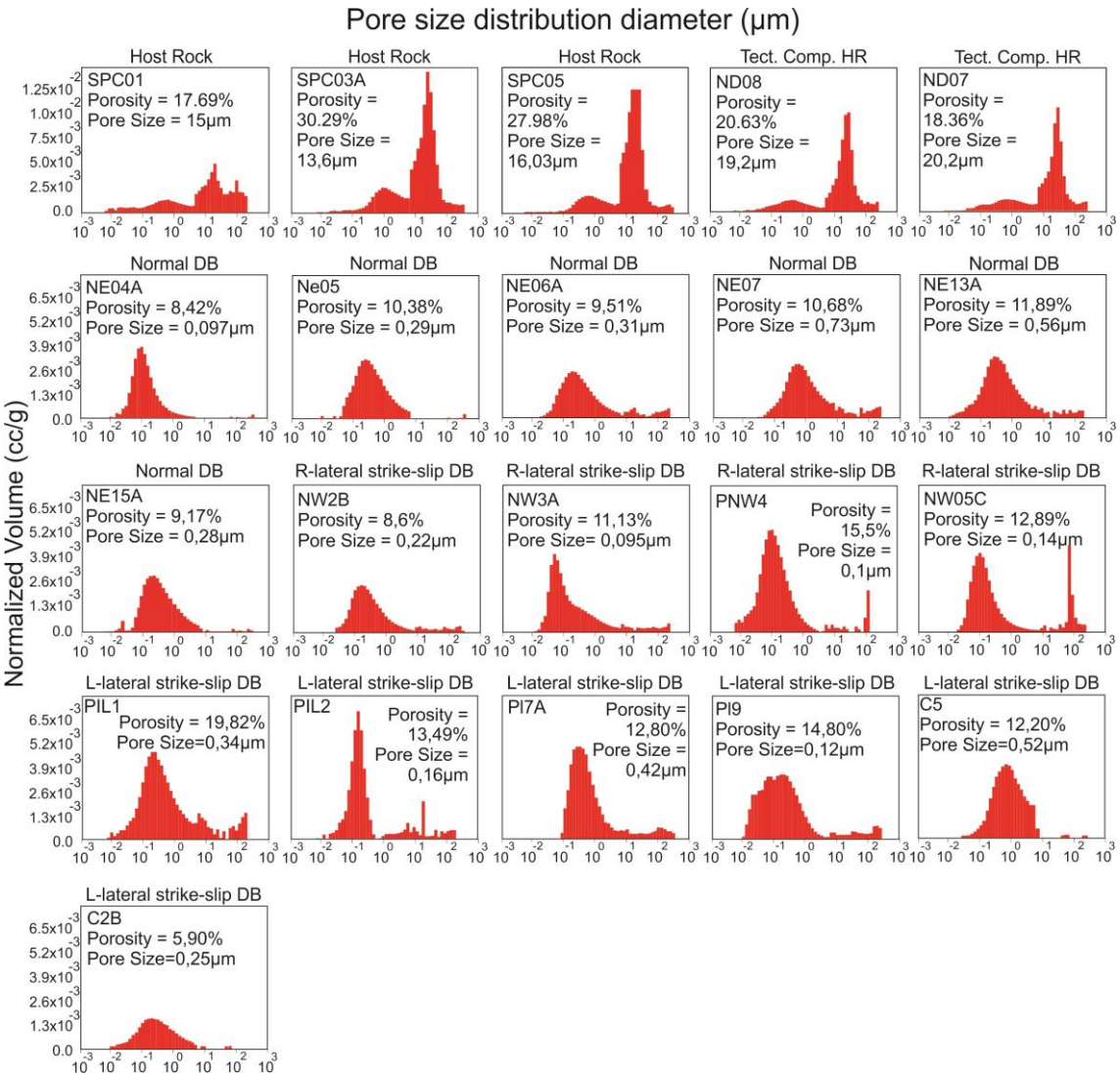

Fig. 3.11. Pore size distribution of undeformed and tectonically compacted host rocks and deformation bands.

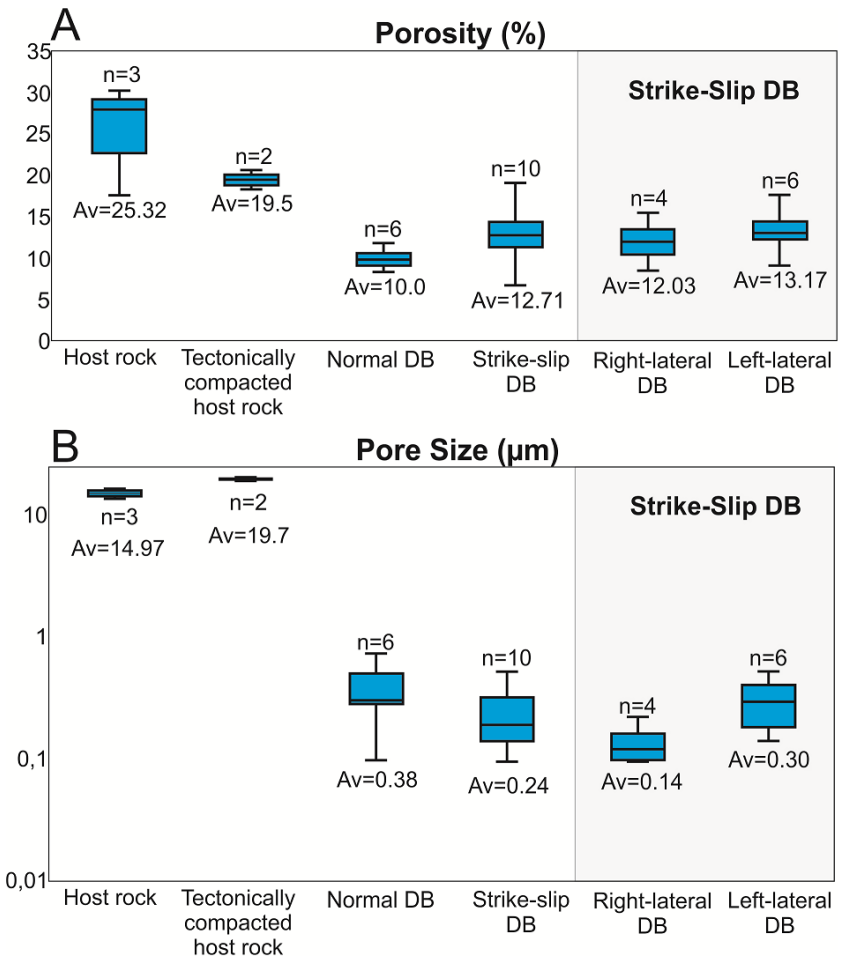

Fig. 3.12. Porosity and pore size distribution analysis. (A) Average total porosity for the analyzed structural domains. (B) Average pore size. Av= Average value.

3.4.5.2 Permeability

In situ air permeability data on deformation bands show low values for all faulting regimes concerning undeformed rocks (Fig. 3.13). On the host rock, the average permeability value is about 1308.42 mD. On tectonically compacted host rock, the average permeability is about 769.13mD. In contrast, for the normal DB, the average is about 12.60 mD, and for the strike-slip DB, the average is about 8.04 mD. Among the strike-slip DB, the right-lateral shear sense bands display an average permeability value of about 11.67 mD, whereas the left-lateral DB are characterized by lower average values, about 1.82 mD.

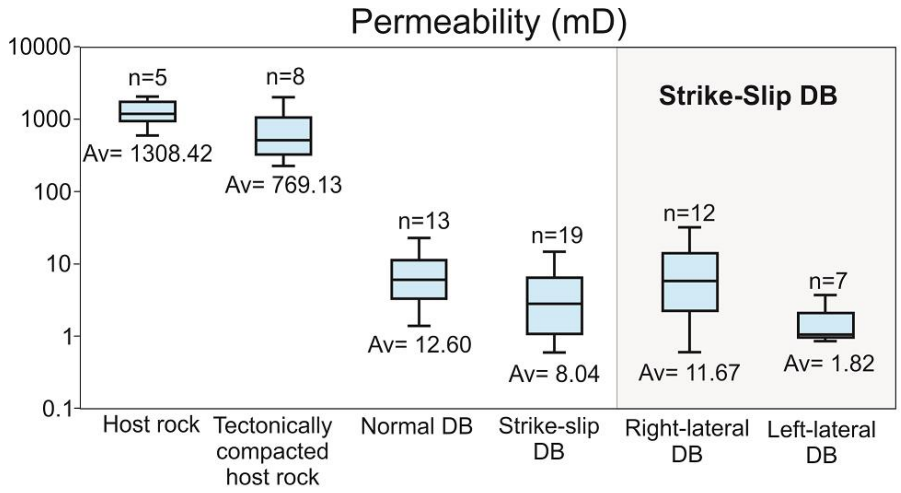

Fig. 3.13. In situ air permeability of undeformed rock and deformation bands. Av= Average value. N= number of measured locations on undeformed conglomerate and number of measured fault planes.

3.4.5.3 Capillary Pressure

Based on the empirical relations by Pittman (1992), the calculated pore size on the apex of the host rock is 16.77μm, while for the tectonically compacted host rock is 13.77 μm. In the deformed samples, the calculated pore size on the apex is intensely reduced (Table 3.5). The calculated pore size on apex point in normal DB is 2.03 μm, whereas in right-lateral and left-lateral strike-slip DBs, the calculated pore size on the apex is 1.92 μm and 0.79 μm, respectively. The capillary pressure data show significant differences between host rock and deformed samples (Fig. 3.14A). The host rock and tectonically compacted host rock samples present similar drainage curves, with single inflection points and low variation of capillary pressure. The calculated average capillary pressure for the host rock samples is 4.91 psi, while the tectonically compacted host rock yield 5.96 psi (Fig. 3.14B). The drainage curves indicate that the capillary pressure of deformation bands are significantly higher than those of undeformed and tectonically compacted host rocks. The DB samples curves do not show a clear threshold pressure point, and some samples, mainly strike-slip DBs, apparently present more than one inflection point (Fig. 3.14A). The calculated capillary pressures are 26.88 psi for normal DB, 27.65 psi for right-lateral and 54.61 psi for left-lateral strike-slip deformation bands (Tab. 3.5).

Domain	Average Porosity (%)	Average Permeability (mD)	Calculated Pore Size on Apex (µm)	Calculated Capillary Pressure (Psi)	Uniaxial Compressive Strength (Mpa)
Host Rock	25.32	1308.42	18.89	4.91	22.85
Tec. Comp. host rock	19.5	769.13	15.52	5.96	52.12
Normal DB	10.00	12.6	3.39	26.88	43.77
Right-lateral DB	12.71	11.67	3.29	27.65	49.85
Left-lateral DB	13.17	1.82	1.66	54.61	51.48

Tab. 3.5. Calculated pore size on apex point and capillary pressure of host rock and fault samples. The pore size on the apex was calculated based on average porosity and permeability data. The capillary pressure was calculated based on the pore size on the apex of each domain.

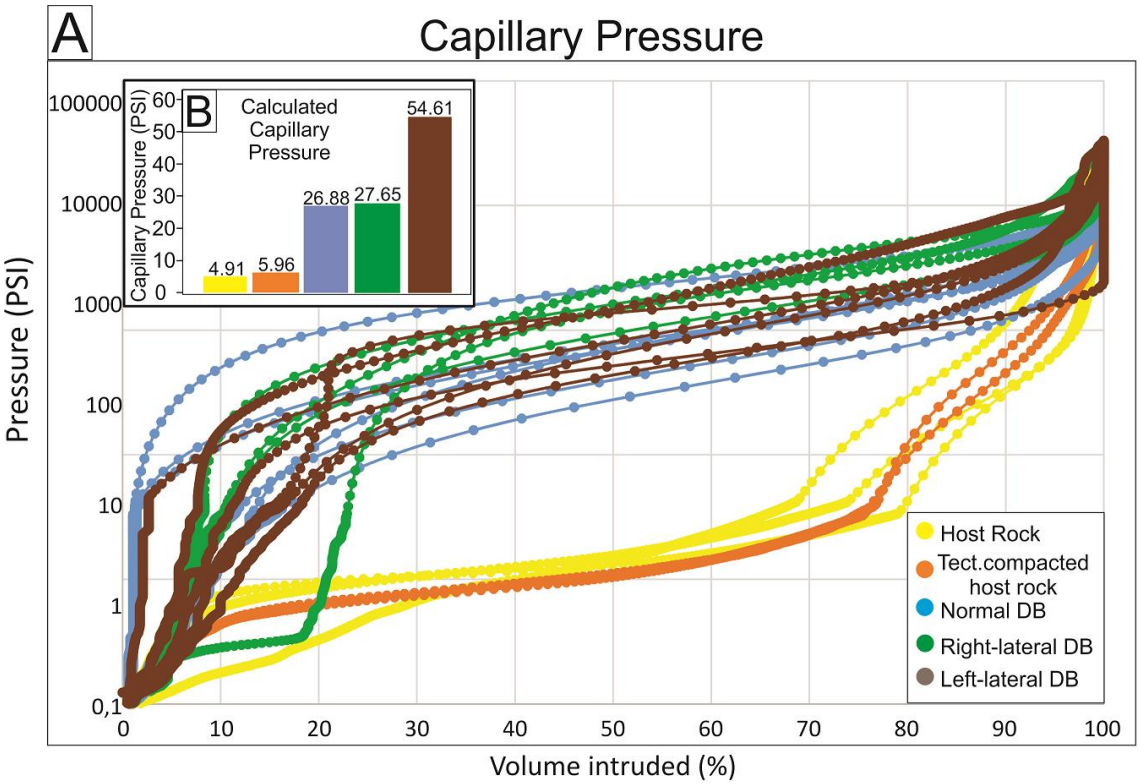

Fig. 3.14. (A) Semi-log diagram showing mercury injection drainage curves of host rocks and deformation bands. (B) Calculated average capillary pressure of each domain.

3.4.5.4 UCS data

The measured values of UCS are shown in Fig. 3.15 and table 3.5. For the host rock, the UCS values vary from 14.25 MPa to 36.94 MPa, with an average value of 22.85 MPa. The tectonically compacted host rocks display the highest average values, with UCS values varying from 43MPa to 79.1 MPa and an average value of 52.12 MPa. In the

normal deformation band zone, the values range from 34.50 MPa to 56.00 MPa, with an average value of 43.77 MPa. Compiling the data acquired on strike-slip DB, the values vary from 35MPa to 83.5 MPa with an average of 49.85MPa. Among the strike-slip DB, the right-lateral DB zone shows values between 37 MPa and 59 MPa, with an average value of 47.25 MPa. The UCS values obtained on the left-lateral strike-slip deformation band zone range from 35 MPa to 83.5 MPa, with 51.48 MPa as average.

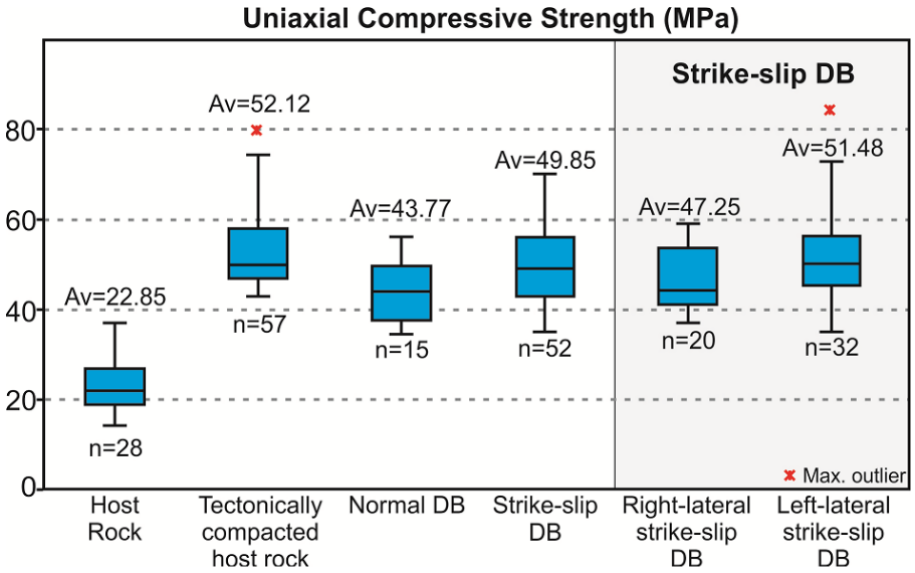

Fig. 3.15 Calculated UCS values for undeformed rocks and deformation bands. The values are expressed in MPa. Av= Average values. n= Number of sampled points.

3.5 Discussion

3.5.1 Burial depth of deformation from mineral assemblages in host rocks

In faulted porous sandstone, burial depth controls the deformation intensity and, in turn, porosity and permeability properties of deformation bands (Ballas et al., 2015; Fossen et al., 2017; Pizzati et al., 2020). In particular, clay mineral assemblage, mixed layered clay minerals and their transformation sequence di-smectite-random ordered mixed layers I-S (R0)-short and long-range ordered mixed layers I-S (R1 and R3)-illite-muscovite can be used as a proxy of maximum burial conditions (e.g., Hower et al., 1976; Pollastro, 1990; Aldega et al., 2017; 2018; 2021) and to determine the depth at which deformation occurred (Meneghini et al., 2012; Carminati et al., 2013;2016). In addition, clay minerals can be a proxy of the degree of fluid-rock interaction in hydrothermal and geothermal systems (e.g., Cox and Browne, 1998; Rossetti et al., 2011; Corrado et al., 2014; Maffucci et al., 2016).

X-ray diffraction analysis of clay minerals from undeformed host rocks (Sousa and Antenor Navarro formations) evidenced a smectite-rich assemblage (Tab. 3.2 and 3.4), indicating formation under near-surface conditions at low temperature. This inference is strengthened by the occurrence of random ordered (R0) I-S with high expandability in the Antenor Navarro Formation (Fig. 3.3), typical of rocks with low levels of thermal maturity formed at shallow depths during burial diagenesis (<1-2km; Srodon, 1999). The inferred shallow burial depths attained for the host rocks are also consistent with the following features: (i) the overall poor lithification of sandstone out of fault zones influence (e.g., site 1 in Figure 1), confirmed by the low UCS values (ii) the microtexture of the host rocks, which display a high porosity framework and the absence of quartz overgrowth (Fig. 3.9A), and (iii) the high permeability (0.7 Darcy, Fig. 3.13) and high Hg-intrusion porosity (17-27%, Fig. 3.11) of undeformed sandstone. In addition, the clay mineral assemblage of the Antenor Navarro Formation is similar to that observed by Maciel et al. (2018), who interpreted the occurrence of smectite as the result of partial weathering of feldspar grains during early diagenesis at shallow depths.

The occurrence of mixed layer chlorite-smectite and the progressive disappearance of smectite in the subsurface samples affected by brittle deformation structures indicate that the Sousa Formation interacted with high temperature geothermal/hydrothermal fluids. In fact, in the active hydrothermal subaerial and submarine systems, the first appearance of mixed layers chlorite-smectite was reported between 150 and 200 °C, and its presence was noted up to temperatures of approximately 300 °C (Schiffman and Fridleifsson, 1991; Shau and Peacor, 1992). This interpretation is strengthened by the presence of analcime in the pores of siltstones and calcite veins (Fig. 3.4A and B), which occur in the Sousa Formation near minor faults and intrabasinal regional-scale faults (Maciel 2020). It indicates that high-temperature geothermal/hydrothermal fluids overprinted the low-temperature mineral assemblage formed during shallow burial conditions. Therefore, we suggest that both normal and strike-slip deformation bands developed under similar burial depths <1-2 km and were affected by hydrothermal fluid ingress.

3.5.2 Relative chronology and development of deformation bands

Figure 3.16 shows a schematic evolution of faults and deformation bands in the Rio do Peixe basin (e.g., Vasconcelos et al., 2020, and references therein). The conjugate systems of normal faults and related deformation bands (site 2, Fig. 3.1) are the earliest deformational features developed in the Portalegre fault damage zone, during the syn-rift stage characterized by a vertical σ1 and horizontal, NNW-SSE-oriented σ3 (Fig. 3.16A; e.g., Araujo et al., 2018). The syn-rift faults exhibit soft-sediment deformation at shallow confining pressure (i.e., burial depth), such as (i) the syn-sedimentary nature of normal faults (Sénant and Popoff, 1991; Araujo et al., 2018); (ii) the distributed deformation in fault core (sensu Rutter, 1986; Balsamo et al., 2010b) without extensive shear localization (Maciel et al., 2018), and (iii) sand intrusion and sediment mixing observed along minor faults and deformation bands (Alsop et al., 2019).

Conversely, the oblique to strike-slip deformation bands documented in this study (sites 2 and 3) have both right- and left-lateral kinematics and systematically cross cut the normal deformation bands (Figs. 3.5A and 3.7B). The strike-slip deformation bands form a conjugate system with a vertical σ2. A NW-SE-oriented horizontal maximum compressive stress directed along the line bisects the acute conjugate angle of strike-slip DBs. Therefore, we suggest they formed during a horizontal NW-SE-oriented compression in the post-rift phase (Fig. 3.16B). The clay mineral assemblages discussed in the previous section formed at similar shallow burial conditions of earlier normal faults (<1-2 km). Therefore, we concluded that these bands also form at similar burial depth.

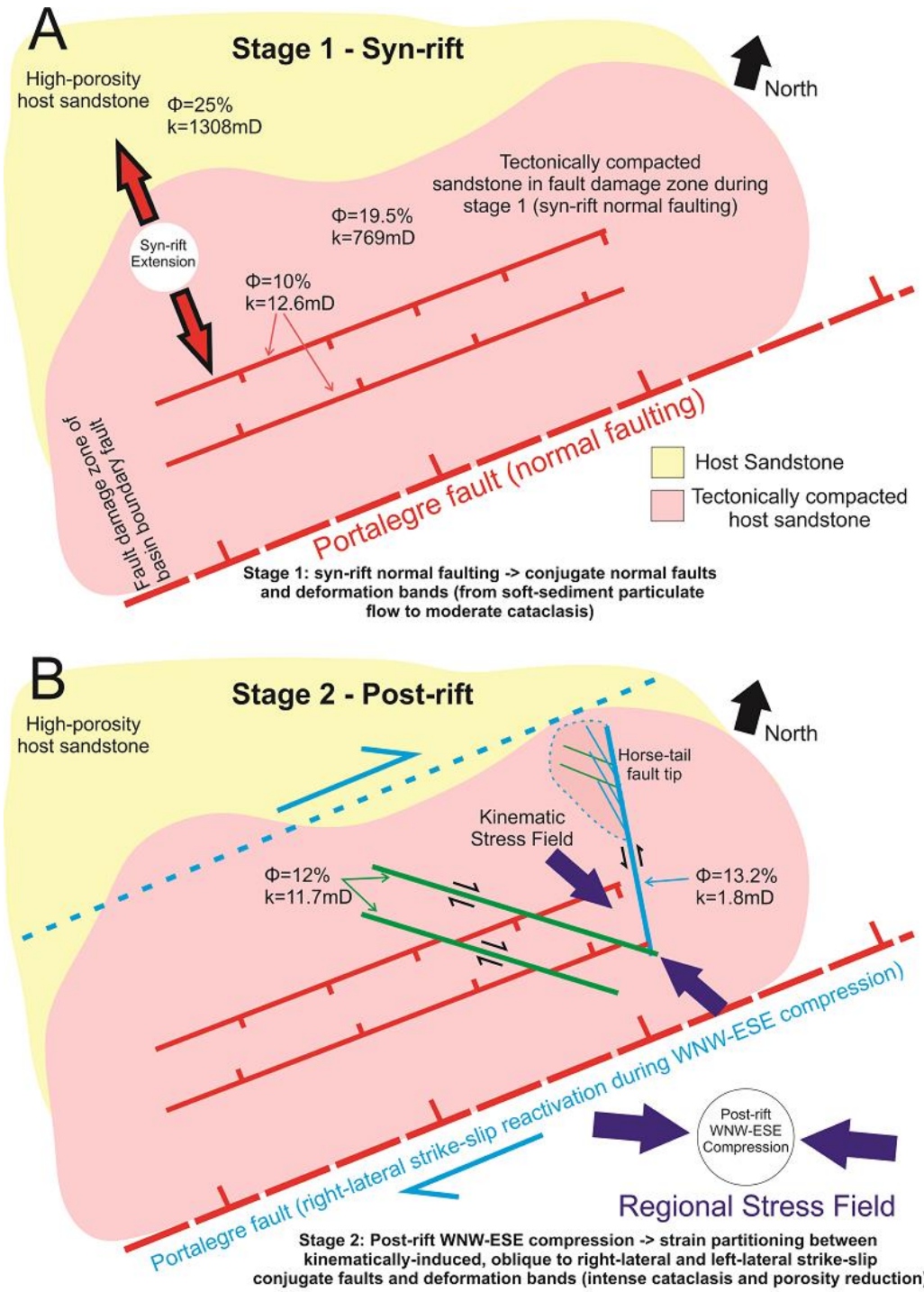

Fig. 3.16. Evolutionary model (not to scale) of faulting during (A) the NW-SE syn-rift extension and (B) WNW-ESE post-rift transpressive reactivation of the Portalegre basin boundary fault. Φ= porosity. K= permeability.

As stated by previous works (Nogueira et al., 2015; Vasconcelos et al., 2020), the post-rift phase consists of a regional ~E-W compression, resulting in a strike-slip transpressive reactivation of the Portalegre basin-boundary fault. The geometrical and kinematic constraints of deformation bands suggest that during the post-rift ~E-W

regional compression, the N70°E-striking Portalegre fault reactivated in right-lateral strike-slip kinematics (Fig. 3.16B). This reactivation triggered a NW-SE-oriented compression within the Portalegre basin boundary fault zone, which in turn was responsible for the formation of ~N-S left-lateral and ~NW-SE right-lateral strike-slip faults and deformation bands. Therefore, we suggest that the conjugate system of strike-slip deformation bands resulted from the post-rift basin inversion that are well documented in the Rio do Peixe basin (Vasconcelos et al., 2020). This is in partial contrast with the model proposed by de Castro et al. (2007), which interpreted "fault-orthogonal" structures as release faults (Destro, 1995) developed during normal faulting. However, (i) the lack of clear structural architecture of release faults in the field, (ii) the systematic cross-cutting relationship between the two normal and right-lateral strike-slip fault systems, and (iii) the different microtextural and petrophysical properties of normal and strike-slip deformation bands (next section), lead us to propose an alternative interpretation different from that proposed by de Castro et al. (2007).

3.5.3 Strain intensity and petrophysics of syn- and post-rift deformation bands

All the deformation bands described in this work developed at shallow burial depths (<1-2 km), presenting moderate to intense cataclasis and locally showing strain localization within narrow slip zones (cf. Nicchio et al., 2018, Nogueira et al., 2021). The microstructural data indicate a greater deformation intensity on strike-slip deformation bands than that observed in the normal deformation bands (Fig. 3.9). As shown in Fig. 3.10, grain size reduction is more intense in left-lateral strike-slip deformation bands, followed by the right-lateral strike-slip bands. Grain shape tends to follow the same trend, i.e., the more reduction in the grain size due to deformation, the more equant the grain aspect ratio becomes (Heilbronner and Keulen, 2006; Storti et al., 2007). Although the porosity reduction is slightly more accentuated in normal deformation bands (Fig. 3.12A), the permeability and pore size reductions in strike-slip deformation bands are more intense, which means that pores are no longer connected, thus suggesting a greater strain in the latter deformation bands in comparison with the former. This greater strain is confirmed by greater compaction inferred from UCS data (Fig. 3.15), which contributed to the higher sealing capacity of strike-slip deformation bands, as showed by the higher capillary pressure compared with other normal DBs and host rock. Recently, Torabi et al. (2021) measured the along-strike variability of capillary pressure porosity and permeability in a DBs cluster associated with a normal fault zone (offset < 10 m)

developed in the high porosity sandstones of the Rio do Peixe basin. Our data from normal deformation bands (26.88 psi) are similar to values described by Torabi et al. (2021), between 30 and 50 psi, whereas higher capillary pressures were found in more intensely deformed post-rift deformation bands with left-lateral strike-slip kinematics.

One possible factor that may explain the difference in petrophysical properties between syn- and post-rift DBs is the displacement accommodated by each deformation band. Displacement accumulation tends to progressively reduce the grain size, porosity and permeability even in low displacement DBs (Balsamo and Storti, 2010; Pizzati et al., 2020). However, the studied syn- and post-rift deformation bands show similar displacement values between 1 and 10 cm, thus ruling out such structural control on observed petrophysical properties.

3.5.4 The role of fault-induced tectonic compaction

Several authors have shown that the depth of deformation (Sperrevik et al., 2002; Beke et al., 2019), shear displacement (Pizzati et al., 2020), slip rate (Cashman et al., 2007; Balsamo et al., 2014), and the tectonic regime (Soliva et al., 2016) influence the deformation band network and properties. In our study, such structural elements do not seem to be the primary factors affecting the formation of deformation bands. As indicated by the crosscutting relationships observed in the field, the post-rift strike-slip systems of DBs developed in a tectonically compacted "host rock" consisting of anastomosed deformation bands (porosity 10%) clustered within normal faults, and tight sandstone between deformation bands (diffuse bulk strain leading to porosity 20%) (Fig. 3.16B). Therefore, the greater strain and capillary pressures in post-rift strike-slip deformation bands can be related to the presence of pre-existing syn-rift deformation bands, which may increase the mechanical resistance of the host rock, resulting in the accumulation of strain as new faults are formed (Gajst et al., 2018). The fault-induced compaction imparted by syn-rift normal faulting may tighten the fabric within the basin-boundary fault and therefore dictate the strain intensity of subsequent deformation bands.

The evolutionary model in Figure 3.17 summarizes our observations and interpretations, in which the progressive syn-rift fault-induced compaction overcomes the effect of increasing confining pressure (burial depth). In an initial stage, the host rock cohesion was low due to high porosity of 25-30% (Fig. 3.17A), allowing the formation of soft-sediment deformation during the syn-rift normal deformation bands with lower

cataclasis intensity (Fig. 3.17B). The normal faulting and deformation bands formation within the Portalegre fault zone resulted in tectonically induced compaction of the host rock, thus decreasing intergranular porosity and increasing the rock mechanical resistance. During the fault inversion in the post-rift stage, the more compacted sandstone formed more localized strike-slip deformation bands as thinner clusters with very intense cataclasis degree (Fig. 3.17C). Locally, strike-slip deformation bands are thinner than normal DBs and have the higher destructive behavior with very intense grain size reduction, permeability of 0.1 mD, and capillary pressure > 100 psi (Fig. 3.16D), thus significantly impacting fluid flow.

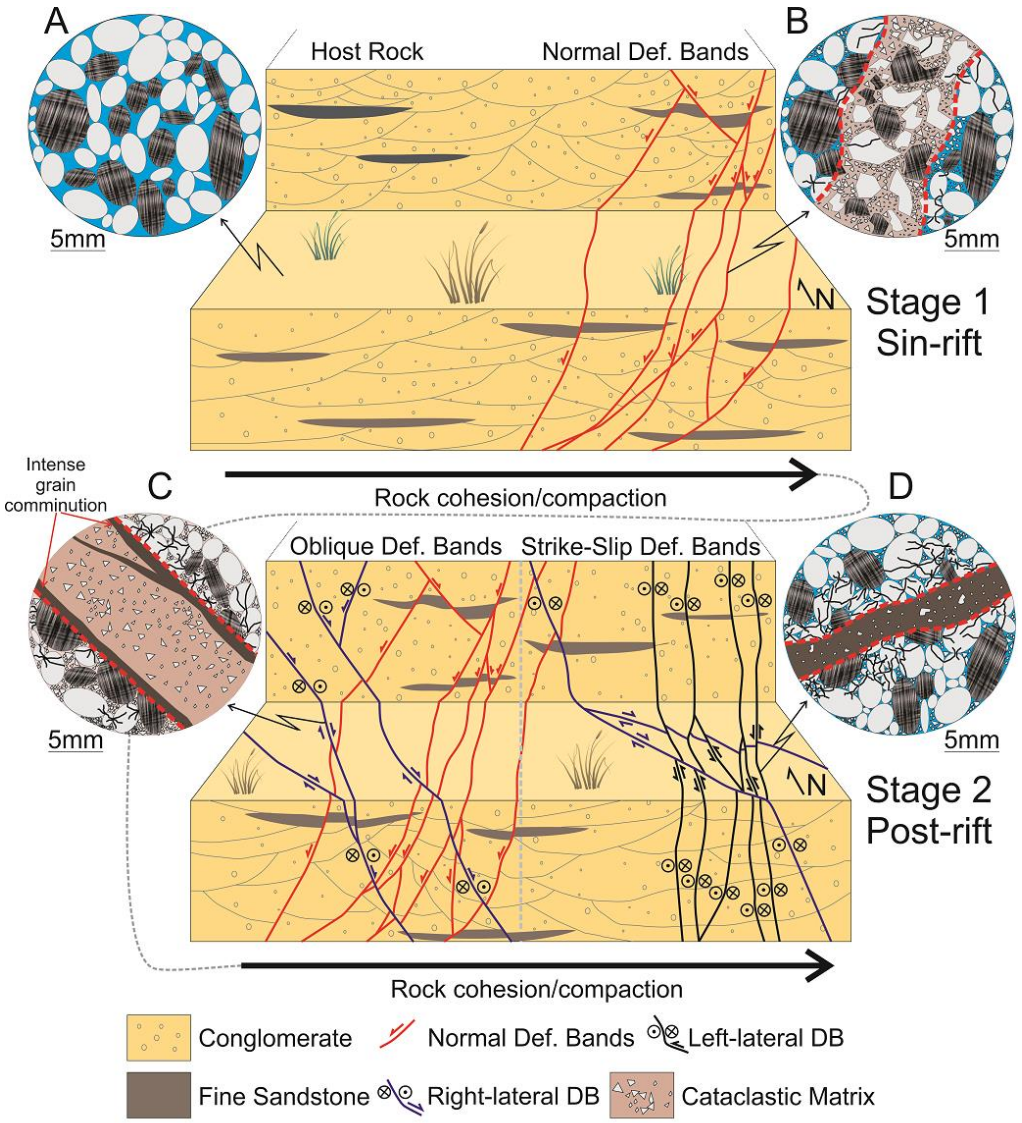

Fig. 3.17. Evolutionary model of deformation bands on Rio do Peixe Basin. A- Undeformed host rock with pristine sedimentary features. Porosity in blue. B- Initial deformation marked by the development of normal deformation bands. Note cataclasis mostly within the band with partial porosity preservation on its borders. C- Second

deformation event marked by strike-slip deformation bands crosscutting the normal deformation bands. Note the very intense cataclasis within the band with strong concentration of intensely comminuted grain on deformation band borders. Out of the band, the porosity is almost completely filled by cataclastic matrix. D- Left-lateral and right-lateral strike-slip deformation bands formed on later deformational stage mutually crosscutting each other. Note the very intense cataclasis degree within the thinner deformation band. Outside the band, the porosity is partially preserved among compacted and fractured grains.

3.6 Conclusions

This work combined structural, microstructural, mineralogical, and petrophysical data of deformation bands formed in damage zones of normal and oblique to strike-slip faults. Based on the observations of this work, we conclude that:

Two distinct faults systems and sets of deformation bands developed within the basin-boundary Portalegre fault zone: NE-SW trending normal faults in a conjugate array, and a conjugate system of oblique to strike-slip faults and deformation bands. All faults and related deformation bands were formed at burial depths not exceeding 1-2 km.

Early syn-rift normal faults were the first to be formed, in soft sediment conditions. During the post-rift stage and fault transpressive reactivation, minor oblique and strike-slip faults developed within the basin-boundary fault zone in a more cohesive, tectonically compacted "host" rock.

The progressive fault strengthening acquired during normal faulting and the reactivation of basin boundary faults are important factors to predict the petrophysical and microstructural properties of deformation bands network in sandstone reservoirs.

Acknowledgments

We are greatful to the Brazilian Oil Company Petrobras that funded the DEBRIP Project (TC 5850.0109438.18.9) coordinated by Francisco C. C. Nogueira (UFCG).

References

Aldega, L., Corrado, S., Carminati, E., Shaban, A., Sherkati, S., 2014. Thermal evolution of the Kuh-e-Asmari and Sim anticlines in the Zagros fold-and-thrust belt: Implications for hydrocarbon generation. Marine and Petroleum Geology 57, 1–13.

https://doi.org/10.1016/j.marpetgeo.2014.04.017

Alsop, G.I., Weinberger, R., Marco, S., Levi, T., 2019. Identifying soft-sediment deformation in rocks. Journal of Structural Geology 125, 248–255. https://doi.org/10.1016/j.jsg.2017.09.001

Antonellini, M.A., Aydin, A., Pollard, D.D., 1994. Microstructure of deformation bands in porous sandstones at Arches National Park, Utah. Journal of Structural Geology 16, 941–959. https://doi.org/10.1016/0191-8141(94)90077-9

Araujo, Renata E B, Bezerra, F.H.R., Nogueira, F.C.C., Balsamo, F., 2018. Basement control on fault formation and deformation band damage zone evolution in the Rio do Peixe Basin , Brazil Tectonophysics Basement control on fault formation and deformation band damage zone evolution in the Rio do Peixe Basin , Brazil. Tectonophysics 745, 117–131. https://doi.org/10.1016/j.tecto.2018.08.011

Araujo, Renata E.B., Bezerra, F.H.R., Nogueira, F.C.C., Balsamo, F., Carvalho, B.R.B.M., Souza, J.A.B., Sanglard, J.C.D., de Castro, D.L., Melo, A.C.C., 2018. Basement control on fault formation and deformation band damage zone evolution in the Rio do Peixe Basin, Brazil. Tectonophysics 745, 117–131. https://doi.org/10.1016/j.tecto.2018.08.011

Aydin, A., 2009. ISRM Suggested method for determination of the Schmidt hammer rebound hardness: Revised version. International Journal of Rock Mechanics and Mining Sciences 46, 627–634. https://doi.org/10.1016/j.ijrmms.2008.01.020

Aydin, A., 1978. Small faults formed as deformation bands in sandstone. Pure and Applied Geophysics PAGEOPH 116, 913–930. https://doi.org/10.1007/BF00876546

Ballas, G., Fossen, H., Soliva, R., 2015. Factors controlling permeability of cataclastic deformation bands and faults in porous sandstone reservoirs. Journal of Structural Geology 76, 1–21. https://doi.org/10.1016/j.jsg.2015.03.013

Ballas, G., Soliva, R., Benedicto, A., Sizun, J.P., 2014. Control of tectonic setting and large-scale faults on the basin-scale distribution of deformation bands in porous sandstone (Provence, France). Marine and Petroleum Geology 55, 142–159. https://doi.org/10.1016/j.marpetgeo.2013.12.020

Ballas, G., Soliva, R., Sizun, J.P., Benedicto, A., Cavailhes, T., Raynaud, S., 2012. The importance of the degree of cataclasis in shear bands for fluid flow in porous sandstone Provence, France. AAPG Bulletin 96, 2167–2186. https://doi.org/10.1306/04051211097

Balsamo, Fabrizio, Clemenzi, L., Storti, F., Solum, J., Taberner, C., 2019. Tectonic control on vein attributes and deformation intensity in fault damage zones affecting Natih platform carbonates, Jabal Qusaybah, North Oman. Journal of Structural Geology 122, 1–20.

Balsamo, F., Aldega, L., De Paola, N., Faoro, I., Storti, F., 2014. The signature and mechanics of earthquake ruptures along shallow creeping faults in poorly lithified sediments. Geology 42, 435–438. https://doi.org/10.1130/G35272.1

Balsamo, F., Storti, F., 2011. Size-dependent comminution, Tectonic mixing, and sealing behavior of a "structurally oversimplified" fault zone in poorly lithified sands: Evidence for a coseismic rupture? Bulletin of the Geological Society of America 123, 601–619. https://doi.org/10.1130/B30099.1

Balsamo, F., Storti, F., 2010. Grain size and permeability evolution of soft-sediment extensional sub-seismic and seismic fault zones in high-porosity sediments from the Crotone basin, southern Apennines, Italy. Marine and Petroleum Geology 27, 822–837. https://doi.org/10.1016/j.marpetgeo.2009.10.016

Balsamo, F., Storti, F., Salvini, F., Silva, A.T., Lima, C.C., 2010a. Structural and petrophysical evolution of extensional fault zones in low-porosity, poorly lithified sandstones of the Barreiras Formation, NE Brazil. Journal of Structural Geology 32, 1806–1826. https://doi.org/10.1016/j.jsg.2009.10.010

Balsamo, F., Storti, F., Salvini, F., Silva, A.T., Lima, C.C., 2010b. Structural and petrophysical evolution of extensional fault zones in low-porosity, poorly lithified sandstones of the Barreiras Formation, NE Brazil. Journal of Structural Geology 32, 1806–1826. https://doi.org/10.1016/j.jsg.2009.10.010

Baud, P., Wong, T., Zhu, W., 2013. International Journal of Rock Mechanics & Mining Sciences Effects of porosity and crack density on the compressive strength of rocks. International Journal of Rock Mechanics and Mining Sciences 67, 10. https://doi.org/10.1016/j.ijrmms.2013.08.031

Beke, B., Fodor, L., Millar, L., Petrik, A., 2019. Deformation band formation as a function of progressive burial: Depth calibration and mechanism change in the Pannonian Basin (Hungary). Marine and Petroleum Geology 105, 1–16.

Bigi, S., Carminati, E., Aldega, L., Trippetta, F., Kavoosi, M.A., 2018. Zagros fold and thrust belt in the Fars province (Iran) I: Control of thickness/rheology of sediments and pre-thrusting tectonics on structural style and shortening. Marine and Petroleum Geology 91, 211–224. https://doi.org/10.1016/j.marpetgeo.2018.01.005

Caine, J.S., Evans, J.P., Forster, C.B., 1996. Fault zone architecture and permeability structure. Geology 24, 1025–1028.

Carminati, E., Aldega, L., Bigi, S., Corrado, S., D'Ambrogi, C., Mohammadi, P., Shaban, A., Sherkati, S., 2013. Control of Cambrian evaporites on fracturing in fault-related anticlines in the Zagros fold-and-thrust belt. International Journal of Earth Sciences 102, 1237–1255. https://doi.org/10.1007/s00531-012-0858-0

Carminati, E., Aldega, L., Bigi, S., Minelli, G., Shaban, A., 2016. Not so simple "simply-folded Zagros": The role of pre-collisional extensional faulting, salt tectonics and multi-stage thrusting in the Sarvestan transfer zone (Fars, Iran). Tectonophysics 671, 235–248. https://doi.org/10.1016/j.tecto.2016.01.033

Cashman, S.M., Baldwin, J.N., Cashman, K. V., Swanson, K., Crawford, R., 2007. Microstructures developed by coseismic and aseismic faulting in near-surface sediments, San Andres fault, California. Geology 35, 611–614. https://doi.org/10.1130/G23545A.1

Cox, M.E., Browne, P., 1998. Hydrothermal alteration mineralogy as an indicator of hydrology at the Ngawha geothermal field, New Zealand. Geothermics 27, 259–270. https://doi.org/10.1016/S0375-6505(97)10015-3

Da Nóbrega, M.A., Sá, J.M., Bezerra, F.H.R., Hadler Neto, J.C., Iunes, P.J., Guedes, S., Tello Saenz, C.A., Hackspacher, P.C., Lima-Filho, F.P., 2005. The use of apatite fission track thermochronology to constrain fault movements and sedimentary basin evolution in northeastern Brazil. Radiation Measurements 39, 627–633. https://doi.org/10.1016/j.radmeas.2004.12.006

de Castro, D.L., de Oliveira, D.C., Gomes Castelo Branco, R.M., 2007. On the tectonics of the Neocomian Rio do Peixe Rift Basin, NE Brazil: Lessons from gravity, magnetics, and radiometric data. Journal of South American Earth Sciences 24, 184–202. https://doi.org/10.1016/j.jsames.2007.04.001

Destro, N., 1995. Release fault: A variety of cross fault in linked extensional fault systems, in the Sergipe-Alagoas Basin, NE Brazil. Journal of Structural Geology 17. https://doi.org/10.1016/0191-8141(94)00088-H

Exner, U., Tschegg, C., 2012. Preferential cataclastic grain size reduction of feldspar in deformation bands in poorly consolidated arkosic sands. Journal of Structural Geology 43, 63–72. https://doi.org/10.1016/j.jsg.2012.08.005

Fossen, H., Soliva, R., Ballas, G., Trzaskos, B., Cavalcante, C., Schultz, R.A., Cie, S. De, Postal, C., Polite, C., Sa, U. De, 2017. A review of deformation bands in reservoir

sandstones : geometries , mechanisms and distribution. Geological Society of London Special Publication 459. https://doi.org/10.1144/SP459.4

Françolin, J.B.L., Cobbold, P.R., Szatmari, P., 1994. Faulting in the Early Cretaceous Rio do Peixe basin (NE Brazil) and its significance for the opening of the Atlantic. 16, 647–661.

Françolin, J. B.L., Cobbold, P.R., Szatmari, P., 1994. Faulting in the Early Cretaceous Rio do Peixe basin (NE Brazil) and its significance for the opening of the Atlantic. Journal of Structural Geology 16, 647–661. https://doi.org/10.1016/0191-8141(94)90116-3

Gajst, H., Weinberger, R., Zhu, W., Lyakhovsky, V., Marco, S., Shalev, E., 2018. Effects of pre-existing faults on compaction localization in porous sandstones. Tectonophysics 747–748, 1–15. https://doi.org/10.1016/j.tecto.2018.09.002

Heilbronner, R., Keulen, N., 2006. Grain size and grain shape analysis of fault rocks. Tectonophysics 427, 199–216. https://doi.org/10.1016/j.tecto.2006.05.020

Hower, J., Eslinger, E. V., Hower, M.E., Perry, E.A., 1976. Mechanism of burial metamorphism of argillaceous sedirnent : 1. Mineralogical and chemical evidence. Geological Society of America Bulletin 87, 725–737. https://doi.org/10.1130/0016-7606(1976)87<725

Jagodzinski, H., 1949. Eindimensionale Fehlordnung in Kristallen und ihr Einfluss auf die Röntgeninterferenzen. I. Berechnung des Fehlordnungsgrades aus den Röntgenintensitäten. Acta Crystallographica 2, 201–207. https://doi.org/10.1107/s0365110x49000552

Maciel, I.B., Dettori, A., Balsamo, F., Bezerra, F.H.R., Vieira, M.M., Nogueira, F.C.C., Savioli-Mariani, E., Sousa, J.A.B., 2018. Structural Control on Clay Mineral Authigenesis in Faulted Arkosic Sandstone of the Rio do Peixe. Minerals 8, 17. https://doi.org/10.3390/min8090408

Maciel, I.B., Silicificação hidrotermal e bandas de deformação: influência na arquitetura interna de falhas na Bacia Rio do Peixe, Brasil /PhD thesis dissertation - 2020. 106f.: il.

Meneghini, F., Botti, F., Aldega, L., Boschi, C., Corrado, S., Marroni, M., Pandolfi, L., 2012. Hot fluid pumping along shallow-level collisional thrusts: The Monte Rentella Shear Zone, Umbria Apennine, Italy. Journal of Structural Geology 37, 36–52. https://doi.org/10.1016/j.jsg.2012.02.004

Nicchio, M.A., Nogueira, F.C.C., Balsamo, F., Souza, J.A.B., Carvalho, B.R.B.M.,

Bezerra, F.H.R., 2018. Development of cataclastic foliation in deformation bands in feldspar-rich conglomerates of the Rio do Peixe Basin, NE Brazil. Journal of Structural Geology 107, 132–141. https://doi.org/10.1016/j.jsg.2017.12.013

Nogueira, F.C.C., Marques, F.O., Bezerra, F.H.R., de Castro, D.L., Fuck, R.A., 2015. Cretaceous intracontinental rifting and post-rift inversion in NE Brazil: Insights from the Rio do Peixe Basin. Tectonophysics 644, 92–107. https://doi.org/10.1016/j.tecto.2014.12.016

Nogueira, F.C.C., Nicchio, M.A., Balsamo, F., Souza, J.A.B., Silva, I.V.L., Bezerra, F.H.R., Vasconcelos, L., Carvalho, B.R.B.M., 2021. The influence of the cataclastic matrix on the petrophysical properties of deformation bands in arkosic sandstones. Marine and Petroleum Geology 124, 15. https://doi.org/10.1016/j.marpetgeo.2020.104825

Philit, S., Soliva, R., Castilla, R., Ballas, G., Taillefer, A., 2018. Clusters of cataclastic deformation bands in porous sandstones. Journal of Structural Geology 114, 235–250. https://doi.org/10.1016/j.jsg.2018.04.013

Pittman, E.D., 1992. Relationship of porosity and permeability to various parameters derived from mercury injection-capillary pressure curves for sandstone. American Association of Petroleum Geologists Bulletin 76, 191–198. https://doi.org/10.1306/bdff87a4-1718-11d7-8645000102c1865d

Pizzati, M., Balsamo, F., Storti, F., 2020. Displacement-dependent microstructural and petrophysical properties of deformation bands and gouges in poorly lithified sandstone deformed at shallow burial depth (Crotone Basin , Italy). 137, 21. https://doi.org/https://doi.org/10.1016/j.jsg.2020.104069

Pontes, Cayo C C, Nogueira, F.C.C., Bezerra, F.H.R., Balsamo, F., Miranda, T.S., Nicchio, M.A., Souza, J.A.B., Carvalho, B.R.B.M., 2019. Petrophysical properties of deformation bands in high porous sandstones across fault zones in the Rio do Peixe Basin , Brazil. International Journal of Rock Mechanics and Mining Sciences 114, 153–163. https://doi.org/10.1016/j.ijrmms.2018.12.009

Pontes, Cayo C.C., Nogueira, F.C.C., Bezerra, F.H.R., Balsamo, F., Miranda, T.S., Nicchio, M.A., Souza, J.A.B., Carvalho, B.R.B.M., 2019. Petrophysical properties of deformation bands in high porous sandstones across fault zones in the Rio do Peixe Basin, Brazil. International Journal of Rock Mechanics and Mining Sciences 114, 153–163. https://doi.org/10.1016/j.ijrmms.2018.12.009

Roesner, E.H., Lana, C.C., José, A.L.H.&, Melo, H.G. de, 2011. Bacia do Rio do Peixe

(PB): novos resultados biocronoestratigráficos e paleoambientais. Paleontologia: Cenários de Vida.

Rotevatn, A., Torabi, A., Fossen, H., Braathen, A., 2008. Slipped deformation bands: A new type of cataclastic deformation bands in Western Sinai, Suez rift, Egypt. Journal of Structural Geology 30, 1317–1331. https://doi.org/10.1016/j.jsg.2008.06.010

Rutter, E.H., 1986. On the nomenclature of mode of failure transitions in rocks. Tectonophysics 122, 381–387.

Sénant, J., Popoff, M., 1991. Early Cretaceous extension in northeast Brazil related to the South Atlantic opening. Tectonophysics 198, 35–46. https://doi.org/10.1016/0040-1951(91)90129-G

Shipton, Z. K., Evans, J. P., Abercrombie, R. E., & Brodsky, E. E. (2006). The missing sinks: Slip localization in faults, damage zones, and the seismic energy budget. Geophysical Monograph Series, 170(June 2014), 217–222. https://doi.org/10.1029/170GM22

Silva, J.G.F. da, Córdoba, V.C., Caldas, L.H. de O., 2014. Proposta de novas unidades litoestratigráficas para o Devoniano da Bacia do Rio do Peixe, Nordeste do Brasil. Brazilian Journal of Geology 44, 561–578. https://doi.org/10.5327/Z23174889201400040004

Silva, M.E., Nogueira, F.C.C., Pérez, Y.A.R., Vasconcelos, D.L., Stohler, R.C., Sanglard, J.C.D., Balsamo, F., Bezerra, F.H.R., Carvalho, B.R.B.M., Souza, J.A.B., 2021. Permeability modeling of a basin-bounding fault damage zone in the Rio do Peixe Basin, Brazil. Marine and Petroleum Geology 135, 105409. https://doi.org/10.1016/j.marpetgeo.2021.105409

Smeraglia, L., Trippetta, F., Carminati, E., Mollo, S., 2014. Tectonic control on the petrophysical properties of foredeeo sandstone in the Central Apennines, Italy. Journal of Geophysical Research : Solid Earth 119, 9077–9094. https://doi.org/10.1002/2014JB011221

Soliva, R., Ballas, G., Fossen, H., Philit, S., 2016. Tectonic regime controls clustering of deformation bands in porous sandstone. Geology 44, 423–426. https://doi.org/10.1130/G37585.1

Soliva, R., Schultz, R.A., Ballas, G., Taboada, A., Wibberley, C., Saillet, E., Benedicto, A., 2013. A model of strain localization in porous sandstone as a function of tectonic setting, burial and material properties; new insight from Provence (southern France). Journal of Structural Geology 49, 50–63. https://doi.org/10.1016/j.jsg.2012.11.011

Środoń, J., 1999. Use of clay minerals in reconstructing geological processes: recent advances and some perspectives. Clay Minerals 34, 27–37. https://doi.org/10.1180/000985599546046

Storti, F., Balsamo, F., Salvini, F., 2007. Particle shape evolution in natural carbonate granular wear material. Terra Nova 19, 344–352. https://doi.org/10.1111/j.1365-3121.2007.00758.x

Torabi, A., Balsamo, F., Nogueira, F.C.C., Vasconcelos, D.L., Silva, A.C.E., Bezerra, F.H.R., Souza, J.A.B., 2021. Variation of thickness, internal structure and petrophysical properties in a deformation band fault zone in siliciclastic rocks. Marine and Petroleum Geology 133, 105297. https://doi.org/10.1016/j.marpetgeo.2021.105297

Torabi, A., Fossen, H., 2009. Spatial variation of microstructure and petrophysical properties along deformation bands in reservoir sandstones. AAPG Bulletin 93, 919–938. https://doi.org/10.1306/03270908161

Torabi, A., Fossen, H., Braathen, A., 2013. Insight into petrophysical properties of deformed sandstone reservoirs. AAPG Bulletin 97, 619–637. https://doi.org/10.1306/10031212040

Vasconcelos, D.L., Marques, F.O., Nogueira, F.C.C., Perez, Y.A.R., Bezerra, F.H.R., Stohler, R.C., Souza, J.A.B., 2020. Tectonic inversion assessed by integration of geological and geophysical data: The intracontinental Rio do Peixe Basin, NE Brazil. Basin Research 1–24. https://doi.org/10.1111/bre.12491

Williams, R.T., Goodwin, L.B., Mozley, P.S., 2017. Diagenetic controls on the evolution of fault-zone architecture and permeability structure: Implications for episodicity of fault-zone fluid transport in extensional basins. Bulletin of the Geological Society of America 129, 464–478. https://doi.org/10.1130/B31443.1

Chapter 4 - The influence of the cataclastic matrix on the petrophysical properties of deformation bands in arkosic sandstones

This chapter is presented in the form of a manuscript that is published in the Journal of Structural Geology. In this work we describe the effects of progressive deformation on silisciclastic reservoir. In a multidisciplinary approach, we used structural, miscrostructural, chemical, petrophysical and geomechanical data to characterize the effects of fault-induced rock compaction on the strain intensity and sealing behavior of siliciclastic reservoir, were deformation bands are frequent on faulted zones. As main conclusion, we proposed a strain evolution model where the fault-induced compaction dictates the strain intensity and the sealing potential of subsequent deformation bands in siliciclastic reservoirs.

PUBLISHED ARTICLE

Francisco Cézar Costa Nogueira[a, *]; Matheus Amador Nicchio [b]; Fabrizio Balsamo[b]; Jorge André Braz de Souza[c]; I.V.L. Silva[a]; Francisco Hilario Rego Bezerra[d]; D.L. Vasconcelos[a]; B.R.B.M. Carvalho[c].

[a] Universidade Federal da Campina Grande, Campina Grande, PB, Brazil;
[b] Department of Chemistry, Life Science and Environmental Sustainability, University of Parma, Parma, Italy;
[c] Petrobras Research Center, Rio de Janeiro, RJ, Brazil;
[d] Universidade Federal Do Rio Grande Do Norte, Natal, RN, Brazil;

Published in: Marine and Petroleum Geology.

Date of first submission: 31/03/2020.

Date of second submission: 04/11/2020.

Accepted in: 16/11/2020.

Available online in: 20/11/2020.

DOI: https://doi.org/10.1016/j.marpetgeo.2020.104825

Abstract

This study investigates how cataclastic deformation mechanisms influence petrophysical properties, such as pore diameter, grain size, porosity, and permeability, in

deformation bands (DBs) of arkosic sandstones and conglomerates affected by normal fault zones in the Rio do Peixe Basin, Brazil. We analysed in detail the cataclastic matrix within the deformation bands, defined as the amount of fine particles (<1000 μm) generated by grain crushing that surround the coarse particles. We collected data in deformation bands exhibiting protocataclastic, cataclastic, and ultracataclastic textures, and we performed structural, microstructural, and petrophysical analyses to establish the geometry, temporal relations, kinematics evolution, and associated stresses responsible for the formation and evolution of the deformation bands. Deformation bands evolve progressively with increasing grain comminution, which result in different cataclastic textures within a normal fault system. These textures influence petrophysical properties, mainly porosity. For example, an increase in the cataclastic matrix generates a decrease in macropores, affecting the pore access. The arkosic and arkosic-lithic sandstones present more selective intragranular fracturing of feldspar grains than of quartz grains. This fact indicates some degree of mineralogical control on the grain size distribution and porosity. As a result, in the ultracataclastic deformation bands, quartz clasts are relatively well preserved, and feldspar grains are almost completely destroyed. Our study indicates that it is possible to estimate the relative porosity reduction of deformation bands by analysing the amount of cataclastic matrix. These results could greatly influence reservoir properties in faulted arkosic sandstones.

Keywords: Cataclastic band; permeability, porosity, pore diameter, cataclastic matrix.

4.1 Introduction

Fault zones have been recognized to influence petrophysical and permeability behaviours in hydrocarbon reservoirs, ranging from effective barriers through baffles and conduits to fluid flow. In this context, the understanding of petrophysical property evolution in deformed zones and the resulting fluid flow pattern has been a focus of research in both academia and industry for the past few decades. Several studies have described the petrophysical properties of faulted rocks to predict how major and minor structures influence fluid flow patterns in reservoirs (e.g., Seeburger et al., 1991; Gibson 1998; Knipe et al., 1998; Faulkner et al., 2010). In porous rocks, thin tabular structures

known as deformation bands (DBs) (Aydin, 1978; Aydin and Johnson, 1978; Johnson, 1995; Davis, 1999; Fossen et al., 2007) can dramatically reduce the porosity and permeability, thus providing flow barriers compared with non-deformed rocks (Antonellini and Aydin, 1994; Holcomb et al., 2007; Faulkner et al., 2010; Balsamo and Storti, 2010). In contrast, some workers have shown that in rare cases, deformation bands are also capable of acting as fluid conduits under specific hydrologic circumstances (Sample et al., 2006; Balsamo et al., 2012). In either case, the formation and evolution of deformation bands in fault zones may potentially result in petrophysical and permeability anisotropies, which impact both the mechanical and hydraulic architecture of rocks, with consequences for reservoir drilling and development (Sternlof et al., 2006; Rotevatn et al., 2017).

The development of deformation bands may involve various deformation mechanisms, including non-destructive particulate flow (grain rearrangement), cataclasis (grain fragmentation, translation, and rotation), clay/phyllosilicate smearing, and dissolution-cementation (Fossen et al., 2007, and references therein). The effect of deformation bands on fluid flow in hydrocarbon reservoirs may depend on several factors (e.g., Ballas et al., 2015), including on deformation mechanism, cataclasis or not (Torabi and Fossen, 2009), band thickness, frequency, distribution, geometry and connectivity of the bands in 3D are important factors, and these are related to the properties of the sediment or sedimentary rock: porosity, grain size, grain sorting, chemical compaction, cementation and mineralogy and external conditions, notably tectonic regime, burial depth, formation pore fluid (over) pressure (Fossen et al., 2017).

It follows that cataclasis associated with mechanical fragmentation and reorganization of comminuted grains into a more compacted fabric (Fossen et al., 2007) significantly affects the petrophysical properties of deformation bands compared with non-cataclastic deformation mechanisms (Torabi et al., 2013). The magnitude of cataclasis, generally indicated by the proportion of fine particles (i.e., the cataclastic matrix), allows the differentiation and classification of deformation mechanisms as crush microbreccia, proto-cataclasis, cataclasis, and ultra-cataclasis (Sibson, 1977; Killick, 2003). The amount of cataclastic matrix, which commonly increases with deformation intensity, controls the effectiveness of the seal potential (Pittman, 1981; Ballas et al., 2012). Therefore, several studies have shown that cataclastic deformation bands are responsible for the reduction of host rock porosities by one order of magnitude with

associated permeability reductions of more than two orders of magnitude (Antonellini and Aydin, 1994; Fisher and Knipe, 2001; Fossen and Bale, 2007; Ballas et al., 2015 and references therein).

Despite the large number of field and laboratory studies on cataclastic deformation bands that document a range of porosity and permeability reductions (Ballas et al., 2012; Saillet and Wibberley, 2013; Pizzati et al., 2020), a quantitative relationship between the intensity of cataclasis and petrophysical properties (pore size, grain size, porosity, and permeability), has not yet available in the literature. In this study, we address this issue by comparing the petrophysical properties of undeformed rocks and cataclastic deformation bands, developed in a normal fault zone in the Rio do Peixe Basin (RPB), Brazil (Fig. 4.1). We used detailed geological and structural mapping, integrated with petrography, mineralogical characterization, and petrophysics measurements. Data were collected from deformation bands (between deformation bands, singles bands, clusters and slip surface) exhibiting three cataclastic textures (protocataclastic, cataclastic, and ultracataclastic) developed within coarse sandstone to conglomerate. We conclude that in the same fault zone, there is a progressive decrease in deformation band porosity and a reduction in pore diameter with increasing generation of the cataclastic matrix. These findings may have direct implications for sandstone reservoir quality in structurally complex settings.

4.2 Geological setting

The Rio do Peixe Basin (RPB) is an Early Cretaceous intracontinental half-graben basin located in northeastern Brazil (Fig. 4.1A). The development of this basin is related to the brittle reactivation of E-W- and NE-SW-striking Neoproterozoic ductile shear zones, known as the Patos and Portalegre shear zones, respectively (Fig. 4.1B) (Sénant and Popoff, 1991; Françolin et al., 1994; de Castro et al., 2007). Both shear zones were reactivated as brittle faults during the Cretaceous rifting that lead to the opening of the South Atlantic Ocean (Sénant and Popoff, 1991; Françolin et al., 1994; de Castro et al., 2007). The sedimentary fill in the RPB comprises siliciclastic deposits of the Early Cretaceous (145 to 130 Ma), which are grouped into three lithostratigraphic formations: Antenor Navarro, Sousa, and Rio Piranhas (Sénant and Popoff, 1991). The Antenor Navarro Formation (~ 1,000 m thick) is composed of coarse- to medium-grained arkosic sandstones and local conglomerates, with trough cross stratification, deposited in alluvial

fans and fluvial braided systems. The Souza Formation (~ 1,000 m thick) is composed of siltstones and shales, locally calcareous, with cross and planar stratifications, deposited in a lacustrine system. Finally, the Rio Piranhas Formation (~ 400 m thick) includes sandstones and conglomerates with cross and planar stratifications deposited in alluvial fans and fluvial braided systems.

The structural evolution of the RPB was studied by Nogueira et al. (2015). They identified two tectonic phases: syn-rift and post-rift. The first phase (syn-rift) was responsible for the formation of the basin. This was an extensional phase that generated major high-angle normal faults, the E-W-striking Malta and the NE-SW-striking Portalegre and Rio Piranhas faults. The second phase is marked by tectonic inversion of the basin, in response to ENE-WNW shortening.

More recently, a few compositional and structural aspects of deformation bands in the RPB have been investigated. These bands form single cm-thick tabular and clustered zones of cataclastic deformation in the feldspar-rich sandstones and conglomerates of the rift sequence close to a major fault (Araújo et al., 2018). A more detailed look at the fault zone reveals that the rock presents a strong increase in degree of cohesion occurs towards complex fault zones with multiple fault cores. These bands form a pervasive cataclastic foliation composed of preferential alignment of intensely comminuted feldspar fragments along thin slip zones. These processes were purely mechanical (i.e., grain crushing and reorientation), and no clays or fluids were involved (Nicchio et al., 2018). In addition, the tight cataclastic fabric inside the deformation bands prevented the weathering of feldspar, thus inhibiting clay authigenesis. For example, in the protolith far from faults, clay minerals such as smectite, illite, and subordinate kaolinite occur and were formed after sediment deposition. Within fault zones, however, these clay minerals are absent or significantly fewer than those in the undeformed sandstone, which indicates that the development of fault zones in high-porosity arkosic sandstones prevents clay mineral authigenesis (Maciel et al., 2018). These results indicate the complexity of factors affecting the petrophysical properties of deformation bands in the RPB.

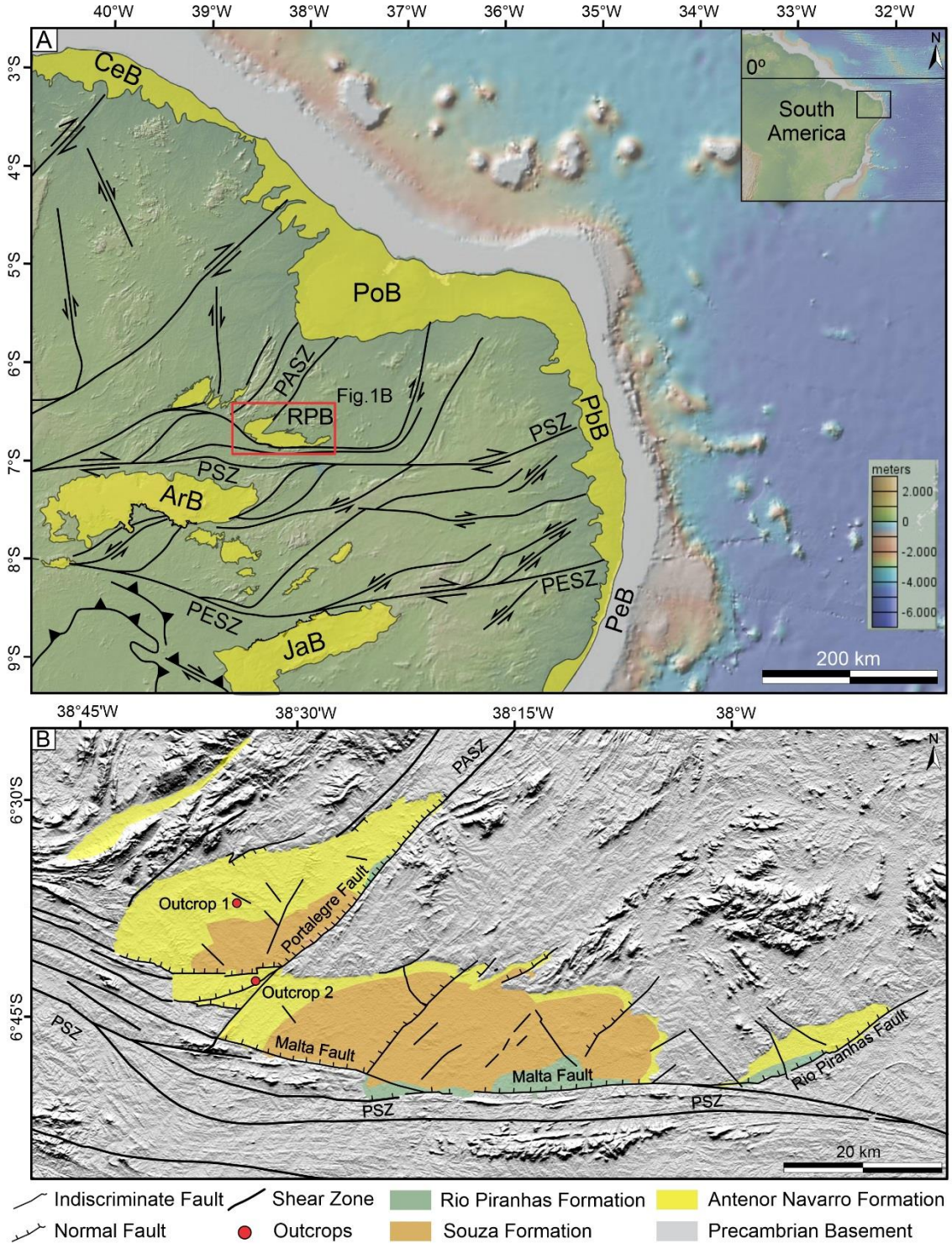

Figure 4.1. (A) Topographic map of the Borborema Province, showing the main ductile shear zones in the crystalline Precambrian basement and marginal and interior basins (topography from the Global Relief Model from GeoMapApp 3.6.10). The black lines mark the border of sedimentary basins. CeB (Ceará Basin), PoB (Portiguar Basin), PbB (Paraíba Basin), PeB (Pernambuco Basin), ArB (Araripe Basin), JaB (Jatobá Basin), and RPB (Rio do Peixe Basin). The geometry of sedimentary basins and shear zones are based on Matos (1992) and Brito Neves et al. (2000), respectively. The main shear zones, namely PASZ (Portalegre Shear Zone), PSZ (Patos Shear Zone) and PESZ (Penambuco Shear Zone). (B) Relief Model from TOPODATA Project (Valeriano and Albuquerque,

2010). Geological framework of the Rio do Peixe Basin, indicating the Brejo das Freiras (BFSB), Sousa (SSB) and Pombal (PSB) sub-basins, and studied outcrops (geological map modified from Françolin et al. (1994) and Nogueira et al. (2015).

4.3 Methods

In this work, we integrated structural, microstructural, and petrophysical data acquired in undeformed and faulted coarse sandstones and conglomerates affected by deformation bands (Fig. 4.1). We applied structural analysis techniques at outcrops to establish the geometry, temporal relations, kinematics, and strains responsible for the formation and evolution of the deformation bands. The structural mapping was performed by interpretation of high-resolution unmanned aerial vehicle (UAV) imagery of outcrops (Fig. 4.2A), where we collected representative samples from the main sets. For this purpose, we obtained cylindrical samples (plugs) 3.54 cm in diameter using a motorized drill. Due to their lack of cohesion, undeformed rock samples could not be drilled, and representative pieces were extracted using a geological hammer. The samples were collected from two outcrops that exhibit different structural characteristics (Fig. 4.1): 45 deformed samples from thirty sites in outcrop 2 and 04 undeformed samples (protolith) from outcrop 1 (Fig. 4.2A). All samples were collected from the same sandstones of the Antenor Navarro Formation (Fig. 4.1B), and collected on surface outcrops.

Microstructural analysis was carried out to identify and document the deformation mechanisms within different structural domains and to quantify the amount of cataclastic matrix in each deformation band. The cataclastic matrix in deformed rocks was characterized by the number of fine particles surrounding the coarse particles. To classify the deformation bands, we used the amount of cataclastic matrix within the deformation band as a parameter (Killick, 2003). We used images of polished, 30 µm-thick thin sections impregnated with blue epoxy. The selected samples include protocataclastic (<50% cataclastic matrix), cataclastic (50-90% cataclastic matrix), and ultracataclastic (90-100% cataclastic matrix) deformation bands. The sample of the protocataclastic texture were collected in the volume of rock between adjacent deformation bands developed within the same fault zone, which we refer in this study to between deformation bands (Fig. 4.2B, D). The samples of the cataclastic and ultracataclastic bands were collected in single bands, clusters, and slip surfaces (Fig. 4.2B, C, D). We identified the cataclastic matrix, likely generated by grain crushing as the amount (area % in 2D) of finer particles (with a diameter <1000 µm that surround the coarser particles). We took

the whole area of the studied deformation band and subtracted the area of the grains (>1000 μm) and pores to calculate the amount of matrix. We classified the remaining area as the cataclastic matrix and divided it by the total investigated area to calculate the percentage of the matrix. We analysed the particle sizes of the protolith using sieving and thin section imagery analysis. The analyses by the sieving method were performed in two samples, one coarse sandstone and another fine conglomerate, where the different sedimentary fraction sizes (clays <4 μm; silt <62 μm; sand <2mm - >62 μm; and gravel >2mm) were represented in percentages (Fig. 4.3A). In thin section, we analysed the fraction between 5000-4 μm and measured the grain diameters. We then grouped the results in the same way we organised the sieving results.

Based on microscopic observations and the amount of cataclastic matrix, the deformation bands were classified as protocataclastic (4 samples), cataclastic (20 samples), and ultracataclastic deformation bands (21 samples). The 2D petrophysical (porosity and permeability) analyses were also performed on polished, 30 μm-thick petrographic thin sections impregnated with blue epoxy. We used the image analysis software AvisoFire® to quantify the percentage of 2D porosity and the amount of cataclastic matrix. The 2D porosity represents the total porosity, the total void space in the rock whether or not it contributes to fluid flow. We used different combinations of RGB patterns with the help of the interactive thresholding tool, which allows the identification of micropores and very small grains, to identify pores and grains. We also applied a filter to remove small holes, which allows the removal of very small holes on the grain and pore surfaces. The erosion filter was also used to identify grains, even in highly deformed zones. Then, we removed particles or noises below the resolution of the method with the small spot removal filter. Finally, we used the label analysis filter to calculate the parameters such as diameters and area occupied by the particles.

The 2D permeability of undeformed and faulted rocks was measured using the method proposed in Torabi et al. (2007) and calculated with MATLAB R2018a. These analyses were performed to obtain the porosity and permeability attributes of both the undeformed rocks and the different types of deformation bands. In the thin section, the 2D permeability also was measured at the internal zone of the deformation band and host rock, aiming to quantify the permeability reduction. Furthermore, we measured the pore access and 3D porosity correspondent to the effective porosity, excluding isolated pores and pore volume. These pores were occupied by water adsorbed by grains, through

mercury (Hg) intrusion analyses using a Quantachrome PoreMaster33, which provided pore diameter in the range 1100-0.0064 μm (see Data Repository in Balsamo et al., 2014). We analysed the grain size distribution using thin section imagery in undeformed and deformed rocks. The curves of grain size distribution were generated to protolith and different intensity of the cataclasis. We also investigated grain size distribution within deformation band and external zone (host rock) of the deformation band in thin section. To minimize the effects caused by the high frequency of small grains that occupy the space of a sole major grain, we have used the method proposed by Nicchio et al. (2018), that compares the 1000 highest grain size values of each undeformed and deformed rocks. The lowest grain diameter values identified by the software was 4.6 μm on thin section images. Within deformation bands, the grain size distribution analyses were focused on the smaller diameter fragments, showing a high frequency of grains, especially in the range between 4.6 μm and 300 μm. In this range, it was possible to distinguish the deformed grains within from the grains outside the cataclastic matrix.

To describe the mineralogical composition of the cataclastic matrix and stablish the compositional relationship between the surviving grains, we used scanning electron microscopy imagery (SEM) of two cataclastic bands: one with cataclastic and another ultracataclastic texture. We used these images to build high resolution compositional maps that allowed us to identify grain less than 1.92 μm in diameter. In the present study, we use the term survivor grains to indicate clasts with diameters of 10-20 μm still visible within the cataclastic matrix of deformation bands (Cladouhos, 1999).

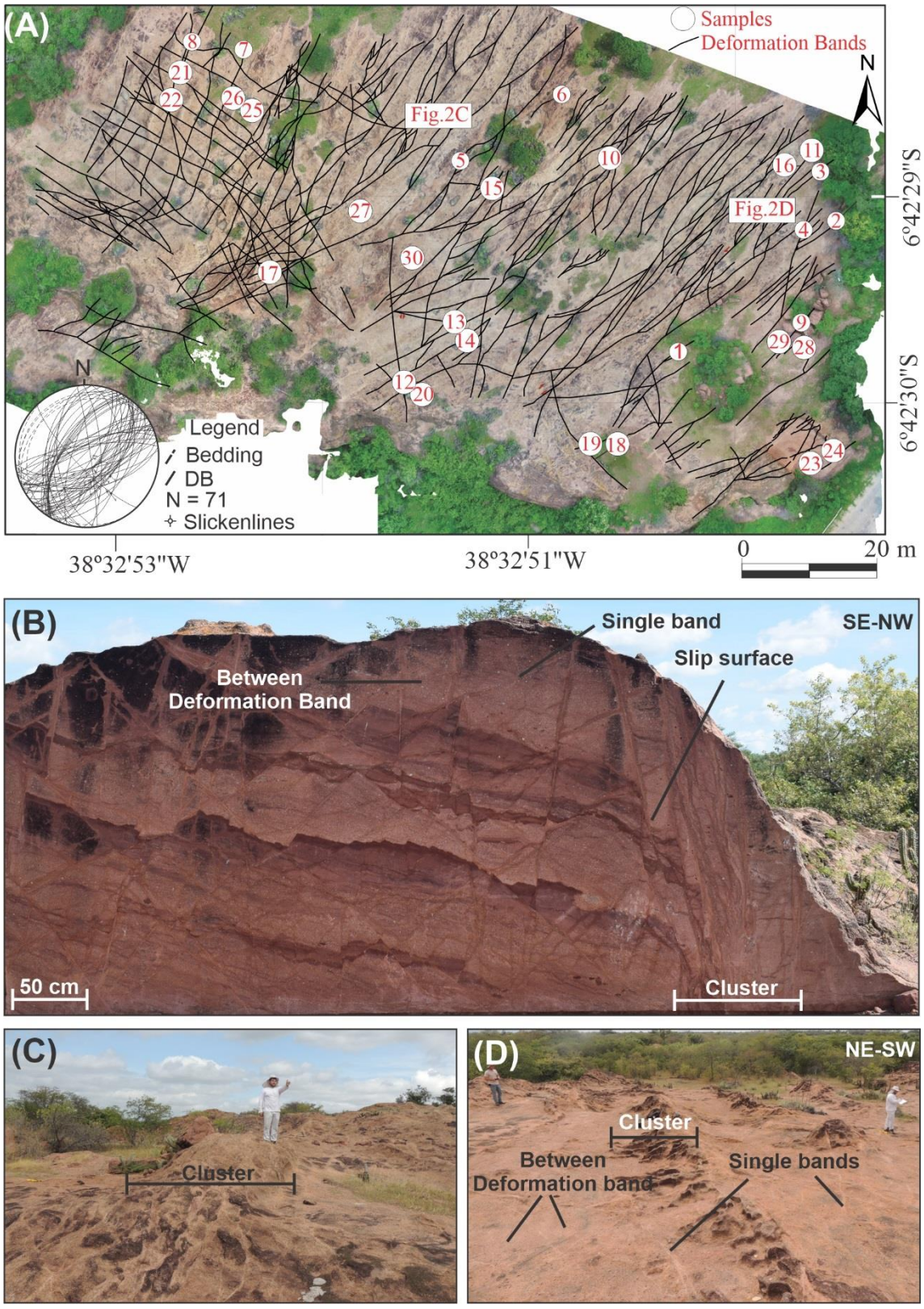

Figure 4.2: (A) Unmanned aerial Vehicle (UAV) imagery indicating sample locations (white circles numbered in red) and traces of deformation bands (black lines). Stereonet (lower hemisphere of equal area net) showing the average orientation of (black) NE- (DB 1) and (red) ENE-striking faults (DB 2) and related mean slickenlines, as well as sedimentary bedding. N = number of measurements. (B) Detail of area between deformation bands, single deformation bands, cluster zones, and slip surfaces. Location

of Figure 4.2B in Figure 4.2A (site 23). (C) Area of cluster zone. The person's arm points to north. (D) Area of between deformation bands, single deformation bands, and cluster zones. Location of Figures 4.2C and 2D in Figure 4.2A.

4.4 Results

4.4.1 Protolith characterization

Outcrop 1 (Fig. 4.1B) is located ~15 km from major rift faults and represents the undeformed units of the RPB. This outcrop consists of poorly lithified sandstones and conglomerates with well-preserved sedimentary structures (mostly cross stratification) without significant deformational features (Fig. 4.3B). The protolith varies from coarse sandstones to fine conglomerates. The rock is grain-supported with little or no matrix (Fig. 4.3C). However, when the matrix is present, it is composed of sand-silt grains, which represent less that 5% of the particles size fraction of the protolith (Fig. 4.3A). The particles size results of coarse sandstones and fine conglomerates from the particle-size analysis by the sieving method, and thin section imagery analysis showed to be more abundant in the range of sand and gravel particles (Fig. 4.3A). In both methods, the sand and gravel fractions together account ~95%, whereas clay and silt are less than 5%. The grains present a moderate to low degree of grain selection with a moderate to low degree of roundness. The mineralogy consists predominantly of quartz grains, as well as feldspar and lithic fragments, with very low contents of phyllosilicates (biotite and muscovite). Due to their high feldspar contents, these rocks are classified as arkose (Fig. 4.3D). We observed strong lithological similarities, such as mineralogical and facies features, when we compared the undeformed rock (outcrop 01, Fig. 4.1) with the deformed rocks (outcrop 02, Fig. 4.1), which were formed in the same depositional system of the Antenor Navarro Formation.

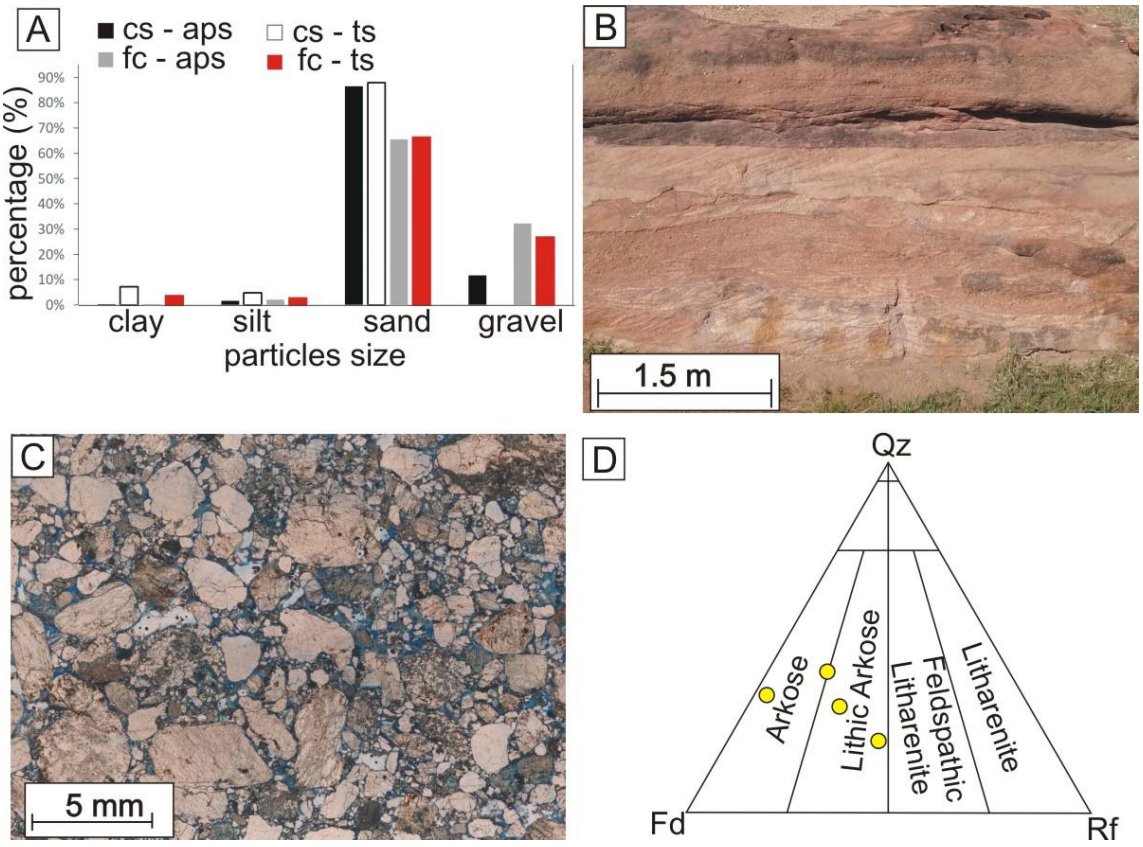

Figure 4.3. (A) Histogram showing the percentage of particle size in host rock. (B) Microscope image of the sandstone with little amount of sedimentary matrix. (C) Thin section of photomicrograph showing the matrix composed of sand-silt grains. (D) Compositional classification of samples based on Folk (1968).

4.4.2 Fault zone characterization

Outcrop 2 (Figs. 4.1B, 2) is located near one of the main rift border faults, the Portalegre fault, and consists of a well-developed, ~80 m-wide fault zone with multiple slip surfaces and deformation bands (DBs) arranged as both single millimetric bands and m-thick clusters surrounding fault slip surfaces. The deformation bands exhibit complex geometry due to their anastomosing nature (Fig. 4.2A) and commonly present positive relief. The structural data show that faults and deformation bands are organized in two conjugate sets (Fig. 4.2B). In map view, NE-SW-striking deformation bands are predominant, with E-W- and NW-SE-striking deformation bands occurring as secondary structures. The NE-SW-striking set varies in different areas of the outcrop, with a NNE-SSW-striking direction in the northwestern part, whereas in the central and southeastern areas of the outcrop, an ENE-WSW-striking set predominates. The E-W-striking set shows discontinuous traces. The NW-SE-striking set exhibits continuous traces of deformation bands and is observed mainly in the northwestern area of the outcrop. In

addition, both E-W- and NE-SW-striking deformation band sets crosscut each other and are offset by the NW-SE-striking deformation band set, with offsets showing apparent strike-slip, right-lateral kinematics (Fig. 4.4A). Cumulative data analysis shows that most faults exhibit extensional kinematics and mainly strike NE-SW, with both NW and SE dip directions (Fig. 4.2A). Contouring of fault slickenlines (Fig. 4.2A) reveals the occurrence of oblique-slip faulting, particularly in the NE-striking set, with oblique striae (Fig. 4.4B) showing systematic normal kinematics with a minor right-lateral component.

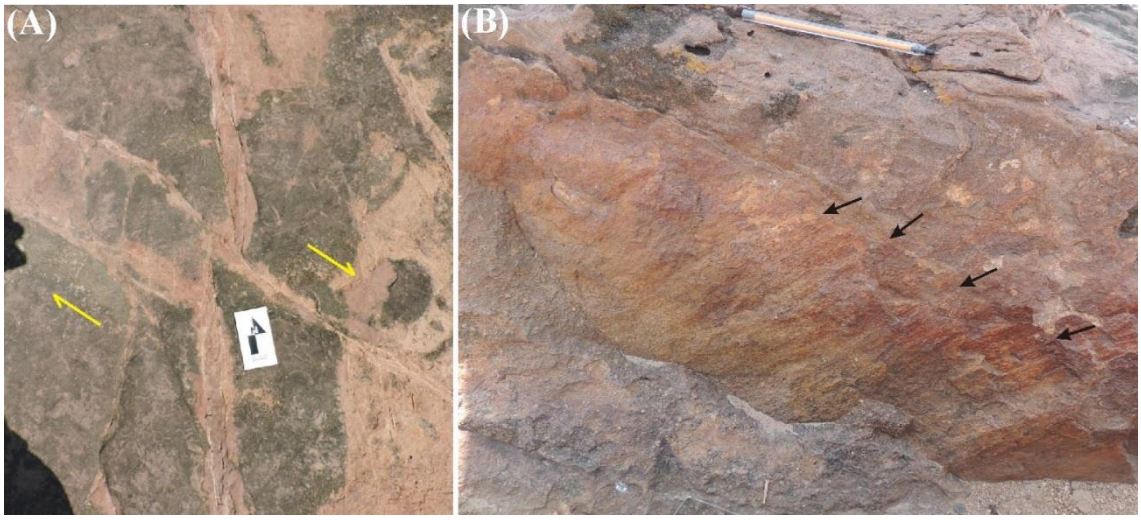

Figure 4.4. Detail of deformation band kinematics: (A) Detail of a NW-SE-striking deformation band cutting a NNE-SSW-striking deformation band. The card for scale indicates N-S direction and yellow arrows show strike-slip right-lateral kinematics. (B) Detail of the slip surface showing the downdip striate oblique to pen. Black arrows indicate striae. Pen points to north. Locations of photos in Figure 2 (photos A and B in sites 12 and 6, respectively).

4.4.3 Petrographic and microstructural analyses

The undeformed rock (outcrop 1) consists of conglomerates and coarse sandstones, mainly composed of quartz, feldspars, and rock fragments, with a high intergranular porosity, poor sorting, and sub-angular grains (Fig. 4.5A). In thin section, the protolith rocks show no evidence of fracture-related grain size reduction.

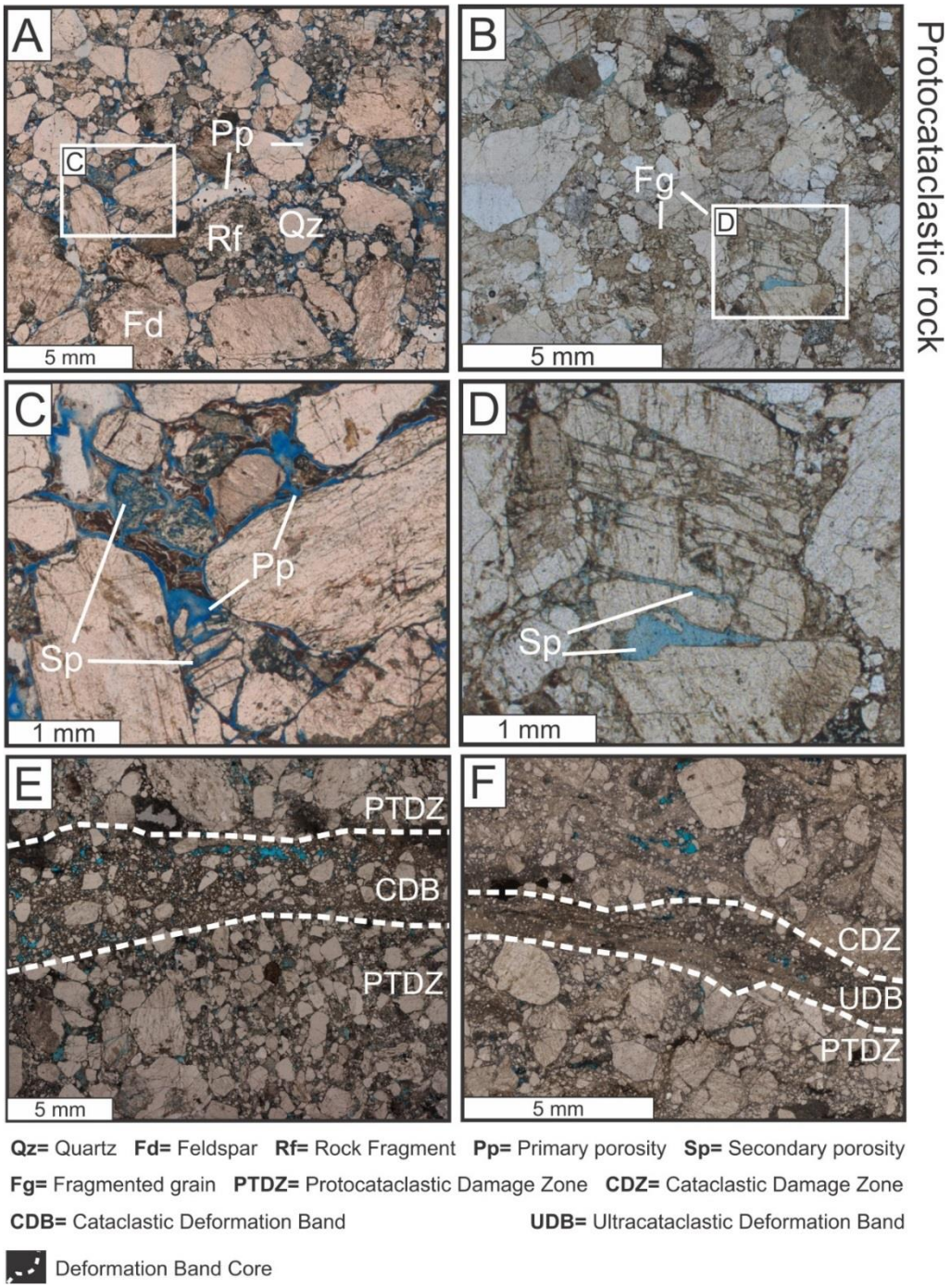

Figure 4.5. Plane-polarized light photomicrograph showing features of protolith and deformed rocks. (A) Microscopic view of the undeformed fine conglomerate. (B) Protocataclastic deformation band exhibiting moderate deformation, with low grain size reduction and formation of secondary porosity. (C) and (D) Detail of secondary porosity formation by grain fracturing. (E) Cataclastic deformation band showing moderate to intense cataclasis, with grain comminution and development of secondary porosity. Note the destruction of grains in the comminution zone. (F) Ultracataclastic deformation band showing very high deformation and generation of cataclastic matrix.

Microstructural analysis indicates that the deformation mechanisms acting in the deformation bands are mainly cataclastic flow, presenting different internal organization

patterns depending on the intensity of the cataclasis acting on them. In the studied outcrop (outcrop 2, Fig. 4.1), low-intensity cataclasis occurs in the between deformation bands, because there is no undeformed rock in this outcrop (Fig. 4.1B). Such zones present absence of internal foliation imparted by grain alignment, and moderate grain size preservation (Fig. 4.5B). The proportion of cataclastic matrix generated by this comminution process can vary from >10% to <50% (Fig. 4.5B). The cataclastic matrix content generated by grain comminution does not exceed 50% and is thus classified as protocataclastic texture. The primary porosity is strongly reduced, with the formation of secondary porosity by grain breakage (Figs. 4.5C, D). The protocataclastic texture exhibit pervasive fragmentation and grain size reduction. Comminution is more intense on the borders of grains, mainly on feldspar grains.

The process of strain localization produces cataclastic deformation bands. Such bands form subparallel shear planes with intense grain comminution. The amount of cataclastic matrix generated by these bands ranges from 50 to 90% (Figs. 4.5E, F). At very high-intensity deformation stages, the generated deformation bands tend to form thin bands of finer grain size with the formation of parallel to sub-parallel little planes, internally the deformation bands (Fig. 4.5F). The most prominent deformation mechanism allows the generation of a cataclastic matrix that reaches more than 90% in content (Fig. 4.5F). All deformation bands presented in this work have in common that the cataclastic intensity decreases outwards from internal zone of the deformation band (Fig. 4.5E, F). Thus, protocataclastic bands are classified around cataclastic and ultracataclastic deformation bands (Fig. 4.5E, F), and cataclastic damage zones surround ultracataclastic deformation bands (Fig. 4.5F).

4.4.4 Petrophysical properties of deformation bands

In this section, we explore the petrophysical properties of deformation bands, such as porosity, permeability, pore size distribution, and the amount of cataclastic matrix vs. porosity. The petrophysical analyses performed in deformed and undeformed sandstones and conglomerates indicate that the 2D porosity is strongly affected by the rock microfabric (Figs. 4.5, 6). The undeformed rocks (UnD) have high mean 2D porosity values equal to 25.48%; the protocataclastic and cataclastic bands have intermediate mean 2D porosity values of 14.87% and 9.44%, respectively; and the ultracataclastic bands

have the lowest mean porosity value of 7.65% (Fig. 4.6). The dispersion of porosity values is also decreasing with cataclasis intensity, from large dispersion in undeformed rock to small dispersion in cataclastic or ultracataclastic structures. This result show that a progressive compaction, which results in grain and pore diameter reductions with a consequent decrease in the bulk 2D porosity dispersion.

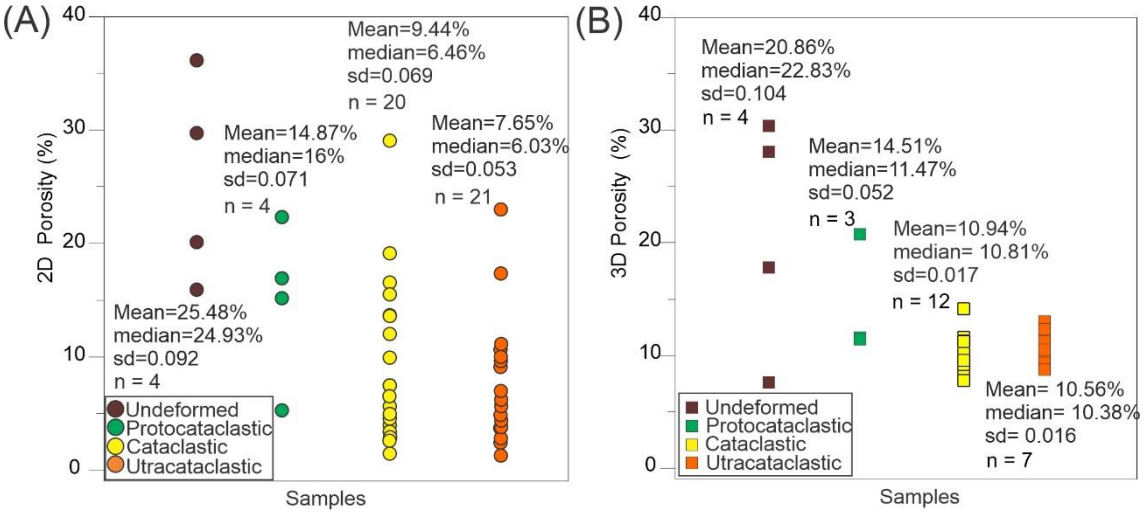

Figure 4.6. Values of porosity in undeformed and deformed samples. The deformed samples were divided into groups related to three cataclasis intensity (Protocataclastic, Cataclastic, and Ultracataclastic) and undeformed rocks. (A) Graphs relating 2D porosity values, and (B) 3D porosity data measured in deformed and undeformed samples. in Key: sample number (n); standard deviation (sd) for sample group.

We calculate the mean 2D permeability using the methodology proposed by Torabi et al. (2007) using thin sections from undeformed samples, where we find a mean value of 8598.33 mD (Fig. 4.7). The protocataclastic bands have a mean permeability of 88.50 mD, which is two orders of magnitude lower than that of the undeformed rocks. Cataclastic deformation bands yield an intermediate mean value of 30.55 mD, whereas the ultracataclastic deformation bands have the lowest average value of 10.71 mD. These results indicate that the permeability data show a behaviour contrary to that of the porosity, showing more variations for the different types of cataclastic bands. We also observed that the permeability dispersion tends to decrease with cataclasis in deformed rocks when compared with that in undeformed rocks (Fig. 4.7). It follows that considering the median permeability values span over six orders of magnitude in the same fault zone (Table 4.1). In conclusion, when compared with undeformed rocks, the mean permeability in protocataclastic, cataclastic, and ultracataclastic samples can show a

decrease of two orders of magnitude (Fig. 4.7A). We also quantified the permeability reduction from internal zone of the deformation bands and host rock, in cataclastic and ultracataclastic bands. The data show a wide range of values, from little permeability change through up to five orders of magnitude reduction in permeability (Fig. 4.7B). Most permeability data show a permeability reduction from 1 to 2 orders of magnitude (78%), which can reach up to 5 orders of magnitude (9.8%) (Fig. 4.7B).

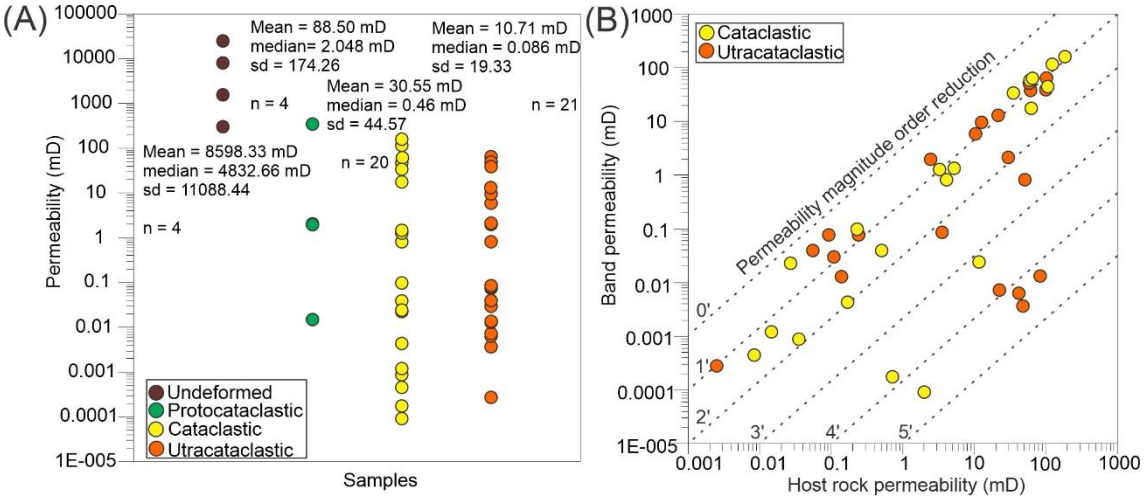

Figure 4.7. (A) Values of 2D permeability in undeformed samples versus deformation band samples (protocataclastic, cataclastic and ultracataclastic), with samples number (n) and standard deviation (sd). All the samples were collected in outcrops 1 and 2. (B) Values of 2D permeability in deformed rock versus host rock permeability.

In all deformation bands, a reduction in the volume of pores >20 μm (Fig. 4.8B, C, D) indicates that these pores have been obliterated in different ways, following a direct and continuous relationship between the development of the pore diameter and 3D porosity (Fig. 4.9). We observed a small correlation coefficient (R2 = 0,73) between pore diameter and 3D porosity (Fig. 4.9). Therefore, the average value of porosity decreases, closed by the cataclastic texture type (Fig. 4.6A, B). The analysis of pore access also indicates a correlation between petrophysical properties and the intensity of cataclasis. The total 3D porosity and pore access obtained through mercury intrusion porosimetry are summarized in Table 4.2 and in Fig. 4.6 and 4.8. The mercury intrusion porosimetry analyses were performed within the deformation bands and restricted to the cataclastic matrix, thus avoiding overlapping data from external and internal zones of the band. The size of the analysed area is variable and limited by the inner portion of the band.

Table 4.1. Table showing permeability values of three groups (protocataclastic, cataclastic and ultracataclastic) of deformation bands (45 samples), undeformed rock permeability (04 samples), and host rocks (41 samples).

Texture of Cataclastic Zone	Permeability (mD)	Host Rock Pemeability (mD)
Undeformed	303.15	
Undeformed	8089.35	
Undeformed	24424.84	
Undeformed	1575.98	
Protocataclastic	0.014	
Protocataclastic	349.89	
Protocataclastic	2.03	
Protocataclastic	2.06	
Cataclastic	17.45	63.40
Cataclastic	58.85	60.06
Cataclastic	44.54	106.66
Cataclastic	1.360	5.23
Cataclastic	64.11	65.69
Cataclastic	114.78	122.68
Cataclastic	0.098	0.226
Cataclastic	0.0012	0.0146
Cataclastic	0.000884	0.035348
Cataclastic	0.022	0.026791
Cataclastic	1.28	3.28
Cataclastic	0.039	0.507
Cataclastic	0.024	11.765
Cataclastic	0.82	4.101
Cataclastic	0.0044	0.1689
Cataclastic	33.77	35.174
Cataclastic	161.23	185.34
Cataclastic	0.000092	1.9946
Cataclastic	0.00018	0.7218
Cataclastic	0.00046	0.008363
Ultracataclastic	48.92	59.68
Ultracataclastic	39.02	99.87
Ultracataclastic	0.0036	48.38
Ultracataclastic	9.57	12.6632
Ultracataclastic	38.62	62.0492
Ultracataclastic	13.08	21.42
Ultracataclastic	5.94	10.434
Ultracataclastic	2.15	30.083
Ultracataclastic	0.086	3.5347
Ultracataclastic	0.00028	0.002507
Ultracataclastic	0.039	0.0556
Ultracataclastic	0.0073	22.6594
Ultracataclastic	0.013	83.5365
Ultracataclastic	0.0063	42.039
Ultracataclastic	0.012	0.1403
Ultracataclastic	1.99	2.44
Ultracataclastic	0.077	0.0919
Ultracataclastic	64.55	102.16
Ultracataclastic	0.03	0.1083
Ultracataclastic	0.82	51.07
Ultracataclastic	0.075	0.2371

The mean 3D porosity of undeformed samples is 20.86%, and the mean pore diameter is 11.44 μm (Fig. 4.8A). The cataclastic and ultracataclastic deformation bands

have mean porosities of 10.94 and 10.56%, respectively, and the smallest mean pore diameter values of 0.44 and 0.22 μm, respectively (Fig. 4.8C, D). In the utltracataclastic samples, the local increase in porosity can be observed by the pore access analysed in Fig. 4.8D, with the appearance of an important diameter peak (Fig. 4.8D), suggesting the occurrence of pores approximately 100 μm in diameter. Protocataclastic deformation bands yield an intermediate 3D porosity value of 14.51% and a mean pore diameter of 6.7 μm. The average pore diameter exhibits a correlation with the porosity properties (Table 4.2). These relationships indicate that the decrease in the average value of 3D porosity results in a decrease in pore diameter and dramatic changes in pore access.

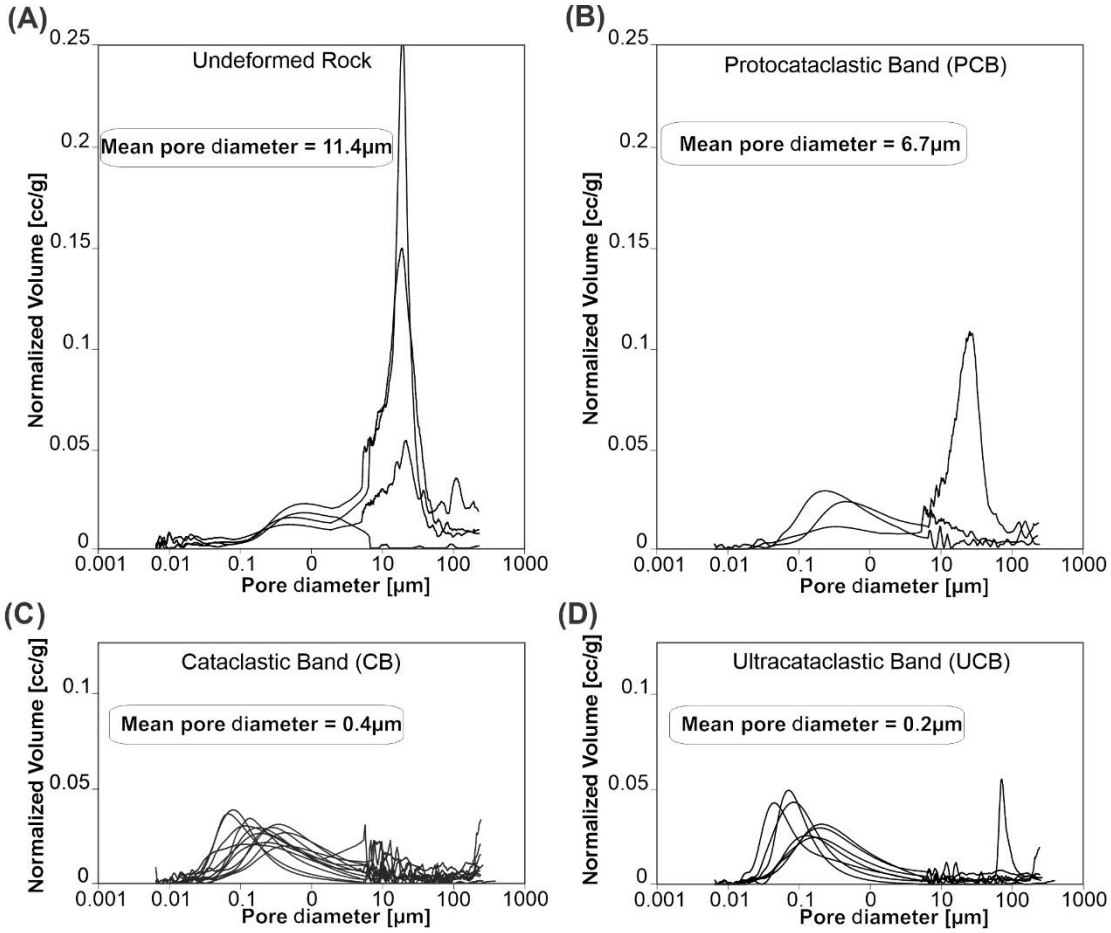

Figure 4.8. Curves of the pore access of (A) undeformed rocks, (B) protocataclastic deformation bands, (C) cataclastic deformation bands, and (D) ultracataclastic deformation bands.

Table 2. 2D and 3D Porosity and pore access data measured in undeformed and deformed samples.

Texture of Cataclastic Zone	2D Porosity (%)	3D Porosity (%)	Pore Acess (μm)
Undeformed	20.12	17.69	15.05
Undeformed	36.15	30.29	13.62
Undeformed	15.92	7.5	0.77

Undeformed	29.72	27.98	16.32
Protocataclastic	13.79	11.45	0.48
Protocataclastic	23.60		
Protocataclastic	30.44	11.47	1.21
Protocataclastic	23.68	20.63	19.2
Cataclastic	29.14		
Cataclastic	12.21		
Cataclastic	4.53		
Cataclastic	6.70		
Cataclastic	13.93	11.96	0.86
Cataclastic	16.69	10.56	0.29
Cataclastic	10.13	12.18	1.5
Cataclastic	5.04	11.89	0.56
Cataclastic	3.37	9.59	0.13
Cataclastic	3.65	9.17	0.28
Cataclastic	15.69	9.84	0.26
Cataclastic	7.69	14.7	0.3
Cataclastic	2.90	11.07	0.52
Cataclastic	1.74		
Cataclastic	4.94		
Cataclastic	13.84	8.42	0.097
Cataclastic	19.26	10.18	0.23
Cataclastic	5.85	11.82	0.33
Cataclastic	5.22		
Cataclastic	6.22		
Ultracataclastic	5.40		
Ultracataclastic	11.42		
Ultracataclastic	17.56		
Ultracataclastic	9.28		
Ultracataclastic	10.84		
Ultracataclastic	6.03		
Ultracataclastic	10.23		
Ultracataclastic	9.87		
Ultracataclastic	2.89		
Ultracataclastic	1.83		
Ultracataclastic	3.26	9.2	0.1
Ultracataclastic	5.20	8,62	0.22
Ultracataclastic	3.56	11.13	0.095
Ultracataclastic	4.06	12.89	0.14
Ultracataclastic	3.15	10.38	0.29
Ultracataclastic	3.15	9.51	0.31
Ultracataclastic	6.41	12.19	0.41
Ultracataclastic	11.37		
Ultracataclastic	23.16		
Ultracataclastic	7.29		
Ultracataclastic	4.68		

The amount of cataclastic matrix, which also quantifies the intensity of cataclasis within the deformation bands, is plotted against the calculated 2D porosity in Figure 4.10. Despite large scattering, the 2D porosity tends to decrease with increasing amounts of cataclastic matrix (Fig. 4.10A). The only ultracataclastic deformation band with fine-grained matrix >90% presents a straight inversely proportional relationship between the amount of cataclastic matrix and the 2D porosity (Fig. 4.10B). The same relation is not

observed in all the samples containing cataclastic bands, where the correlation between matrix percentage and 2D porosity data indicates higher dispersion values than those in ultracataclastic deformation bands.

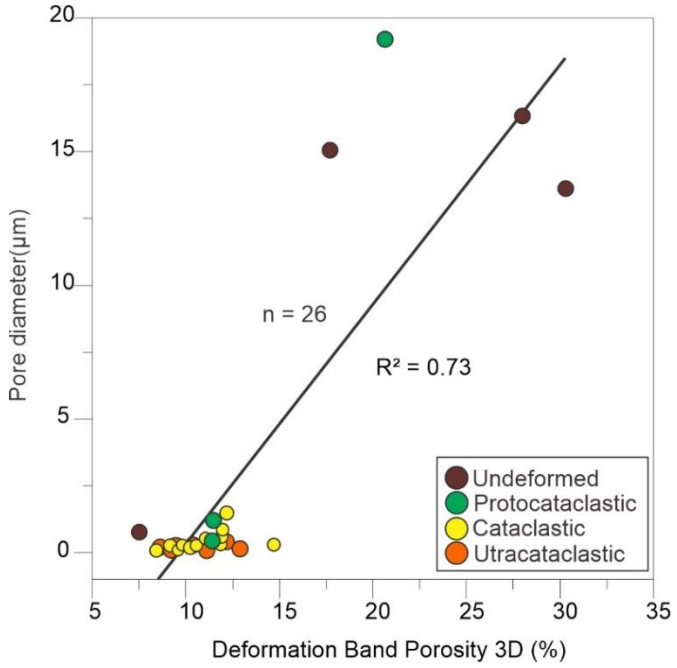

Figure 4.9. Relationship between values of pore access and 3D porosity in undeformed and deformed samples. Key: number of samples (n).

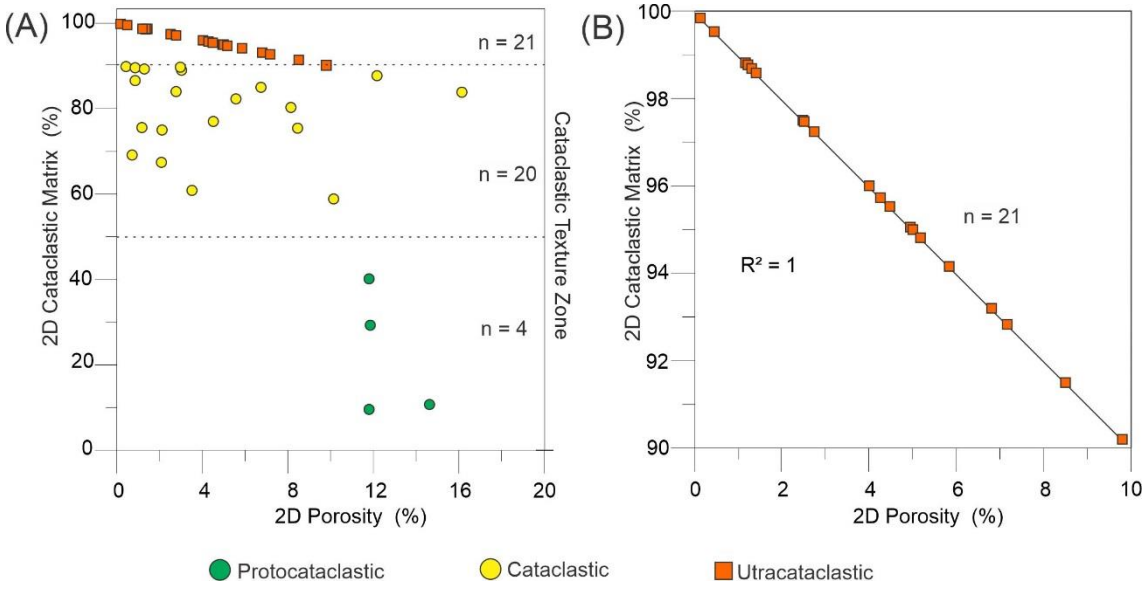

Figure 4.10. Comparisons of 2D parameters from deformation band calculated from thin sections images processing: (A) Porosity vs. cataclastic matrix percentage with identification of protocataclastic, cataclastic, and ultracataclastic zones. (B) Detail graphic showing porosity as a function of distribution of cataclastic matrix on an ultracataclastic texture zone.

The grain size distribution analysed to undeformed samples revealed that range, of values between 240 μm and 5000 μm, with an important two peaks in approximately 390 μm and 1000 μm (Fig. 4.11A). The protocataclastic deformation bands showed values ranging from 4,6 μm to 3300 μm, with peak approximately at 10 μm (Fig. 4.11B). Cataclastic deformation bands recorded maximum values at 2000 μm, with peak approximately at 10 μm (Fig. 4.11C). Ultracatraclastic deformation bands showed lowest grain size with maximum values at 1000 μm, and peak approximately at 5 μm (Fig. 4.11D). When compared the grain size distribution within deformation band and host rock, the host rock shows the values maximum ranging from 100 μm to 190 μm, with peak approximately at 140 μm and 60 μm (Fig. 4.12C, D), to protocataclastic and cataclastic textures, respectively (Fig 4.12 A, B). The internal zone of the deformation band presents grain size reduction, with peak at 40 μm (Fig. 4.12C, D), for both cataclastic and ultracataclastic textures (Fig. 4.12A, B).

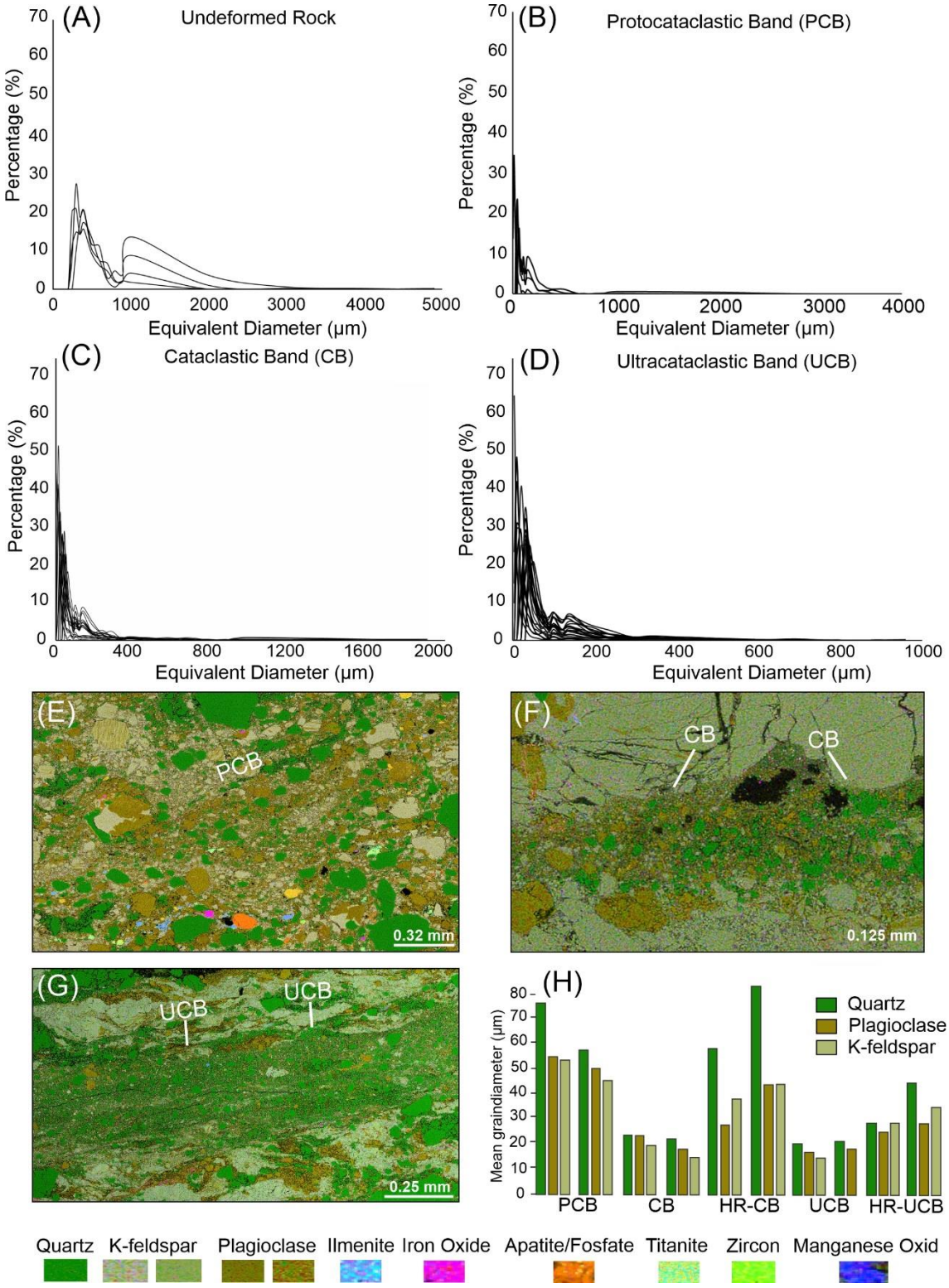

Figure 4.11. Graphs indicating the grain sizes distribution in (A) undeformed samples, (B) protocataclastic bands, (C) cataclastic bands, and (D) ultracataclastic bands. SEM images showing the mineral composition within cataclastic matrix of (E) protocataclastic, (F) cataclastic and (G) ultracataclastic bands. (H) Histogram with box plot showing the mean grain diameter to deformed rocks.

The SEM analyses were performed to identify the mineralogy of the cataclastic matrix, allowing the identification of minerals such as K-feldspar, plagioclase, quartz, and iron oxides, apatite, and glass (Fig. 4.11E, F, G). The intense grain fracturing and comminution lead to the segregation of surviving grains and small fragments. The finest grains identified in the cataclastic matrix were the feldspar grains with a 1.92 μm diameter (Fig. 4.11H). The mean maximum diameters of quartz, K-feldspar, and plagioclase grain from protocataclastic bands are ~60, 46, and 50 μm (Fig. 4.11H), respectively. The mean diameters for deformation bands with more intense cataclasis are 17 μm (quartz-feldspar), 20 μm (plagioclase), and 21 μm (quartz); cataclastic bands present mean values of 14 μm (K-feldspar), 17 μm (plagioclase), and 20 μm (quartz). We also analyzed the composition of surviving grains in different types of cataclastic matrix. The protocataclastic bands yielded values of 27% (K-feldspar), 31% (plagioclase), and 42% (quartz). Cataclastic and ultracataclastic samples yielded values of 22% (K-Feldspar), 35% (plagioclase), and 43% (quartz), and 7% (K-Feldspar), 20% (plagioclase), and 73% (quartz), respectively. We also measured mean grain diameter to host rock of cataclastic and ultracataclastic deformation bands (Fig. 4.11H). The mean maximum diameters of quartz, K-feldspar, and plagioclase grain from host rock of cataclastic and ultracataclastic bands are ~82, 43, and 43 μm, and ~44, 36, and 28 μm (Fig. 4.11H), respectively. The composition of surviving grains in host rock of cataclastic and ultracataclastic bands are 17% (quartz), 47% (K-feldspar), and 36% (plagioclase), and 24% (quartz), 46% (K-feldspar), and 30% (plagioclase), respectively.

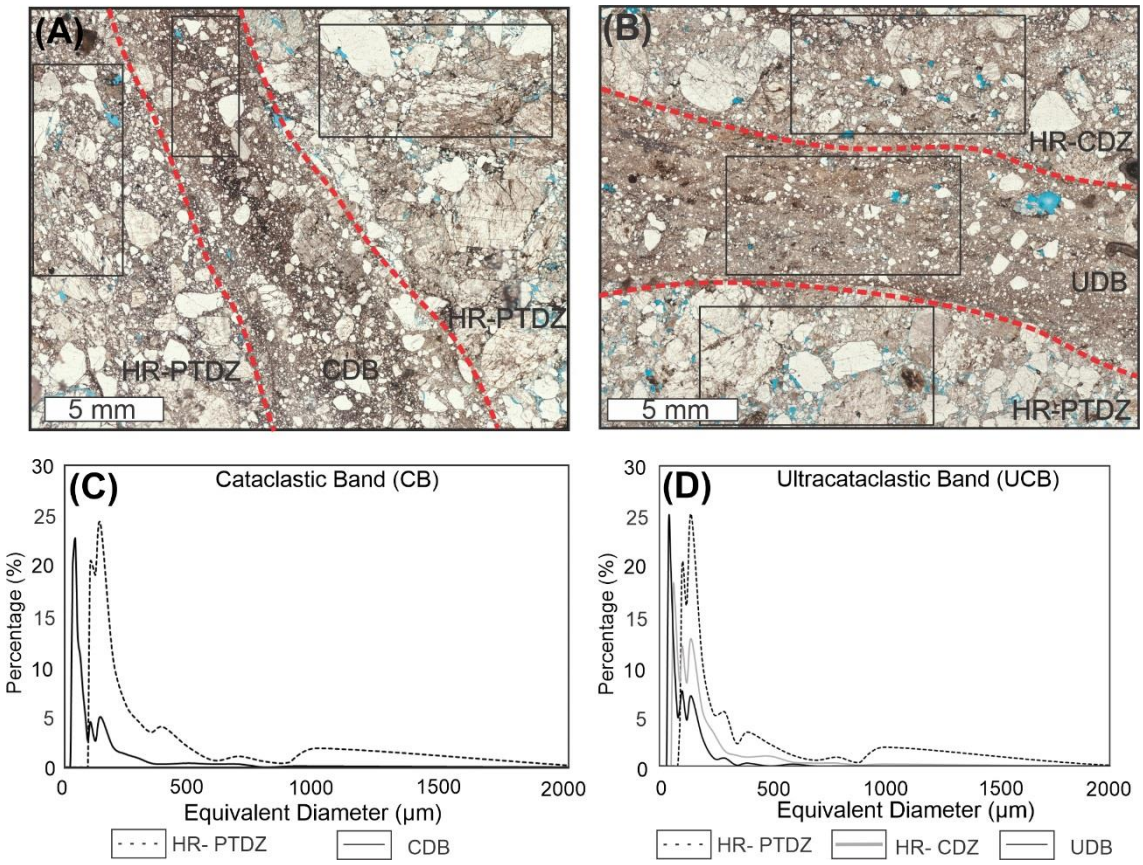

Figure 4.12. (A) Cataclastic deformation band showing moderate to intense cataclasis, with grain comminution and development of secondary porosity. Note the destruction of grains in the comminution zone. (B) Ultracataclastic deformation band showing very high deformation and generation of cataclastic matrix. Graphs indicating the grain size distribution in the host rock in both (C) cataclastic deformation band and (D) ultracataclastic deformation band. PTDZ – Protocataclastic Deformation Zone. CDB – Clastic Deformation Band. CDZ – Cataclastic Deformation Zone. UDB – Ultracataclastic Deformation Band. HR – Host Rock.

4.5 Discussion

4.5.1 Evolution of porosity in deformation bands

The porosity reduction in deformation bands has been studied in detail during recent years. Among the factors cited in the bibliography, the intensity of cataclasis involved is constantly considered the most relevant process in the reduction of porosity (Fossen et al., 2007, 2017; Ballas et al., 2012, 2015; Saillet and Wibberley, 2013; Shipton et al., 2019; Pizzati et al., 2020). The progressive decrease in porosity in cataclastic deformation bands has been constantly attributed to the intensity of cataclasis due to the strong grain size reduction and compression generated by shear (Fossen et al., 2007, 2017; Balsamo et al., 2014; Ballas et al., 2012, 2015; Saillet and Wibberley, 2013), which reduce the volume and pore diameter. This process can be progressively intensified by the evolution

of displacement in poorly lithified sandstone (e.g., Balsamo & Storti, 2010; Pizzati et al., 2020). The main deformation mechanisms associated with cataclasis are rotation/sliding of comminuted grains and pore collapse (Gambino et al., 2019), as well as post-deformational diagenetic cementation or alteration (Fisher and Knipe,1998; Fowles and Burley, 1994).

In this work, we performed petrophysical analyses of both undeformed rocks and deformation bands with different cataclastic intensities (protocataclastic, cataclastic and ultracataclastic) developed in the same basin-bounding fault zone. These results confirm that the porosity decrease is a function of cataclastic intensity within the bands, from small porosity reductions in protocataclastic bands to moderate porosity reductions in cataclastic bands. However, in these types of bands, the porosity reduction occurs in a non-linear manner, promoting a lower mechanical compaction of the rock along the zone affected by deformation bands, obliterating pores in some zones but at the same time generating new pores or even increasing the effective porosity by the connection of pre-existing pores. The data obtained in this work suggest, however, that the relationship between deformation and reduction in porosity represents different factors depending on the degree of deformation.

We also suggest that this porosity reduction is generated initially by pore collapse and fracturing, followed by grain crushing the grains by shearing that produces greater volume of a cataclastic matrix (Fig. 4.13B-E). The volume of the cataclastic matrix is a function of grain size reduction in the undeformed rock (Fig. 4.13B-E). Thus, the higher the cataclastic matrix volume, the higher the strain intensity within the band. In less intense strain stages, where the amount of cataclasis is small, the protocataclastic deformation bands show reduction in porosity dispersion because the grains are partially preserved, and the grain size reduction is small (Fig. 4.13B). In this stage, the grain border comminution is predominantly due to pervasive but heterogeneous grain flow, promoting grain rotation, and the formation of cataclastic matrix that fills primary pores (Nicchio et. al., 2018). Additionally, the shear tends to consolidate the sediments by compaction, resulting in porosity reduction (Rawling and Goodwin, 2006). Such processes would result in a porosity reduction proportional to strain (Fig. 4.13C, D). However, as our data indicate that on small strain stages, secondary porosity is also formed (Figure 4.5D), we suggest that the secondary porosity formation might be responsible for the non-linear relation between strain increase and porosity reduction. This dispersion behaviour is due

assumed to lower mechanical compaction of the rock along the zone affected by deformation bands, obliterating pores in some areas and in other areas generating new pores or even increasing effective porosity by the connection of pre-existing pores (see primary and secondary porosity in Figs. 4.5A, C, D).

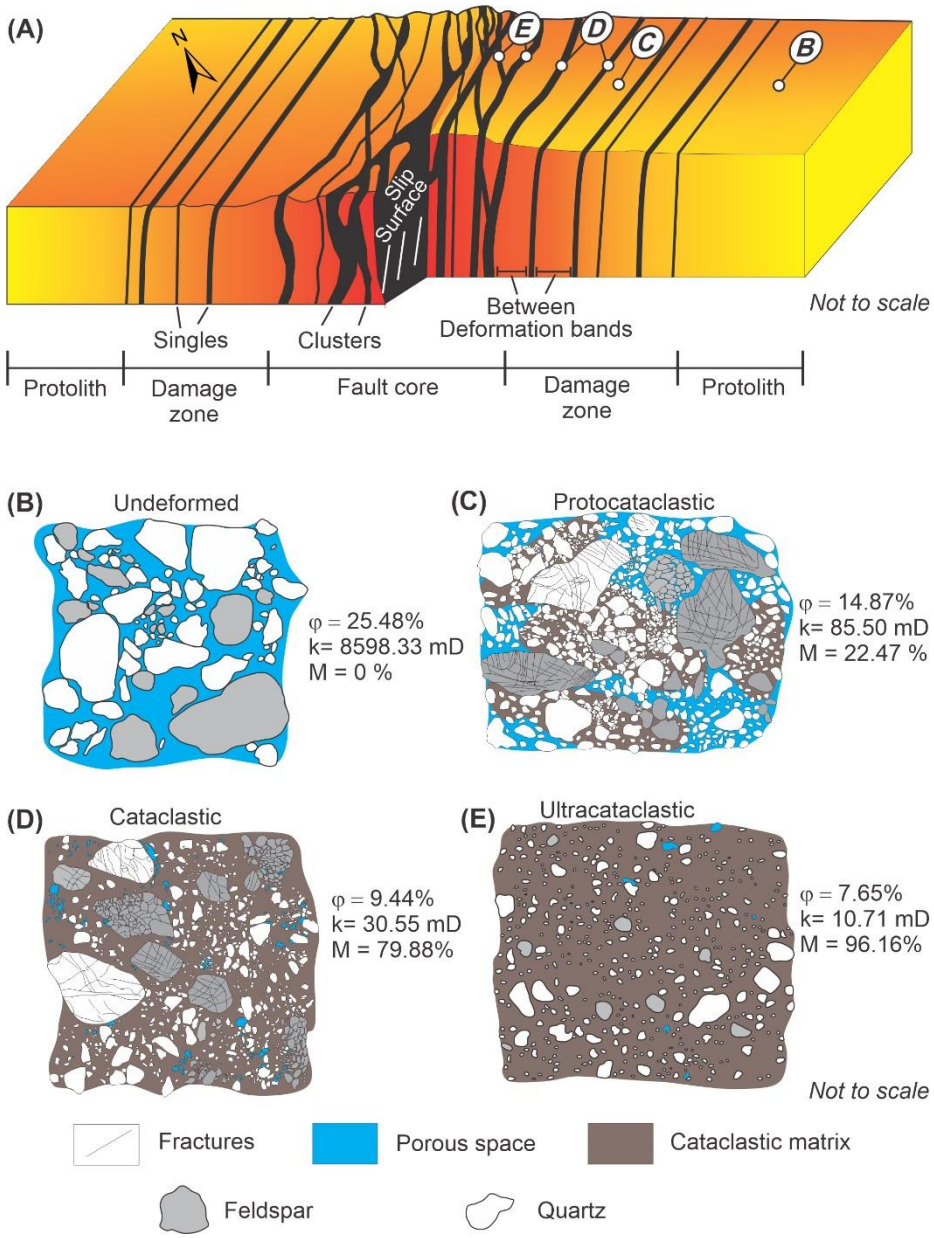

Figure 4.13. Schematic model showing (A) location of the collected samples across a fault zone representing the protolith, area between deformation bands, single bands, clusters, and slip surfaces. The different deformation stages of the cataclastic deformation band: (B) undeformed rocks, (C) protocataclastic, (D) cataclastic, and (E) ultracataclastic deformation bands, with the correlation between porosity (φ), permeability (k), and cataclastic matrix (M).

Porosity values can display a negative correlation with the amount of cataclasis, mainly related to the increase in the degree of cataclastic intensity (e.g., Philit et al., 2018) or in case for disaggregation bands (Fossen, 2010). The porosity of deformation bands can be lower than that of the host rocks, with the deformed rocks displaying an average porosity reduction of approximately 15% (Torabi, 2014). Porosity can be further reduced in slip surfaces, reaching two orders of magnitude of porosity reduction in comparison to the host rocks (Peralta Gomes et al., 2018; Gambino et al., 2019).

On the other hand, when analysing ultracataclastic deformation bands, a strong linear relationship is observed (Fig. 4.10B), controlled by the increase in the amount of cataclastic matrix (deformation intensity) and porosity reduction (Fig. 4.13D). We suggest that after reaching the ultracataclastic deformational stage (> 90% matrix), the pore size may no longer be large enough to allow the rearrangement of the grains, thus cancelling the compaction factor and making secondary porosity unfeasible. Therefore, the porosity reduction in ultracataclastic deformation bands is dependent only on the breakdown of the residual grains by the addition of strain, generating more matrix and progressively filling the remaining pores around surviving grains (Fig. 4.13D). The data reveal that the porosity reduction ranges one order of magnitude in ultracataclastic deformation bands.

The cataclastic process is the main responsible for porosity reduction, particularly where grain crushing is more effective (Fossen et al., 2007). The grain fracturing promotes drastic grain diameter reduction and changes on pore volume, which can either increase or reduce. The grain crushing is controlled by including mineralogy, grain composition and strength, grain size, shape and packing geometry (Wong and Baud, 1999; Rawling and Goodwin, 2003), as well as by consolidation state and cementation (e.g., Rawling and Goodwin, 2006). The analysis of pore access shows intense peaks with a diameter of ~50 μm on undeformed samples. The deformed samples present the extinction of large pores (close to 10-100 μm), concentrating the pore diameters between 0.1 and 10 μm. In deformation bands, heterogeneity in the pore access occurs with diameters >20 μm. This result indicates that the pores with larger diameters have been obliterated in varied ways, leading to a non-direct and non-linear relationship between the development of the pore diameter and porosity (Fig. 4.9). Particles size concentrates in the sand and gravel intervals in the protolith, with minor concentrations of silt and clay. We observed that the matrix minerals are the same of the larger sized clasts,

predominantly K-feldspar, plagioclase, and quartz. In the undeformed rocks, the grain size ranges from 240 to 5000 μm. Our data indicate that the cataclastic processes result in a progressive reduction in the maximum grain size, producing grains with minimum diameter of 1.92 μm. This reduction is controlled by a few factors such as the amount of shearing during the extensional tectonic regime, mineralogy, absence of cementation, and grain size.

4.5.2 Role of mineralogy

The mineral composition is a relevant parameter for the formation and development of rock deformation due to variations in shape, chemical stability, strength, and susceptibility to cleavage fracture (Aydin et al., 2006). In particulate flow, grain breakage can be selective. The selective grain breakage controls the sealing potential of fault rocks, thus lithological variations in the host rock should not be neglected in fault seal analysis (Schröckenfuchs et al., 2019). Feldspar grains show preferential fractures oriented along cleavage planes and intragranular fracturing. On the other hand, quartz grains show fractures with dispersed orientations and tend to break by transgranular and spalling fractures (Rawling and Goodwin, 2003; Del Sole and Antonellini, 2019; Shipton et al., 2019). Therefore, we suggest that the presence of feldspar grains exerts a great influence on the development of the cataclasis process within the undeformed rock. This influence is evident in both altered (Exner and Tschegg, 2012) and non- altered feldspar (Nicchio et al., 2018; Del Sole and Antonellini, 2019), with feldspar grains showing lower differential stress than quartz grains (Rawling and Goodwin, 2003). Our results are consistent with those presented in the bibliography. The arkosic and arkosic-lithic sandstone samples in this study clearly show preferential intragranular fracturing of feldspar grains with respect to quartz grains, which might be due to differences in susceptibility to cleavage fracture (Fig 4.11E, F, G). This behaviour makes feldspar weaker and more prone to breakage than quartz (Fig. 4.11E - H). This fact shows the mineralogical control on the grain size distribution in the studied sandstones (Fig. 4.13). In the ultracataclastic deformation bands, we observe the relative preservation of quartz clasts and almost intense destruction of feldspar grains (Fig. 4.13C, D).

4.5.3 Implications for reservoir quality

Regarding permeability, all studied deformation bands have negative impacts on permeability, with reductions from 1 to 6 orders of magnitude relative to that of the host rocks, as already observed elsewhere (Fossen and Bale, 2007; Ballas et al., 2015). The variation in the permeability reduction can be attributed to the degree of cataclasis within these deformation bands (Torabi, 2014). Most studies indicate that the average permeability reduction is about two to three orders of magnitude (e.g. Crawford, 1998). In cataclastic bands, the crush microbreccia and protocataclastic types show very low degrees of cataclasis and have induced permeability reductions less than two orders of magnitude (Lubiniecki et al., 2019). The permeability reduction range can be up to two orders of magnitude relative to the host rocks, which is comparable to the permeability reduction in cataclastic and ultracataclastic deformation bands in clustering zones, slipped deformation bands, and fault cores (Rotevatn et al., 2013; Torabi, 2014; Ballas et al., 2015). The Jurassic sandstones of the Colorado Plateau show permeability values greater than 1 Darcy (Fossen and Sole, 2007). The single cataclastic deformation bands from these deformed sandstones exhibit one to two orders of magnitude of permeability reduction, and cluster zones with densely packed deformation bands from the same layer show reduction of about five orders of magnitude (Fossen and Sole, 2007).

The permeability analysis from different band structures in porous sandstones indicates that the difference in permeability is significant. This analysis confirms that permeability decrease is as a function of cataclasis intensity in bands, from 1 to 3 orders of magnitude of permeability reduction in crush microbreccia of Pure Compaction Bands (PCBs) and Shear-Enhanced Compaction Bands (SECBs) to greater than three orders of magnitude permeability reduction in cataclasites/ultracataclasites of shear bands from band clusters, slipped bands, and fault cores (Ballas et al., 2015). Our results show that in undeformed rocks, the mean permeability values are greater than 8 Darcy. In cataclastic bands, the protocataclastic type shows mean permeability values equal to 88.50 μm in between deformation bands. The cataclastic bands with high degrees of cataclasis, such as cataclastic and ultracataclastic bands, show 1 to 5 orders of magnitude of permeability reduction, respectively (Fig. 4.7B), in zones of singles and clustering deformation bands, and slip surface.

4.6 Conclusions

The structural and microtextural analyses performed in the present study reveal a fault zone composed of different types of deformation bands, which evolved progressively within the same tectonic regime but with different deformation intensities. The results of this study suggest the following conclusions: The microstructural evolution of deformation band chosen for study in this work occurs in extensional tectonic regime and is identified in the same fault zone that presents the following elements: between deformation bands, single bands, clusters, and slip surfaces. The protocataclastic deformation bands occur between deformation bands, whereas the cataclastic and ultracataclastic deformation bands occur as single bands and clusters, and sometimes the cataclastic and ultracataclastic texture can be associated with the slip-surfaces. The architectural elements identified in the fault zone exert strong control on the petrophysical properties of rocks in the study area. The deformation mechanisms consequently modify the tight cataclastic fabric inside the deformation bands.

The compaction of the cataclastic fabric is influenced by the intensity of deformation within cataclastic deformation bands. The increase in grain comminution by intense cataclasis promotes the gradual generation of the cataclastic matrix, allowing the formation of ultracataclastic bands. At this level of deformation, properties such as porosity are fully controlled by the development of the comminuted matrix. In the ultracataclastic deformation bands, the only factor that influences the porosity is the amount of cataclastic matrix generated during deformation.

It is possible to estimate the porosity relative reduction and permeability of cataclastic deformation bands by analysing the amount of cataclastic matrix. The increase in deformation intensity produces a reduction in the number of macropores identified in the undeformed rock because of the comminution of the grains, affecting the pore access. In general terms, the process of grain comminution commonly leads to the reduction in pore size, consequently decreasing the amount of isolated pore space within the deformation bands.

Acknowledgements

We thank Gregory Ballas, Haakon Fossen, an anonymous reviewer, and Marine and Petroleum Geology editor Kei Ogata for their comments and corrections, which greatly

improved the manuscript. We also thank the Brazilian Agency of Oil, Gas, and Biofuels (*Agência Nacional do Petróleo*, ANP). This study was sponsored by Petrobras/Federal University of Campina Grande project (TC 5850.0109438.18.9) grant to Francisco C. C. Nogueira.

References

Antonellini, M.A., Aydin, A., Pollard, D.D., 1994. Microstructure of deformation bands in porous sandstones at Arches National Park, Utah. Journal of Structural Geology 16, 941–959. http://dx.doi.org/10.1016/0191-8141(94)90077-9.

Araujo, R. E.B., Bezerra, F. H. R., Nogueira, F. C.C., Balsamo, F., Carvalho, B. R.B.M., Souza, J. A.B., Sanglard, J. C.D., De Castro, D. L., Melo, A.C.C., 2018. Basement control on fault formation and deformation band damage zone evolution in the Rio do Peixe Basin, Brazil. Tectonophysics 745, 117–131. https://doi.org/10.1016/j.tecto.2018.08.011.

Aydin A., 1978. Small faults formed as deformation bands in sandstone. Pure and Applied Geophysics 116 (4‑5), 913‑930. https://doi.org/10.1007/BF00876546.

Aydin, A., Johnson, A.M., 1978. c. Pure and Applied Geophysics, 116, 931–942. https://doi.org/10.1007/BF00876547.

Aydin, A., Borja, R.I., Eichhubl, P., 2006. Geological and mathematical framework for failure modes in granular rock. Journal of Structural Geology 28, 83–98. https://doi.org/10.1016/j.jsg.2005.07.008.

Ballas, G., Soliva, R., Sizun, J.P., Benedicto, A., Cavailhes, T., Raynaud, S., 2012. The importance of the degree of cataclasis in shear bands for fluid flow in porous sandstone Provence, France. The American Association of Petroleum Geologists Bulletin 96, 2167–2186. http://dx.doi.org/10.1306/04051211097.

Ballas, G., Soliva, R., Sizun, J.P., Fossen, H., Benedicto, A., Skurtveit, E., 2013. Shear-enhanced compaction bands formed at shallow burial conditions; implications for fluid flow (Provence, France). Journal of Structural Geology 47, 3–15. https://doi.org/10.1016/j.jsg.2012.11.008.

Ballas, G., Fossen, H., Soliva, R., 2015. Factors controlling permeability of cataclastic deformation bands and faults in porous sandstone reservoirs. Journal of Structural Geology 76, 1–21. http://dx.doi.org/10.1016/j.jsg.2015.03.013.

Balsamo F & Storti F, 2010. Grain size and permeability evolution of soft-sediment

extensional sub-seismic and seismic fault zones in high-porosity sediments from the Crotone basin, southern Apennines, Italy. Marine and Petroleum Geology 27, 822-837.

Balsamo, F., Storti, F., Grocke, D., 2012. Fault-related fluid flow history in shallow marine sediments from carbonate concretions, Crotone Basin, south Italy. Journal of the Geological Society, London 169, 613-626. doi: 10.1144/0016-76492011-109

Balsamo, F., Aldega, L., De Paola, N., Faoro, I., Storti, F., 2014. The signature and mechanics of earthquake ruptures along shallow creeping faults in sediments. Geology 42, 435–438. http://dx.doi.org/10.1130/G35272.1.

Brito Neves, B.B., Santos, E.J., Van Schmus, W.R., 2000. Tectonic History of the Borborema Province, Northeast Brazil. In: Cordani, U.G., Thomaz Filho, A., Campos, D.A. (eds) Tectonic Evolution of South America. Rio de Janeiro, 31STIGC, 151–182.

Cladouhos, T.T., 1999. Shape preferred orientations of survivor grains in fault gouge. Journal of Structural Geology 21, 419 - 436. https://doi.org/10.1016/S0191-8141(98)00123-0.

Crawford, B.R. 1998. Experimental fault sealing: shear band permeability dependency on cataclastic fault gouge characteristics. In: Coward, M.P., Johnson, H. & Daltaban, T.S. (eds) Structural Geology in Reservoir Characterization. Geological Society, London, Special Publications, 127, 83–97.

Davis, G.H., 1999. Structural geology of the Colorado Plateau Region of southern Utah. In: Editor, A. (ed.) Book Title. Geological Society of America, Special 45 Papers 342, 1–157. https://doi.org/10.1130/0-8137-2342-6.1

de Castro, D.L., de Oliveira, D.C., Gomes Castelo Branco, R.M., 2007. On the tectonics of the Neocomian Rio do Peixe Rift Basin, NE Brazil: lessons from gravity, magnetics, and radiometric data. Journal of South American Earth Sciences 24, 184–202. http://dx.doi.org/10.1016/j.jsames.2007.04.001.

Del Sole, L., Antonellini, M., 2019. Microstructural, petrophysical, and mechanical properties of compactive shear bands associated to calcite cement concretions in arkose sandstone. Journal of Structural Geology 126, 51–68. https://doi.org/10.1016/j.jsg.2019.05.007.

Exner, U., Tschegg, C., 2012. Preferential cataclastic grain size reduction of feldspar in deformation bands in poorly consolidated arkosic sands. Journal of Structural Geology 43, 63-72. https://doi.org/10.1016/j.jsg.2012.08.005.

Faulkner, D.R., Jackson, C.A.L., Lunn, R.J., Schlische, R.W., Shipton, Z.K., Wibberley, C.A.J., Withjack, M.O., 2010. A review of recent developments concerning the structure, mechanics and fluid flow properties of fault zones. Journal of Structural Geology 32, 1557–1575. https://doi.org/10.1016/j.jsg.2010.06.009.

Fisher, Q.J., Knipe, R.J., 1998. Fault sealing processes in siliciclastic sediments. Geological Society, London 147, 117-134. https://doi.org/10.1144/GSL.SP.1998.147.01.08.

Fisher, Q.J., Knipe, R.J., 2001. The permeability of faults within siliciclastic petroleum reservoirs of the North Sea and Norwegian Continental Shelf. Marine and Petroleum Geology 18, 1063–1081. http://dx.doi.org/10.1016/S0264-8172(01)00042-3.

Folk, R.L., 1968. Hemphill, Austin, Texas. Petrology of the Sedimentary Rocks 190. http://dx.doi.org/10.1016/0169-555X(91)90027-8.

Fossen, H. 2010. Deformation bands formed during soft-sediment deformation: Observations from SE Utah. Marine and Petroleum Geology 27, 215–222. doi:10.1016/j.marpetgeo.2009.06.005

Fossen, H., Bale, A., 2007. Deformation bands and their influence on fluid flow. The American association of Petroleum Geologists Bulletin 91, 1685–1700. https://doi.org/10.1306/07300706146.

Fossen, H., Schultz, R.A., Shipton, Z.K., Mair, K., 2007. Deformation bands in sandstone: a review. Journal of the Geological Society London 164, 1–15. http://dx.doi.org/10.1144/0016-76492006- 036.

Fossen, H., Soliva, R., Ballas, G., Trzaskos, B., Cavalcante, C., Schultz, R.A., 2017. A review of deformation bands in reservoir sandstones: geometries, mechanisms and distribution. In: Ashton, M., Dee, S.J., Wennberg, O.P., (eds) Subseismic-Scale Reservoir Deformation. Geological Society London, Special Publications 459, 9–33. http://dx.doi.org/10.1144/SP459.4.

Fowles, J. and Burley, S., 1994. Textural and permeability characteristics of faulted, high porosity sandstones. Marine Petroleum Geology 11, 608 – 623. https://doi.org/10.1016/0264-8172(94)90071-X.

Françolin, J.B.L., Cobbold, P.R., Szatmari, P., 1994. Faulting in the early cretaceous Rio do Peixe basin (NE Brazil) and its significance for the opening of the Atlantic. Journal of Structural Geology 16, 647–661. https://doi.org/10.1016/0191-8141(94)90116-3.

Gambino, S., Fazio, E., Maniscalco, R., Punturo, R., Lanzafame, G., Barreca, G., Butler,

R.W.H., 2019. Fold-related deformation bands in a weakly buried sandstone reservoir analogue: A multi-disciplinary case study from the Numidian (Miocene) of Sicily (Italy). Journal of Structural Geology 118, 150–164. S. https://doi.org/10.1016/j.jsg.2018.10.005.

Gibson, R.G., 1998. Physical character and fluid-flow properties of sandstone derived fault zones. In: Coward, M.P., Johnson, H., Daltaban, T.S., (eds) Structural Geology in Reservoir Characterization. Geological Society London, Special Publications 127, 83–97. https://doi.org/10.1144/GSL.SP.1998.127.01.07.

Griffiths, J., Faulkner, D.R., Edwards, A.P., Worden, R.H., 2016. Deformation band development as a function of intrinsic host-rock properties in Triassic Sherwood Sandstone. Geological Society London, Special Publications 435, 161–176. https://doi.org/10.1144/SP435.11.

Holcomb, D., Rudnicki, J.W., Issen, K.A., Sternlof, K., 2007. Compaction localization in the Earth and the laboratory: state of the research and research directions. Acta Geotechnica 2, 1–15. https://doi.org/10.1007/s11440-007-0027-y.

Johnson, A.M., 1995. Orientations of faults determined by premonitory shear zones. Tectonophysics 247, 161–238. https://doi.org/10.1016/0040-1951(95)00002-5.

Killick, A.M., 2003. Fault Rock Classification: An aid to structural interpretation in mine and exploration geology. South African Journal of Geology 106 (4), 395–402. https://doi.org/10.2113/106.4.395.

Knipe, R.J., Jones, G., Fisher, Q.J., 1998. Faulting, fault sealing and fluid flow in hydrocarbon reservoirs: an introduction. In: Jones, G., Fisher, Q.J., Knipe, R.J., (eds) Faulting, Fault Sealing and Fluid Flow in Hydrocarbon Reservoirs. Geological Society London, Special Publications 147, vii-xxi. https://doi.org/10.1144/GSL.SP.1998.147.01.01.

Lubiniecki, D. C., White, S. R.S., King, R. C., Holford, S. P., Bunch, M. A., Hill, S. M., 2019. Structural evolution of carbonate-hosted cataclastic bands adjacent to a major neotectonic fault, Sellicks Beach, South Australia. Journal of Structural Geology 129, 11–24. https://doi.org/10.1016/j.jsg.2019.05.004.

Maciel, I.B., Dettori, A., Balsamo, F., Bezerra, F.H.R., Vieira, M.M., Nogueira, F.C.C., Salvioli-Mariani, E., Sousa, J.A.B., 2018. Structural Control on Clay Mineral Authigenesis in Faulted Arkosic Sandstone of the Rio do Peixe Basin, Brazil. Minerals 8, 1–17. https://doi.org/10.3390/min8090408.

Matos, R.M.D., 1992. The northeastern Brazilian Rift System. Tectonics 11 (4), 766–791.

https://doi.org/10.1029/91TC03092

Nicchio, M.A., Nogueira, F.C.C., Balsamo, F., Souza, J.A.B., Carvalho, B.R.B.M., Bezerra, F.H.R., 2018. Development of cataclastic foliation in deformation bands in feldspar-rich conglomerates of the Rio do Peixe Basin, NE Brazil. Journal of Structural Geology 107, 132-141. https://doi.org/10.1016/j.jsg.2017.12.013.

Nogueira, F.C.C., Marques, F.O., Bezerra, F.H.R., de Castro, D.L., Fuck, R.A., 2015. Cretaceous intracontinental rifting and post-rift inversion in NE Brazil: insights from the Rio do Peixe Basin. Tectonophysics 644, 92–107. http://dx.doi.org/10.1016/j.tecto.2014.12.016.

Parry, W.T., Chan, M.A., Beitler, B., 2004. Chemical bleaching indicates episodes of fluid flow in deformation bands in sandstone. The American Association of Petroleum Geologists Bulletin 88, 175–191. https://doi.org/10.1306/09090303034.

Peralta Gomes, C., Fossen, H., Almeida. R. P., Salmoni, B., 2018. Subseismic deformation in the Vaza-Barris Transfer Zone in the Cretaceous Recôncavo-Tucano-Jatobá rift system, NE Brazil. Journal of Structural Geology 117, 81–95.

Philit, S., Soliva, R., Castilla, R., Ballas, G., Taillefer, A., 2018. Clusters of cataclastic deformation bands in porous sandstones. Journal of Structural Geology 114, 235–250. https://doi.org/10.1016/j.jsg.2018.04.013.

Pittman, E.D., 1981. Effect of fault-related granulation on porosity and permeability of quartz sandstones, Simpson Group (Ordovician) Oklahoma. The American Association of Petroleum Geologists Bulletin 65, 2381–2387. https://doi.org/10.1306/03B5999F-16D1-11D7-8645000102C1865D.

Pizzati, M., Balsamo, F., Storti, F., 2020. Displacement-dependent microstructural and petrophysical properties of deformation bands and gouges in poorly lithified sandstone deformed at shallow burial depth (Crotone Basin, Italy). Journal of Strutural Geology 137. https://doi.org/10.1016/j.jsg.2020.104069.

Pontes, C. C.C., Nogueira, F. C.C., Bezerra, F. H.R., Balsamo, F., Miranda, T. S., Nicchio, M. A, Souza, J. A.B., Carvalho, B. R.B.M., 2019. Petrophysical properties of deformation bands in high porous sandstones across fault zones in the Rio do Peixe Basin, Brazil. International Journal of Rock Mechanics and Mining Sciences 114, 153–163.

Rawling, G. C., Goodwin, L. B., 2003. Cataclasis and particulate fow in faulted, poorly lithified sediments. Journal of Structural Geology 25, 313–331. https://doi.org/10.1016/S0191-8141(02)00041-X.

Rawling, G.C., Goodwin, L.B., 2006, Structural record of the mechanical evolution of mixed zones in faulted poorly lithified sediments, Rio Grande rift, New Mexico, USA. Journal of Structural Geology 28, 1623–1639. doi: 10.1016/j.jsg.2006.06.008.

Rotevatn, A., Sandve, T.H., Keilegavlen, E., Kolyukhin, D., Fossen, H., 2013. Deformation bands and their impact on fluid flow in sandstone reservoirs: the role of natural thickness variations. Geofluids 13, 359–371. https://doi.org/10.1111/gfl.12030

Rotevatn, A., Fossmark, H.S., Bastesen, E., Thorsheim, E., Torabi, A., 2017. Do deformation bands matter for flow? Insights from permeability measurements and flow simulations in porous carbonate rocks. Petroleum Geoscience 23, 104–119. https://doi.org/10.1144/petgeo2016-038.

Saillet, E., Wibberley, C.A.J., 2013. Permeability and flow impact of faults and deformation bands in high-porosity sand reservoirs: southeast Basin, France, analog. Am. Assoc. Pet. Geol. Bull. 97, 437–464. http://dx.doi.org/10.1306/09071211191.

Sample, J.C., Woods, S., Bender, E., Loveall, M., 2006. Relationship between deformation bands and petroleum migration in an exhumed reservoir rock, Los Angeles Basin, California, USA. Geofluids 6, 105–112. ttps://doi.org/10.1111/j.1468-8123.2005.00131.x.

Schröckenfuchs, T., Schuller, V., Zamolyi, A., 2019. Influence of Host Rock Lithology Contrast on Permeability Reduction in Fault Zones (Vienna Basin, Austria). Publisher: European Association of Geoscientists & Engineers; Source: Conference Proceedings, Fifth International Conference on Fault and Top Seals 2019, 1 – 5. https://doi.org/10.3997/2214-4609.201902309

Seeburger, D. A., A. Aydin, and J. L. Warner, 1991, Structure of fault zones in sandstone and its effect on permeability (abs): American Association of Petroleum Geology Bulletin 75, 669.

Sénant, J., Popoff, M., 1991. Early Cretaceous extension in northeast Brazil related to the South Atlantic opening. Tectonophysics 198, 35–46. http://dx.doi.org/10.1016/0040-1951(91)90129-G.

Shipton, Z. K., Roberts, J. J., Comrie, E. L., Kremer, Y., Lunn, R. J., Caine, J. S., 2019. Fault fictions: systematic biases in the conceptualization of fault-zone architecture. Journal Geological Society London, Special Publications, 496. https://doi.org/10.1144/SP496-2018-161.

Sibson, R.H., 1977. Fault rocks and fault mechanisms. Journal of the Geological Society

London 133, 191–213. http://dx.doi.org/10.1144/gsjgs.133.3.0191.

Soliva, R., Ballas, G., Fossen, H., Philit, S., 2016. Tectonic regime controls clustering of deformation bands in porous sandstone. Geology 44(6), 423–426. https://doi.org/10.1130/G37585.1.

Sternlof, K.R., Karimi-Fard, M., Pollard, D.D., Durlofsky, L.J., 2006. Flow and transport effects of compaction bands in sandstone at scales relevant to aquifer and reservoir management. Water Resources Research 42(7), W07425. doi:10.1029/2005WR004664.

Torabi, A., Braathen, A., Cuisiat, F., Fossen, H., 2007. Shear zones in porous sand: Insights from ring-shear experiments and naturally deformed sandstones. Tectonophysics 437 (1–4), 37–50. https://doi.org/10.1016/j.tecto.2007.02.018.

Torabi, A., and Fossen, H., 2009. Spatial variation of microstructure and petrophysical properties along deformation bands in reservoir sandstones. The American Association of Petroleum Geologists Bulletin 93 (7), 919–938. https://doi.org/10.1306/03270908161.

Torabi, A., Fossen, H., Braathen, A., 2013. Insight into petrophysical properties of deformed sandstone reservoirs. The American Association of Petroleum Geologists Bulletin 97(4), 619–637. https://doi.org/10.1306/10031212040.

Torabi, A., 2014. Cataclastic bands in immature and poorly lithified sandstone, examples from Corsica, France. Tectonophysics 630, 91–102. http://dx.doi.org/10.1016/j.tecto.2014.05.014.

Valeriano, M. M., Albuquerque, P. C. G., 2010. Topodata: Processamento dos dados SRTM. Instituto Nacional de Pesquisas Espaciais – INPE, São José dos Campos 79pp. (INPE–16702–RPQ/854).

Wong, T-f., Baud, P., 1999. Mechanical Compaction of Porous Sandstone. Oil & Gas Science and Technology 54, 715-727. doi: 10.2516/ogst:1999061.

Chapter 5 - General Conclusions

In this PhD thesis we performed a multiscale and multidisciplinary approach to constrain the strain trajectories responsible for the opening and tectonic evolution of the Rio do Peixe Basin (Brazil) and their effects on siliciclastic reservoirs. The work includes field and laboratorial analyses such as structural/microstructural, magnetic, clay mineral analysis and petrophysical surveys. From the combination of these data, the following conclusions can be considered.

From AMS and structural data, we found two distinct and orthogonal stretching directions diverging about 79º that were present during the syn-rift phase of the Rio do Peixe Basin, namely syn-rift phase I and syn-rift phase II. The syn-rift phase I represents the initial opening stage of the basin. During this stage, a NNE-SSW main strain trajectories resulted in initial brittle reactivation of the branches of the Proterozoic Tranzbrasilian shear zone, the E-W striking Patos and the NE-SW striking Portalegre shear zones. During this phase, the NNE-SSW stretching caused the brittle reactivation of the E-W striking shear zones in normal shear sense dipping north, in Malta Fault. At the same time, NE-SW shear zones were reactivated in right-lateral transtensive sense, reflecting the block movement towards north, forming from W to E, the NE-striking Portalegre, Sítio Saguí and Lagoa do Forno faults.

In the syn-rift phase II, the strain trajectory direction gradually shifted from NNE-SSW to NW-SE, changing the major faults kinematics. In syn-rift phase II, the E-W striking Malta fault shifted from normal to left-lateral transtensive shear sense. At the same time, NE-SW striking faults, turned from right-lateral transtensive to normal shear sense with faults dipping NW. In this stage, the deformation in sedimentary units started to form, identified mostly due NE-SW striking extensional faults within sediments with damage zone dominated by deformation bands and deformation band clusters sub-parallel to main border faults. The Rio do Peixe basin is product of the gradual counterclockwise intraplate stress rotation in the Borborema Province during the pre-Pangea breakup in the Cretaceous period.

Within the basin, faults and deformation bands, product of syn-rift phase II deformation, constantly affect the porous sandstones. Through structural, microstructural, clay mineralogy analysis and petrophysical analysis, we characterized the main structures

correlating with the tectonic evolutionary stage of the basin and their effects on fluid flow properties. Two main fault-related deformation band sets occur in the basin boundary Portalegre fault zone. The extensional NE-SW trending faults were the first to form in soft sediments conditions during the syn-rift phase. The post-rift structures are NW-SE and NNW-SSE trending transtensive faults and crosscut the syn-rift phase II faults. In respect to the syn-rift phase II faults, the post-rift faults present a more destructive behavior evidenced by the relative greater grain size reduction. Additionally, greater permeability reduction and higher capillary pressure observed in post-rift faults evidences that they form more effective sealing structures in respect to the syn-rift structures. Microscopic characteristics of non-deformed host rock, together with clay mineralogy data indicated that the basin did not experienced deep burial depths, remaining shallow (<1-2 km). Consequently, the two fault systems documented in this study were both formed in shallow burial depth. The different microstructural and petrophysical properties of deformation bands formed during distinct tectonic stages is likely due to the progressive fault-induced tectonic compaction (strain hardening) acquired during the syn-rift stage. The host rock compaction and consequently the cataclasis intensity and sealing behavior progressively increases as new bands form after tectonic compaction. This shows that the development of faults and deformation bands present a strong relation with the tectonic phase of the basin. Thus, the tectonic interpretation of the RPB can support to prediction of the effects of deformation in siliciclastic reservoir properties.

The microstructural properties of deformation bands must also be considered, as the cataclasis intensity, measured by the amount of generated cataclastic matrix within the band is closely related to the porosity and permeability loss. In protocataclastic DB's (i.e., cataclastic bands with less than 50% of cataclastic matrix), the relation between porosity loss *versus* cataclastic matrix amount is quite random, as secondary porosity due grain fracturing is formed at the same time the primary porosity is destroyed. In cataclastic DB's (i.e., cataclastic bands with more than 50% and less than 90% of cataclasic matrix), a non-linear relation between porosity loss *versus* cataclastic matrix amount is observed, but in general view, the higher is the cataclastic matrix amount, the lower is the porosity. In this case, the formation of secondary porosity, although still being formed, becomes less important to the as the space for grain accommodation reduces. In ultracataclastic DB's (i.e., cataclastic bands with more than 90% of cataclastic matrix), the porosity reduction occurs exclusively as function of the increasing of the cataclastic matrix amount

in a linear relation. In this stage, the grains are reduced to very fine sizes in a very compacted fabric, making unfeasible the formation of secondary porosity that barely exists in this stage. The mineralogy is also an aspect to be analyzed, as feldspar grains produce higher amount of cataclastic matrix, deformation bands formed in arkosic sandtones tend to form more effective fluid flow barriers.

Acknowledgment

This PhD. thesis was supported by Petrobras, DEBRIP research project TC 5850.0109438.18.9 coordinated by Francisco Cezar Costa Nogueira, Universidade Federal de Campina Grande, Brazil. The AMS analysis was performed at the University of RomaTre in laboratory of paleomagnetism under supervision of the professor Dr. Francesca Cifelli. The RXD analysis was performed at the Sapienza University of Rome by the professor Dr. Luca Aldega.